Preparation of nitrogen-doped multiwalled carbon nanotubes anchored 2D platinum dichalcogenides for application as hydrogen evolution reaction catalysts

Lineo Florence Mxakaza (1465370)

A thesis submitted to the Faculty of Science, School of Chemistry at the University of the Witwatersrand, in partial fulfilment of the requirements for the degree of

Doctor of Philosophy

Supervisors: Dr. Zikhona Tetana & Prof. Nosipho Moloto

Johannesburg, 2024

Declaration

I proclaim that the work reported in this thesis is my own and was independently studied. It is being submitted for the degree of Doctor of Philosophy to the School of Chemistry, Faculty of Science at Wits University, Johannesburg. It has not been submitted to any institution previously for examination.

Candidate name: Lineo Florence Mxakaza

Signature: …….  **…….**

Date: …25/09/2024……

Supervisor name: Dr. Zikhona Tetana

Signature: ……  **…….**

Date: …25/09/2024……...…….

Co-supervisor name: Prof. Nosipho Moloto

Signature: …… 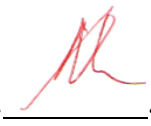 **…….**

Date: …25/09/2024……..

Abstract

The alkaline hydrogen evolution reaction (HER) ($H_2O + 2e^- \rightarrow H_2 + 2OH^-$) is fast gaining traction as a sustainable hydrogen gas generation route but suffers from slow reaction kinetics because of the additional water dissociation step and large reaction overpotential. As such, the current state-of-the-art acidic medium Pt and Ru catalysts suffer from considerable loss of catalytic activity in an alkaline medium. We propose the development and use of platinum metal dichalcogenides for alkaline HER. Platinum dichalcogenides are 2D materials that offer the advantage of more exposed catalytic sites, show dramatic chalcogen-dependent electronic properties, and have a band gap (0.24 eV - 1.8 eV for PtS_2 and $PtSe_2$) thus extending the use of these materials to light-stimulated photo-electrochemical (PEC) HER. As such, PtS_2 is reported to be a semiconductor, $PtSe_2$ is semi-conductive/semi-metallic depending on the number of layers, and $PtTe_2$ is metallic. The Pt-chalcogen covalent bond intensifies down the chalcogen group. Additionally, the interlayer interactions in Pt dichalcogenides are covalent, and just like the Pt-chalcogen bond, intensify as the chalcogen atom changes from sulphur to selenium to tellurium. This behaviour of Pt dichalcogenides results from the Pt bonding d orbitals and the chalcogen bonding p orbitals that are relatively close in energy than in other TMDs, and the difference in the energy becomes smaller and smaller down the chalcogen group. Herein, we report on the synthesis of $PtSe_2$ and $PtTe_2$ using the colloidal synthesis method for the first time and then applying them as electrocatalysts in alkaline HER.

As mentioned, developing 2D materials results in band gap development, particularly in PtS_2 and $PtSe_2$. Following this, $PtSe_2$ was explored as a photocathode in light-induced photo-electrochemical HER. Generally, semiconductors are poor electron transporters and one of the major requirements for an efficient PEC cathode is solar absorption, charge generation, and efficient charge separation. The charge separation properties of $PtSe_2$ were improved by supporting this material on highly conductive, mechanically, and thermally stable nitrogen-doped multi-walled carbon nanotubes (N-MWCNTs).

In Chapter 3, we report on the effect of varying selenium precursors from elemental selenium, sodium selenite to selenourea on the colloidal synthesis of $PtSe_2$ in a mixture of oleylamine and oleic acid at 320 ℃. All the reactions resulted in the formation of $PtSe_2$ although $PtSe_2$ prepared from selenourea is amorphous, evidenced by relatively broader XRD peaks and a smaller crystallite size. HER activity of the three $PtSe_2$ catalysts was evaluated in

1 M KOH at a scan rate of 5 mV/s and $PtSe_2$ prepared from selenium exhibited the earliest onset potential of 46 mV, overpotential of 162 mV, and a smaller Tafel slope of 112 $mVdec^{-1}$. This material exhibits the smallest resistance to electron transport and a high electrochemical surface area. We then explored the effect of altering tellurium precursor from elemental tellurium to tellurium tetrachloride, and sodium tellurite. Unlike the $PtSe_2$ synthesis, different platinum tellurite phases, $PtTe_2$, PtTe, and the mixed phase PtTe: $PtTe_2$ were produced from Te, $PtCl_4$, and sodium tellurite, respectively. Of the three, $PtTe_2$ exhibited the highest alkaline HER activity with an onset potential of 29 mV, an overpotential of 107 mV, and a Tafel slope of 79 $mVdec^{-1}$. In the same chapter, we compared the catalytic activity of $PtSe_2$ (prepared from Se) and $PtTe_2$ (prepared from Te) catalysts. We determined that $PtTe_2$ has a high surface roughness and electrochemical surface, leading to relatively higher activity than $PtSe_2$. However, $PtTe_2$ is metallic and therefore does not have a band gap, which implies that it cannot be employed in light-stimulated catalysis reactions.

In Chapter 4, we explored the use of $PtSe_2$ as a light-stimulated PEC alkaline HER catalyst. We used in situ colloidal synthesis to grow $PtSe_2$ on the walls of N-MWCNTs to improve the overall electron transport properties of $PtSe_2$. $PtSe_2$ anchored on N-MWCNTs was also studied in the dark and under illumination using 1 sun (100 mW/cm^2) to determine the influence of light on the HER catalytic activity of the hybrid materials. This study demonstrates that the light-stimulated HER activity of $PtSe_2$ improves when minimal amounts of N-MWCNTs are incorporated in the $PtSe_2$ sample matrix. This then leads to employing these materials as photocathodes in PEC HER.

Dedication

for my adorable grandmother, `Mathato Mxakaza, and my kids, Lesedi and Nkhabu

Acknowledgments

- First and foremost, I would like to thank God for giving me the courage to embark on this journey and to see it through.
- I would like to thank my supervisors, Dr. Z. N. Tetana and Prof. N. Moloto, for allowing me to do this research under their guidance. Thank you for holding my hand and giving me the support I needed.
- I would like to thank DSI-NRF CoE-SM and NRF for funding this work.
- I would like to thank the Microscopy and Microanalysis Unit (MMU), NMISA, University of Johannesburg, and CSIR for their contributions to this work.
- My greatest gratitude also goes to the research groups I was a member of, CATMAT and Nanowebs, for their input in making this work a success.
- I would like to thank my family in Lesotho and South Africa for supporting me in all ways possible.
- My friends, particularly Grace Ngubeni and Bonakele Mtolo, thank you so much for keeping me sane throughout this tough journey, for always picking up my calls when I wanted to talk about my frustrations with this work, and for your valuable input.
- I would like to thank my partner, Khali Makoae, for supporting my dreams and being my biggest cheerleader.

Presentations/ Conferences

1. Oral presentation at the 10th Annual Nanosciences Young Researcher's Symposium on the 7th and 8th of October 2021. (Virtual)

Title: Colloidal synthesis of Pt dichalcogenides ($PtSe_2$, $PtTe_2$) electrocatalysts for HER

2. Oral presentation at the Nanowebs progress meeting held at the University of the Witwatersrand on the 6th of May 2022.

Title: Performance evaluation of $PtTe_2$ electrocatalysts towards HER and OER

3. Flash presentation at the 13th postgraduate cross-faculty symposium held on the 11th to 15th of July 2022. (Virtual)

Title: Photo-electrochemical water splitting

4. Attended the Fluorescence spectroscopy workshop held on the 26th to 27th September 2022, at the University of the Witwatersrand.
5. Poster presentation at European School of Nanosciences and Nanotechnology held on the 28th of August to 10th September 2022 at Grenoble-France.
6. Oral presentation at the Wits PhD Seminar held on the 12th, 13th, and 16th of September 2022. (Virtual)

Title: Sustainable and innovative hydrogen energy production approach using Pt dichalcogenides ($PtSe_2$, $PtTe_2$)

7. Oral presentation at the 2nd Gauteng Catalysis Seminar held at Tshwane University of Technology, on the 28th of March 2023.

Title: Alkaline hydrogen evolution reaction of colloidally prepared $PtSe_2$ and $PtTe_2$ catalysts.

8. Oral presentation at the Nanowebs progress meeting held at the University of the Witwatersrand on the 30th of March 2023.

Title: Graphene quantum dots prepared via a simple calcination synthesis method.

9. Oral presentation at the Nanowebs progress meeting held at the University of the Witwatersrand on the 8th of June 2023.

Title: N-GQDs/$PtSe_2$ hybrid systems for HER

10. Oral presentation at the 9th Collaboration Symposium held at Sefako Makgatho University, Pretoria from the 2nd to 3rd of November 2023.

Title: Alkaline hydrogen evolution reaction of $PtSe_2$ and $PtSe_2$/N-MWCNT

11. Attended the South African National Energy Development Institute (SANEDI) first annual energy conference held on the 21st to 22nd November 2023 at Emperors Palace Convention Centre, Johannesburg.

Publications

Lineo F. Mxakaza, Victor Mashindi, Cebisa E. Linganiso, Nosipho Moloto, Zikhona N. Tetana, "Evaluating the hydrogen evolution reaction activity of colloidally prepared $PtSe_2$ and $PtTe_2$ catalysts in an alkaline medium" *ChemistryOpen*, 2024, e202400146.

Lineo Mxakaza, Grace Ngubeni, Nosipho Moloto, Zikhona Tetana, "Cu_2ZnSnS_4/N-MWCNTs hybrid systems as counter electrode substitutes for platinum in dye-sensitized solar cells" *Journal of Materials Research*, 2024, 689 - 701.

Grace N. Ngubeni, Olusola Akinbami, **Lineo Mxakaza**, Siyabonga Nkabinde, Tshwarela Kolokoto, Francis Otieno, Makwena J. Moloto, Kalenga P. Mubiayi, Nosipho Moloto, "Evaluating the effect of the substrate on the electrocatalytic performance of Cu_2ZnSnS_4 and $Cu_2ZnSnSe_4$ counter electrodes in dye-sensitized solar cells" *Thin Solid Films*, 2022, 139099.

Mildred A. Airo, Francis Otieno, **Lineo Mxakaza**, Adewale Ipadeola, Rudo S. Kadzutu-Sithole, Lerato F. E. Machogo-Phao, Caren Billing, Makwena Moloto, Nosipho Moloto, "Probing the stoichiometry dependent catalytic activity of nickel selenide counter electrodes in the redox reaction of iodide/triiodide electrolyte in dye-sensitized solar cells" RSC Advances, 2020, 39509-39520.

Table of Contents

List of Figures

List of Tables

List of Abbreviations

ΔG_H -Hydrogen adsorption energy

^1H - proton

2D -Two-dimensional

APCE - Absorbed photon to current efficiency

b - Tafel slope

BE - Binding energy

CB - Conduction band

CCS - Carbon capture and storage

C_{dl} - Double layer capacitance

C_m - Monomer concentration

CV - Cyclic voltammetry

CVD - Chemical vapor deposition

D_p - Crystallite size

e^- - Electron

E_a - Activation energy

ECSA - Electrochemical surface area

EDS – Energy dispersive X-ray spectroscopy

E_f - Fermi level

EIS - Electrochemical impedance spectroscopy

Eqn. - Equation

F - Faraday constant

FE - Faradaic efficiency

FTIR - Fourier transform infra-red

FWHM - Full width half maximum

GC - Glassy carbon

h - Hour

h^+ - Holes

H^+ - Hydrogen ion

HER - Hydrogen evolution reaction

HOR – Hydrogen oxidation reaction

HRTEM - High-resolution transmission electron microscopy

IPCE - Incident photon to current efficiency

J - Current density

J_o – Exchange current density

K - Shapeless dimension factor

MBE - Molecular beam epitaxy

ME - Mechanical exfoliation

MH - Metal hydrogen

NMR - Nuclear magnetic resonance

N-MWCNTs - Nitrogen-doped multiwalled carbon nanotubes

O.A. - Oleic acid

OER - Oxygen evolution reactiom

OH^- - Hydroxide ion

OLA - Oleylamine

ORR - Oxygen reduction reaction

PEC - Photo-electrochemical

pH - Potential hydrogen

Pt/C - Platinum on carbon

PGM – Platinum group metals

PtX_2 - Platinum dichalcogenides

R - Real gas constant

R_{ct} - Charge transfer coefficient

RF - Radiofrequency

RHE - Reference hydrogen electrode

R_s - Solution resistance

SC - Semiconductor

SeU - Selenourea

T - Temperature

TAC - Thermally assisted conversion

TEM - Transmission electron microscope

TGA - Thermogravimetric analysis

TMDs - Transition metal dichalcogenides

TOF - Turnover frequency

TOP - Trioctylphosphine

UV-Vis - Ultraviolet-visible spectroscopy

VB - Valence band

XPS - X-ray photoelectron spectroscopy

XRD - X-ray diffraction

η - Overpotential

η_{-10} - Overpotential at -10 $mAcm^{-2}$

Thesis Synopsis

Pt dichalcogenides are layered 2D materials that offer exposed edge sites, band gap generation, and reduced amounts of Pt. The interlayer interactions of Pt dichalcogenides intensify as one progresses down the chalcogen group, making the electronic properties of these materials immensely dependent on the chalcogen atom. Pt dichalcogenides have been explored as counter electrodes in dye-sensitized solar cells, optoelectronic devices, and hydrogen evolution reactions. We explored colloidal synthesis for the preparation of $PtSe_2$ and $PtTe_2$ nanomaterials and their catalytic activity towards alkaline hydrogen evolution reaction. Colloidal synthesis offers the opportunity for sustainable development of Pt dichalcogenide-based HER devices because of the relatively high quantities of nanomaterials that are produced through this procedure. The band gap of $PtSe_2$ can be tuned by altering the number of layers of this material. As such, $PtSe_2$ can be used as a photoelectrode in PEC hydrogen evolution reactions. The conductivity of $PtSe_2$ can be improved by hybridizing this material with carbon materials. Nitrogen-doped multi-walled carbon nanotubes enhance the conductivity and stability of TMDs.

Chapter 1

General Background

1.1 Problem Statement

Energy, transport and infrastructure, agriculture, and industry sectors are the primary emitters of greenhouse gases. Their percentage contributions are highlighted in Figure 1.1 (a) and attribute the energy sector to the largest source of CO_2 emissions in the atmosphere.[1] CO_2 exacerbates climate change which in turn contributes to the detriment of the respiratory systems of living beings on earth and the overall health of the planet. Generally, two approaches are taken to reduce the carbon footprint; avoid the CO_2 emission altogether or remove emitted CO_2 in various industrial processes. The latter process implements Carbon Capture and Storage (CCS) strategies to trap CO_2 from industrial plants and store it in underground rock formations. Although attractive, CCS does not provide a sustainable energy solution for the future.[2] Alternatively, industrial processes that have zero CO_2 emissions are sought after and implemented to address the global warming issue.[3] These include the use of renewable energy sources and hydrogen fuel economy. Hydrogen does not exist as a free element, its production processes are complicated, and its storage is unswerving and costly. This has led to a slow advancement of the hydrogen economy.[2] Hydrogen can be harnessed from various sources, highlighted in Figure 1.1 (b), such as natural gas, oil, and coal. Natural gas accounts for the largest current source of H_2 at 71.3 %.[4] These carbon-based fuels pose a danger to the environment by releasing CO_2 into the atmosphere during H_2 production. Water is a hydrogen reserve that can be decomposed using electricity to generate H_2 and O_2 molecules through a water electrolysis system.[5] The amount of energy required to initiate water electrolysis can be reduced by using catalyst materials. Additionally, renewable energy systems can be coupled with the water electrolysis setup to generate photo-electrochemical water-splitting devices to alleviate the water electrolysis energy feedstock.[6] Catalyst development for water electrolysis is a hot area of research as cheaper and earth-abundant catalysts are sought after to replace the conventional high-cost Pt and Ru-based water-splitting electrodes.[7,8] It is a mission to find hydrogen evolution reaction catalysts that surpass the activity of Pt. Doping of catalysts with minimal amounts of Pt or reducing the overall quantity of Pt in platinum compounds such as developing Pt dichalcogenides (PtX_2, X=S, Se, Te), are some strategies aimed at the sustainability of platinum-based HER devices.

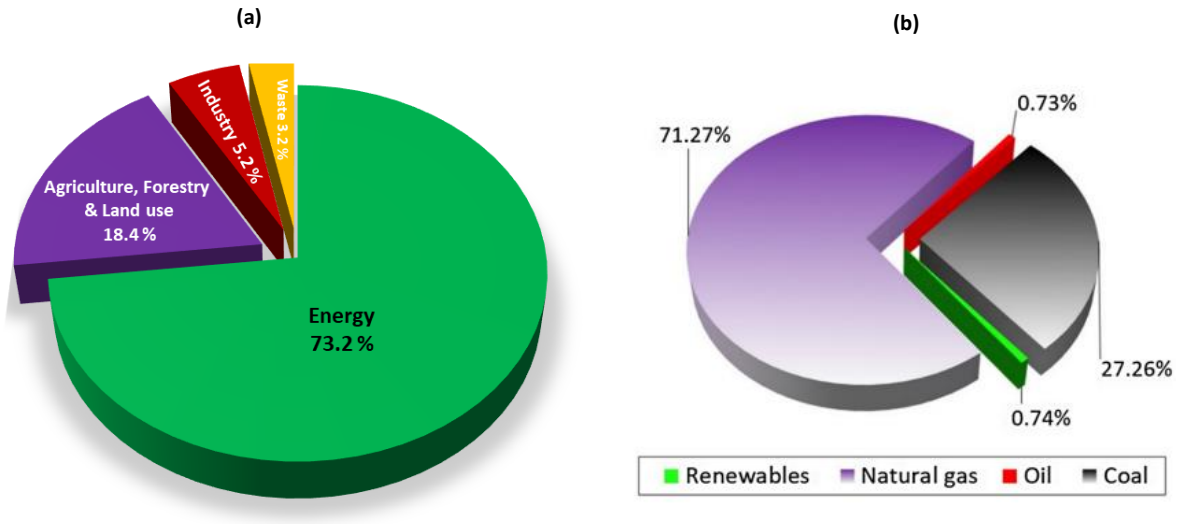

Figure 1.1: The CO_2 gas emission into the atmosphere by sectors,[1] and (b) global hydrogen energy production by source.[9]

PtS_2, $PtSe_2$, and $PtTe_2$ are proposed as HER catalysts because they have comparable HER activity to Pt, although they have relatively lower quantities of Pt. PtX_2 demonstrates interesting layer and chalcogen-dependent properties.[10,11] Their electronic properties change from semi-conductor to semi-metallic and metallic when the chalcogen atom is changed from sulfur to selenium, to tellurium in PtS_2, $PtSe_2$, and $PtTe_2$, respectively.[11–13] The exploration of PtX_2 in HER is a fresh area of research. Extensive studies on the employment of group 6 transition metal dichalcogenides (TMDs) for HER have inspired the investigation of PtX_2 towards various electrochemical reactions. The most popular method for the preparation of PtX_2 is the thermally assisted method which involves sputtering Pt onto a substrate followed by vaporization and deposition of the chalcogen precursor using chemical vapor deposition methods.[14] This method does not allow for large-scale synthesis of PtX_2. The colloidal synthesis method has been previously employed for the preparation of TMDs and offers the advantage of material post-synthesis treatment, morphology, layer, and size manipulation as well as scaling up.[15] This means that this method can drive the sustainability of devices based on colloidally prepared catalysts. As a result, colloidal synthesis was explored for the first time, to prepare PtX_2 in this research. TMDs have also been applied in photo-electrochemical (PEC) cells as photoelectrodes to drive the oxygen or the hydrogen evolution reactions using light energy.[16–18] The exposed edge sites, vacancies, and suitable optical properties of TMDs render them suitable photocathodes.[19] Marrying the TMDs with carbon materials is reported to be an effective approach to developing multifunction catalysts.[20–22] Generally, carbon nanotubes can endure steady current, show good chemical and thermal stabilities, and most importantly, have good electron properties. The synergetic effects of

hybridizing TMDs with carbon nanotubes are crucial in PEC photoelectrodes because they improve the overall stability of the electrode, the conductivity as well as charge generation and separation.[23,24] In this study, the PtX_2, and carbon nanotube composites have been explored as PEC hydrogen evolution reaction photocathodes. The growth of PtX_2 on the walls of the carbon nanotubes has not been reported in the literature.

1.2 Motivation and Rationale

Group 10 dichalcogenides, particularly PtX_2 demonstrate more dramatic layer-dependent properties than other TMDs. The Pt bonding d orbitals and the chalcogen p orbitals lie at proximity energy levels and the interaction of these orbitals results in a greater hybridization relative to group 6 TMDs.[25,26] Therefore, the conventional van de Walls interactions in TMDs are reported to diminish in these compounds; rather, a more covalent bonding occurs. Additionally, the covalent bonding nature of the PtX_2 intensifies down the chalcogen group, that is Pt-Te has a higher bonding energy than Pt-S bond. The evaluation of chalcogen dependence of PtX_2 on the electrocatalytic HER makes for an interesting study. PtX_2 are layered materials and make for reduced use of Pt and more exposed catalytic sites. The properties of Pt can be extended by developing Pt-based 2D materials which instigate band gap development, thus making these materials suitable to use in light-stimulated catalysis. Generally, the development of 2D Pt dichalcogenides produces layered structures with exposed catalytic edge sites and band gaps, which makes these materials photoactive and therefore extends their use to photo-electrochemical devices. Synthesis methods reported for PtX_2 suffer from restrictions in large-scale production. The colloidal synthesis of these compounds has not been explored. This study bridges the gap on minimal research on PtX_2 in electrochemical, photoelectrochemical studies, and colloidal synthesis. Electrochemical energy storage reactions (HER, oxygen evolution reaction (OER)) and energy conversion reactions (Hydrogen oxidation reaction (HOR), oxygen reduction reaction (ORR)) are often hindered by high overpotentials and slow kinetics, particularly in alkaline medium.[27–29] Stable and efficient catalysts that can simultaneously the energy storage and conversion reactions are crucial in overcoming these hindrances and allow for the sustainability of devices based on these reactions. Pt has a good reputation in electrocatalysis and various morphologies,[30,31] compositions,[32,33] and crystal phases[34,35] of Pt have been explored in the quest to find the most efficient electrocatalyst. Pt-based catalysts' performance and stability highly depend on the choice of the electrolyte. Although fast HER/HOR reaction rates are observed in acid medium on Pt catalysts, even at low catalyst loadings, the counteracting reactions (OER/ORR, respectively) require much higher Pt catalyst loadings, thereby restricting the sustainability of these devices.[36] One of the solutions is to

employ alkaline electrolytes, resulting in cheaper devices because of the low cost of anion exchange membranes, and abundant catalysts for OER/ORR reactions. Often the catalytic performance of the catalysts is lowered by their poor stability, and this can be counteracted by hybridizing the catalysts with carbon materials. Nitrogen-doped multi-walled carbon nanotubes are chemically, and mechanically stable carbon allotropes often used as support structures for TMD. They are highly conductive and improve the electron transport properties of TMD when these chalcogenides are grown on their surface. The TMD/carbon nanotube composites can be employed as photoelectrodes in PEC water-splitting devices because of the synergistic effects, including enhanced stability, improved conductivity, and charge separation that follows photo-absorption and charge generation.

1.3 Hypothesis

The development of 2D metal dichalcogenides materials results in the formation of layered materials that have more exposed catalytic sites and have reduced metal loading compared to the corresponding metal nanoparticle. The reduction of the metal loading and production of more exposed sites results in catalysts that show either improved catalytic activities or comparable catalytic activities to metal catalysts.

1.4 Research Questions

- Can colloidal synthesis be employed to prepare powdered Pt dichalcogenides?
- How does the catalytic activity of Pt dichalcogenides compare to Pt and does the morphology of the Pt dichalcogenides influence the HER activity of these catalysts?
- Can the band gap of the semi-conductor $PtSe_2$ be modified by growing this material on the walls of nitrogen-doped multi-walled carbon nanotubes? And can this extend the use of $PtSe_2$ to light-induced HER?

1.5 Aims and Objectives

The main objective of this research is to synthesize platinum selenide (PtSe) and platinum telluride (PtTe) electrocatalysts using a colloidal synthesis method and investigate their performance as catalysts for the hydrogen evolution reaction (HER) in an alkaline environment. Additionally, the study aims to assess the efficacy of $PtSe_2$ grown in situ on nitrogen-doped multi-walled carbon nanotubes ($PtSe_2$/N-MWCNTs) as a photocathode material in photo-electrochemical (PEC) HER under alkaline conditions. The following objectives were executed to achieve these goals.

- The effect of varying Se precursor on the colloidal synthesis of platinum selenide was evaluated.
- The effect of varying Te precursor on the colloidal synthesis of platinum telluride was evaluated.
- The alkaline catalytic activities of platinum selenide and platinum telluride catalysts were studied.
- $PtSe_2$ on N-MWCNTs was grown by an in situ colloidal synthesis method.
- The light-stimulated alkaline hydrogen evolution reaction of $PtSe_2$/N-MWCNTs was studied.

1.6 Delimitations of the Study

- Colloidal synthesis of PtS_2
- Effect of varying the Pt precursor on $PtSe_2$ and $PtTe_2$
- HER of $PtSe_2$ anchored on N-MWCNTs

1.7 Thesis Outline

Chapter 1: Highlights the current energy demands and drive to move towards hydrogen energy. This study's problem statement and motivation are highlighted and aims and objectives are outlined.

Chapter 2: Highlights the details of the background of hydrogen energy and the conventional strategies for H_2 generation. HER performance indicators are explained. A background on Pt dichalcogenides and their synthesis methods are explained. Colloidal synthesis as a preparation technique for TMDs is detailed. Photo-electrocatalytic hydrogen evolution is introduced, and the development and advantages of TMDs-carbon composites and their applications as photoelectrodes in PEC water-splitting devices are highlighted. Common performance parameters for evaluating photocathode performance in light-stimulated PEC HER are described.

Chapter 3: Outlines the effect of the selenium precursor on the colloidal synthesis of $PtSe_2$ and the different $PtSe_2$ nanomaterials are evaluated as potential alkaline HER electrocatalysts and the best $PtSe_2$ HER catalyst was identified. Chapter 3 also describes the effect of the tellurium precursor on the colloidal synthesis of $PtTe_2$ in a mixture of oleylamine and trioctylphosphine. The different phases of platinum telluride obtained were evaluated for HER and the best $PtTe_2$ HER catalyst was

identified. The alkaline HER performance of $PtSe_2$ (prepared from Se) and $PtTe_2$ were compared and the best HER Pt dichalcogenide catalyst was identified.

Chapter 4: Describes the in-situ growth of $PtSe_2$ on the walls of the N-MWCNTs by colloidal synthesis method. 3, 5, and 10 weight % of N-MWCNTs were incorporated in the $PtSe_2$ matrix to generate $PtSe_2$/N-MWCNTs (0.03), $PtSe_2$/N-MWCNTs (0.05), $PtSe_2$/N-MWCNTs (0.1) composites. The light-stimulated HER of these catalysts in 1 M KOH was evaluated and the composite giving the best HER performance was identified.

Chapter 5: Highlights the conclusions and the general recommendations for the future work of this study.

1.8 References

1. https://ourworldindata.org/emissions-by-sector accessed 14th Feb 2024.
2. Safari, F. & Dincer, I. A review and comparative evaluation of thermochemical water splitting cycles for hydrogen production. *Energy Convers Management* 205, 112182 (2020).
3. Matthews, H. & Wynes, S. Current global efforts are insufficient to limit warming to 1.5°C. *Sci* 375, (2022).
4. MacDowell, N. *et al.* The hydrogen economy: A pragmatic path forward. *Joule* 5, 2524 - 2529 (2021).
5. Shiva Kumar, S. & Lim, H. An overview of water electrolysis technologies for green hydrogen production. *Energy Reports* 8, 13793 - 13813 (2022).
6. Krol, R. van de & Gratzel, M. Photoelectro-chemical hydrogen production. *Spinger*, New York, (2012).
7. Danilovic, N. *et al.* Activity-stability trends for the oxygen evolution reaction on monometallic oxides in acidic environments. *J Phys Chem Lett* 5, 2474 - 2478 (2014).
8. Norskov, J. K. & Christensen, C. H. Toward efficient hydrogen production at surfaces. *Sci* 312, 1322 - 1323 (2006).
9. Dincer, I. & Zamfirescu, C. Sustainable hydrogen production options and the role of IAHE. in *Int J Hydrog Energy* 37, 16266 - 16286 (2012).
10. Mirõ, P., Ghorbani-Asl, M. & Heine, T. Two dimensional materials beyond MoS_2: Noble-transition-metal dichalcogenides. *Angew Chem Int Ed* 53, 3015 - 3018 (2014).
11. Chia, X. *et al.* Layered platinum dichalcogenides (PtS_2, $PtSe_2$, and $PtTe_2$) Electrocatalysis: Monotonic dependence on the chalcogen size. *Adv Funct Mater* 26, 4306 -4318 (2016).

12. Soled, S., Wold, A. & Gorochov, O. Crystal growth and characterization of several platinum sulfoselenides. *Mat Res Bull*, 9 - 16 (1976).

13. Hulliger, F. Electrical properties of some nickel-group chalcogenides. *Journal of Physics and Chemistry of Solids* 26, 639 - 645 (1965).

14. Tong, X. W. et al. Direct tellurization of Pt to synthesize 2D $PtTe_2$ for high-performance broadband photodetectors and NIR image sensors. *ACS Appl Mater Interfaces* 12, 53921 - 53931 (2020).

15. Airo, M. A. et al. Probing the stoichiometry dependent catalytic activity of nickel selenide counter electrodes in the redox reaction of iodide/triiodide electrolyte in dye sensitized solar cells. *RSC Adv* 10, 39509 - 39520 (2020).

16. Behera, G. C. et al. WS_2 nanosheets functionalized Fe_2O_3 nanorod arrays as a type II heterojunction for photoelectrochemical water splitting. *Appl Surf Sci Adv* 11, 100293 (2022).

17. Tian, Y. et al. Photo-electrocatalytic hydrogen evolution reaction stimulated by the surface plasmon resonance effect of copper and silver surrounded with MoS_2. *RSC Adv* 13, 25246 - 25252 (2023).

18. Kwon, K. C. et al. Wafer-scale transferable molybdenum disulfide thin-film catalysts for photoelectrochemical hydrogen production. *Energy Environ Sci* 9, 2240 - 2248 (2016).

19. Jun, S. E., Lee, J. K. & Jang, H. W. Two-dimensional materials for photoelectrochemical water splitting. *Energy Advances* 2, 34 - 53 (2023).

20. Ndala, Z. B. et al. Electrocatalytic activity of pristine and electrochemically activated $SnSe_2$ nanoplates for the hydrogen evolution reaction. *J Electroanal* 918, 116464 (2022).

21. Ndala, Z. et al. Evaluating the effect of varying the metal precursor in the colloidal synthesis of $MoSe_2$ nanomaterials and their application as electrodes in the hydrogen evolution reaction. *Nanomater* 10, 1 - 14 (2020).

22. Ndala, Z. B. et al. Unravelling the effects of surface functionalization on the catalytic activity of $ReSe_2$ nanostructures towards the hydrogen evolution reaction. *Appl Surf Sci* 612, 155971 (2023).

23. Vidhya, M., Selvakumari, T. M., Marnadu, R. & Ashraf, I. M. MoS_2 blended MWCNT hybrid nanocomposites and its enhanced super capacitive features. *Solid State Commun* 375, 115345 (2023).

24. Wei, B. Q., Vajtai, R. & Ajayan, P. M. Reliability and current carrying capacity of carbon nanotubes. *Appl Phys Lett* 79, 1172 - 1174 (2001).

25. Dai, D. et al. Trends in the structure and bonding in the layered platinum dioxide and dichalcogenides PtQ_2 (Q = O, S, Se, Te). *J Solid State Chem* 173, 114 - 121 (2003).

26. Chia, X. et al. Layered platinum dichalcogenides (PtS_2, $PtSe_2$, and $PtTe_2$) electrocatalysis: Monotonic dependence on the chalcogen size. *Adv Funct Mater* 26, 4306 - 4318 (2016).
27. Yang, X., Lin, L., Guo, X. & Zhang, S. Design of multifunctional electrocatalysts for ORR/OER/HER/HOR: Janus makes difference. *Small* 2404000 (2024).
28. Sheng, W., Gasteiger, H. A. & Shao-Horn, Y. Hydrogen oxidation and evolution reaction kinetics on platinum: Acid vs alkaline electrolytes. *J Electrochem Soc* 157, B1529 (2010).
29. Khusnun, N. F. *et al.* An avant-garde of carbon-doped photoanode materials on photo-electrochemical water splitting performance: A review. *J Electroanal Chem* 929, 117139 (2023).
30. Hansen, J. N. *et al.* Is there anything better than Pt for HER? *ACS Energy Lett* 6, 1175 -1180 (2021).
31. Takimoto, D. *et al.* Platinum nanosheets synthesized via topotactic reduction of single-layer platinum oxide nanosheets for electrocatalysis. *Nat Commun* 14, 19 (2023).
32. Strmcnik, D. *et al.* Improving the hydrogen oxidation reaction rate by promotion of hydroxyl adsorption. *Nat Chem* 5, 300 - 306 (2013).
33. McCrum, I. T. & Koper, M. T. M. The role of adsorbed hydroxide in hydrogen evolution reaction kinetics on modified platinum. *Nat Energy* 5, 891 - 899 (2020).
34. Kuzume, A., Herrero, E. & Feliu, J. M. Oxygen reduction on stepped platinum surfaces in acidic media. *J Electroanal Chem* 599, 333 - 343 (2007).
35. Brandes, B. A. *et al.* Unifying the ORR and OER with surface oxygen and extracting their intrinsic activities on platinum. *Nat Commun* 15, 7336 (2024).
36. Tian, X., Zhao, P. & Sheng, W. Hydrogen evolution and oxidation: Mechanistic studies and material advances. *Adv Mat* 31, 1808066 (2019).

Chapter 2

Literature review

2.1 Background on Hydrogen Energy

The employment of fossil fuels for energy production has aided the advancement of the global economy through improved industrialization. The recent oil price hikes, escalating energy utilization, probable fossil fuel reserve depletion, and the accompanying CO_2 emissions threaten fossil fuel energy and economic security.[1] To warrant sustainable energy in the future calls for CO_2 emission reduction and transformation to renewable energy sources. Strategies for reducing the CO_2 levels in the atmosphere include CO_2 capture and storage, and the development of zero CO_2 emitting energy sources.[2] Hydrogen energy, since its inception, has been regarded as the "Messiah" of sustainable and clean energy sources. Hydrogen is the lightest (molecular weight of 2.02 $gmol^{-1)}$, most abundant chemical element, and constitutes over 75 % of normal matter. Combustion of 2 moles of H_2 generates a total energy of 286 $kJmol^{-1}$, as shown in Eqn. 2.1 with only steam as a side product. 1 kg of H_2 carries energy equivalent to 141 MJ, 6 times higher than coal and 3 times higher than natural gas and gasoline.[1,3,4]

$$\mathbf{2H_2(g) + O_2\ (g) \rightarrow 2H_2O\ (g) + \ -286\ kJmol^{-1}}\text{.....Eqn. 2.1}$$

Hydrogen is used in the chemical sector as feedstock in steel, methanol, and ammonia production (Figure 2.1). As it stands, the hydrogen production pathways, highlighted in Figure 2.1 rely mainly on non-renewable sources, which further increases the CO_2 emissions.[5] Nonetheless, the possibility of producing green hydrogen from water electrolysis coupled with renewable energy sources such as wind, solar, and biomass exists but is restricted by technology development and high-cost implications. Research is therefore channelled towards reducing the overall cost of water electrolysers by optimizing individual components of such devices.

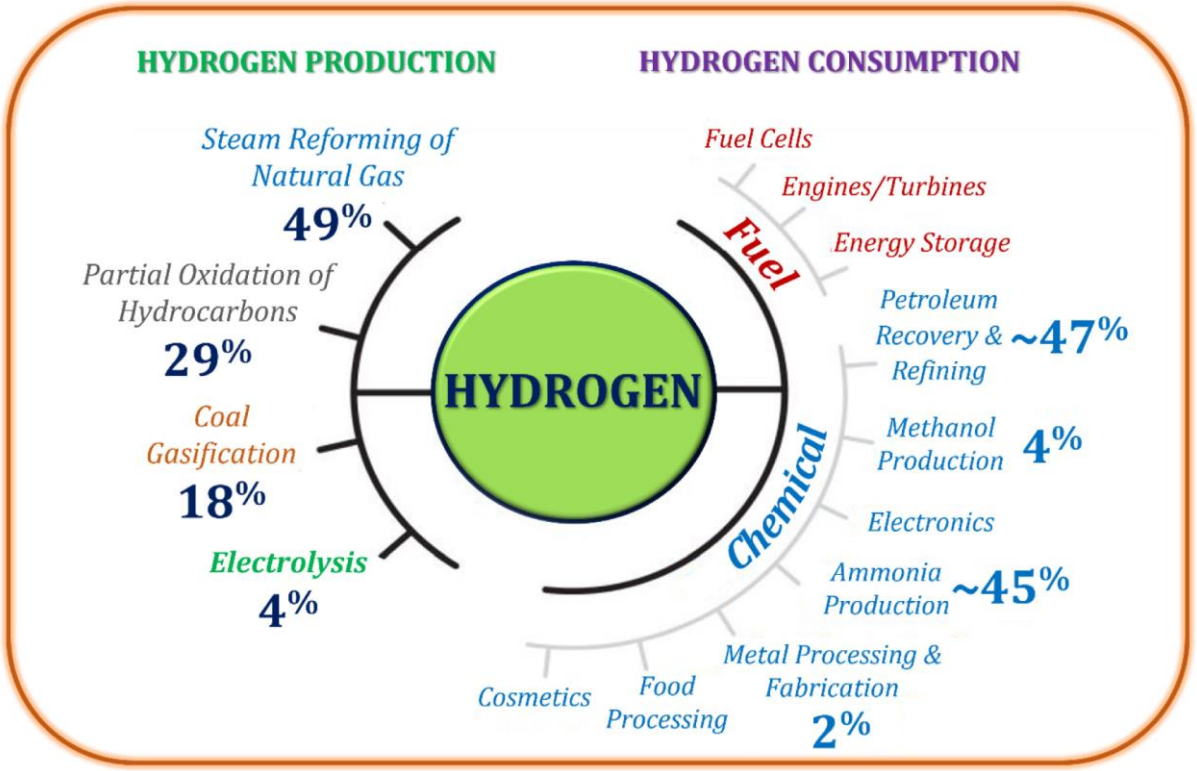

Figure 2.1: Hydrogen production methods and uses with respective percentage contributions.[6]

2.2 Introduction to Electrochemical Water Splitting

In the water electrolysis cell, hydrogen is produced at the cathode while oxygen is produced at the anode, as depicted in Figure 2.2. Electricity is employed to split H_2O molecules into O_2 and H_2. A theoretical voltage of 1.23 V is required to drive this reaction, although surplus energy is needed to ensure an adequate water-splitting reaction rate.[7,8] The reactions at the respective electrodes are shown in Eqn. 2.1 and 2.2 and are referred to as oxygen evolution reaction (OER) and hydrogen evolution reaction (HER). A half-cell that only has either the anode component (OER) or the cathode component (HER) of the electrolysis cell, can be assembled to study the performance of the specific electrode.[9] The electrolyte and the anode material play an important role in the HER kinetics.[10] Water is a poor electrical conductor, which can be enhanced by adjusting its pH through the addition of an electrolyte. In low-pH electrolytes (acidic), the current is carried by H^+ ions, whereas in higher-pH electrolytes, OH^- ions conduct the current. Alternatively, for a more sustainable water-splitting process, light can be used to provide the voltage required to initiate the water dissociation, a process referred to as photo-electrochemical (PEC) water splitting.

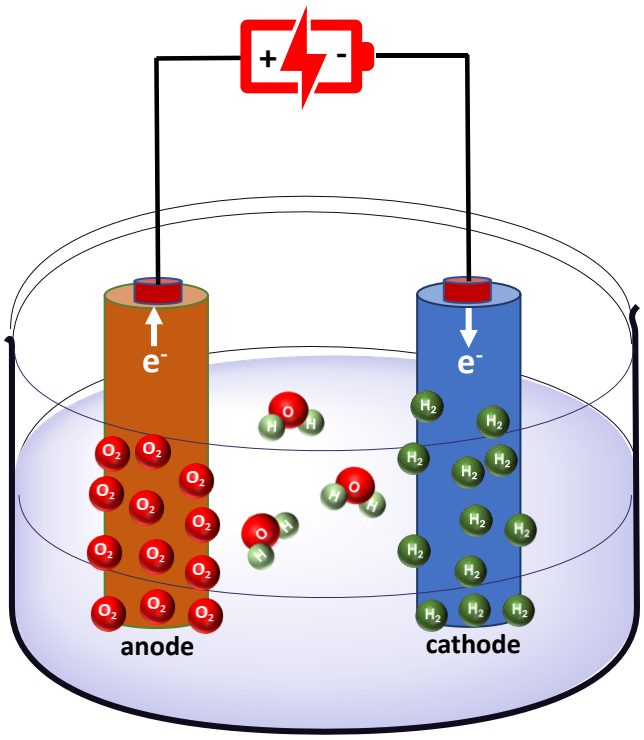

Figure 2.2: A typical water electrolysis cell.[8]

Anode reaction: $2H_2O_{(l)} \rightarrow O_{2(g)} + 4H^+_{(aq)} + 4e^-_{(aq)}$**……Eqn. 2.2**

Cathode reaction: $2H^+_{(aq)} + 2e^-_{(aq)} \rightarrow 2H_{2(g)}$**……Eqn. 2.3**

Overall reaction: $2H_2O_{(l)} \rightarrow 2H_{2(g)} + 2O_{2(g)}$ **……Eqn. 2.4**

2.3 Introduction to Photo-electrochemical Water Splitting

Photoelectrochemical (PEC) water splitting involves photo-absorption by a semiconductor material, generating electron-hole pairs that facilitate the water electrolysis. Generally, PEC devices integrate light absorption and electrocatalysis in a single device. The holes (h^+) oxidize water at the anode surface to O_2 and e^- reduce H^+ ions on the cathode to H_2 (Figure 2.3).[11] The direct transformation of light energy to chemical energy (O_2 and H_2) highlights the prospect of converting solar energy into energy that can be easily stored. Vital standards that should be synchronized for efficient PEC water splitting include adequate voltage production by the semiconductor material, generated e^- should only be employed for water splitting rather than side reactions such as corrosion, the electrodes should demonstrate excellent stability in the electrolyte, and electrode band-edge potentials should match the potentials for the reduction and oxidation reactions.[12–14]

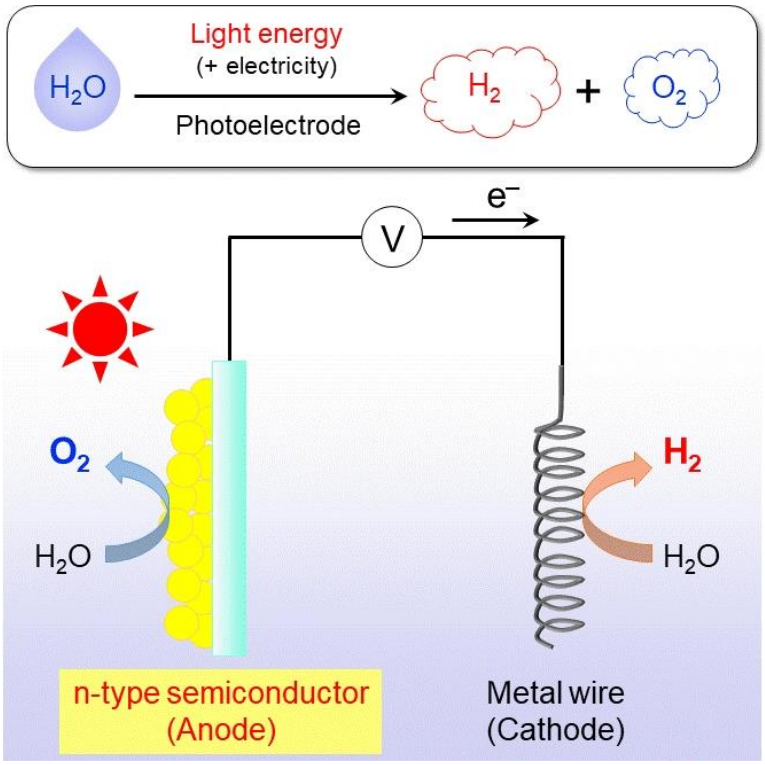

Figure 2.3: PEC water splitting device constructed from an n-type semiconductor and metal wire cathode.[15]

2.4 Alkaline Hydrogen Evolution Reaction

The reactions occurring in an alkaline medium are illustrated in Eqn. 2.5 - Eqn. 3.7 and the corresponding mechanism is demonstrated in Figure 2.4. Initially, water molecules undergo dissociation on the catalyst surface (M) to form hydroxyl ions and adsorbed hydrogen atoms (MH) in the Volmer step.[16] Subsequently, the adsorbed hydrogen atoms combine to regenerate the catalyst surface and produce H_2 in the Tafel step. Alternatively, continuous dissociation of H_2O molecules, along with simultaneous interaction with adsorbed hydrogen and electrons, produces H_2 in the Heyrovsky step.[17,18]

Volmer: $M + H_2O_{(l)} + e^-_{(aq)} \rightarrow MH_{ads} + OH^-_{(aq)}$ **……Eqn. 2.5**

Tafel: $MH_{ads} + MH_{ads} \rightarrow 2M + H_{2(g)}$ **……Eqn. 2.6**

Heyrovsky: $MH_{ads} + H_2O_{(l)} + e^-_{(aq)} \rightarrow M + H_{2(g)} + OH^-_{(aq)}$ **……Eqn. 2.7**

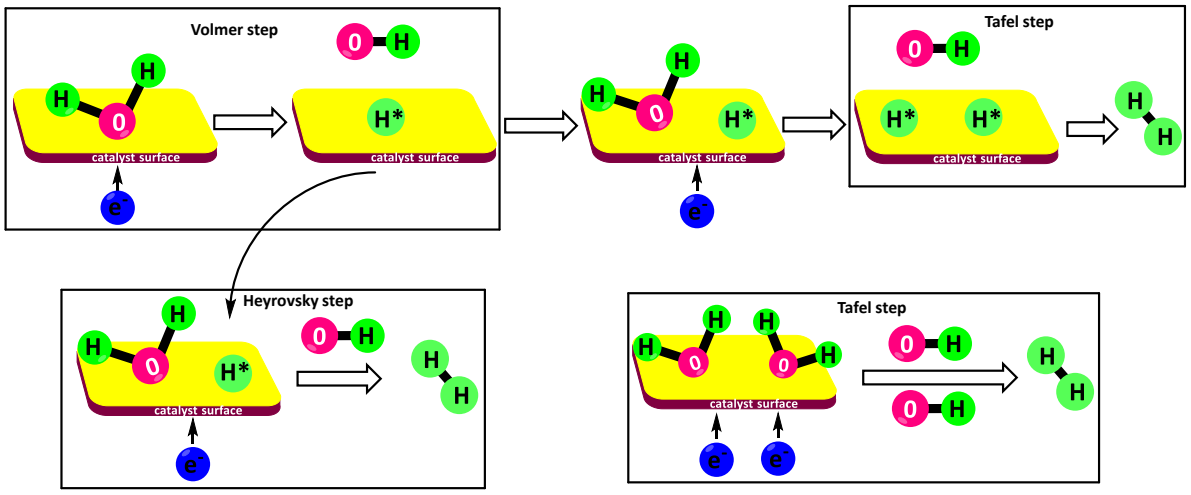

Figure 2.4: The HER mechanism in an alkaline medium

2.5 Hydrogen Evolution Reaction Catalysts

The rate of H_2 generation is predominantly controlled by the extent of interaction between the metal surface (M) and hydrogen atoms (H) and the desorption of H_2 molecules post the reduction process. For a weak MH interaction, few MH intermediates are formed thus the production of H_2 because of MH-MH interactions is restricted, and the overall H_2 production rate declines. On the other hand, if the interaction of the metal surface and H_2 is high, then the desorption of H_2 from the metal surface is hindered and ultimately the catalyst's active sites are blocked. Thus, a HER catalyst must have optimal hydrogen atom (MH) adsorption to allow efficient HER. This is supported by Sabatier`s principle of catalysis, which states that the adsorption energy of intermediates and products should neither be too high nor too low. That is, the free energy of hydrogen adsorption (ΔG_H) should be as close to zero as possible.[19,20] The relationship between the reaction rate and the free energy of adsorption is given by a volcano plot, depicted in Figure 2.5 (a). The volcano plot shows two regions, the ascending region where $\Delta G_H > 0$ and the descending region where $\Delta G_H < 0$. The tip of the two regions is where ΔG_H corresponds to the maximum reaction rate. When the $\Delta G_H > 0$, MH adsorption is weak resulting in increasing j_0 as ΔG_H decreases and approaches zero. Otherwise, when $(\Delta G_H) < 0$, j_0 decreases as the reaction rate declines. According to this plot, platinum group metals give the highest HER rate. More recently, the volcano plot has been reconstructed as more research is done. Figure 2.5 (b) shows the alkaline volcano plot which shows that the reaction rate increases in the region $\Delta G_H < 0$, whereas the reaction rate declines when $\Delta G_H < 0$. According to this plot, Pt, iridium (Ir), and palladium (Pd) are the best HER catalysts in an alkaline medium.[19,21]

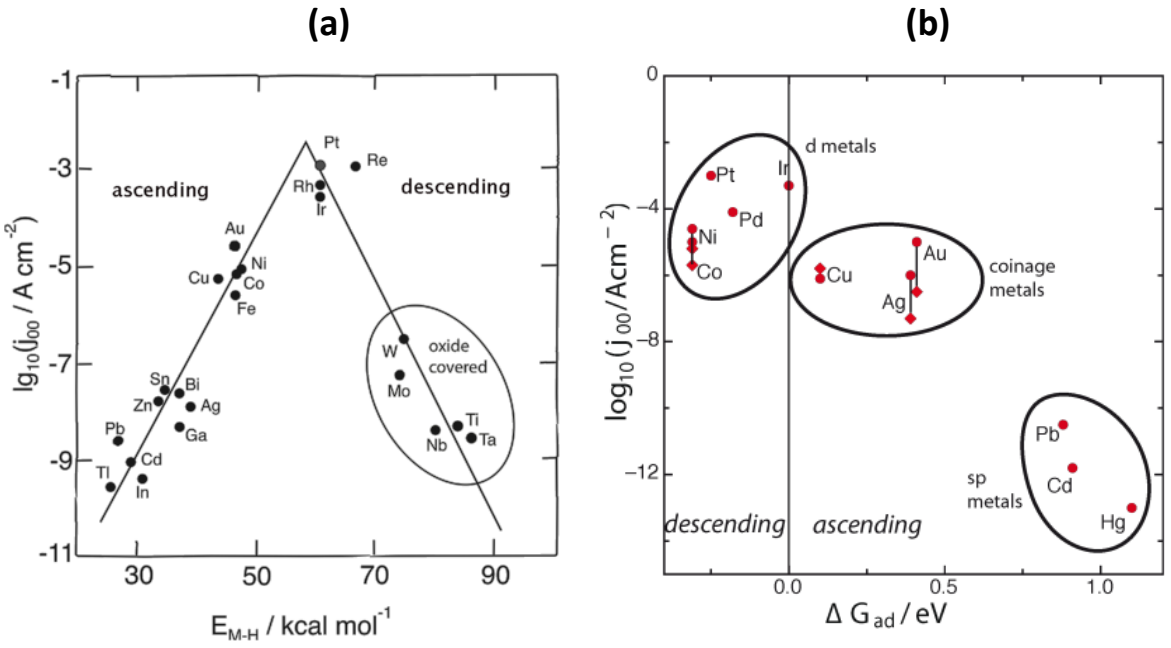

Figure 2.5: (a) Trassati volcano plot,[22] and (b) volcano plot for alkaline hydrogen evolution reaction.[21]

2.6 HER Performance Parameters

2.6.1 Overpotential

For any electrochemical reaction, the potential applied to initiate the reaction deviates from the equilibrium potential because of the reaction activation barrier, ion diffusion, and ion resistance to movement. This potential difference is referred to as overpotential (η). Overpotential is determined from a plot of applied potential against current density as shown in Figure 2.6 (a).

a) Onset Potential

As the potential is increased from the positive to the negative direction, the current density usually does not change until a potential is reached where a current density change is observed. This region, indicated by a box in Figure 2.6 (a), is the point at which hydrogen starts being produced. It is the activation potential for instigation of the HER. The catalytic activity of individual catalysts is directly related to the onset potential, with a low onset potential indicating a high activity.

b) Overpotential at -10 mAcm^{-2}

Universally, the η at -10 mAcm^{-2} (η_{-10}) is used to compare various catalyst materials. A large η_{-10} suggests that the relative HER efficiency is low, and the reverse is true.

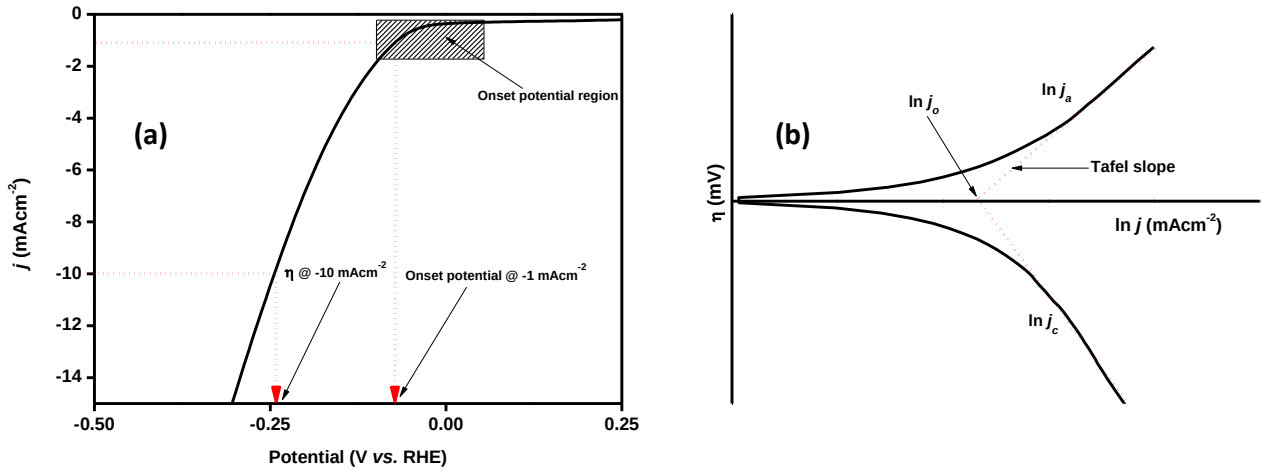

Figure 2.6: (a) Typical LSV polarization curve showing the onset and overpotential, and (b) Tafel plot showing the exchange current density.

2.6.2 Tafel Slope

The Tafel plot, given by the relationship between ln j and η is deduced from the Butler-Volmer equation. The Butler-Volmer equation, depicted in Eqn. 2.8, correlates the overall current density to the sum of the oxidation and reduction halves of the electrochemical process.

$$j = j_0 \left(e^{\frac{(1-\alpha F\eta)}{RT}} - e^{\frac{-\alpha F\eta}{RT}} \right) \quad \text{.....Eqn. 2.8}$$

where j is the current density, j_o is the exchange current density, F is the Faraday constant, η is the overpotential, R is the real gas constant, α is the transfer coefficient, and T is temperature.

Linearizing the Butler-Volmer equation using just the reduction half, gives

$$ln\, j = ln|\, j_0| - \frac{\alpha F}{RT}\eta \quad \text{.....Eqn. 2.9}$$

The slope and the y-intercept of a plot of ln j and η give the value of j_0 and the Tafel slope (linear region of the Tafel plot in Figure 2.6 (b)). Tafel slope indicates how readily an electrode material produces current as potential is applied. The smaller the Tafel slope is, the more readily current is produced from the electrode surface.[10]

2.6.3 Exchange Current Density

Extrapolation of the linear region of the Tafel plot gives a current that would be produced if no potential is applied, as shown in Figure 2.6 (b). This is the exchange current density, j_0, and is linked to the catalytic activity of the catalyst material. A highly catalytic electrode surface will have a relatively high j_0.

2.6.4 Charge Transfer Resistance

Charge transfer resistance (R_{ct}) is the resistance to electron transport at the electrode-electrolyte interface.[23] A Nyquist plot obtained from electrochemical impedance spectroscopy (EIS) provides information about the kinetics of the electron transport between catalytic sites and the electrolyte during HER.[24] A typical Nyquist plot is shown in Figure 2.7. The R_{ct} is deduced from fitting the EIS data to a cell circuit, insert of Figure 2.7, and corresponds to the diameter of the semi-circle. Parameters such as double-layer capacitance (C_{dl}), solution resistance (R_s), and R_{ct} are obtained from the fit. A smaller semi-circle diameter indicates fast charge transfer kinetics.[25]

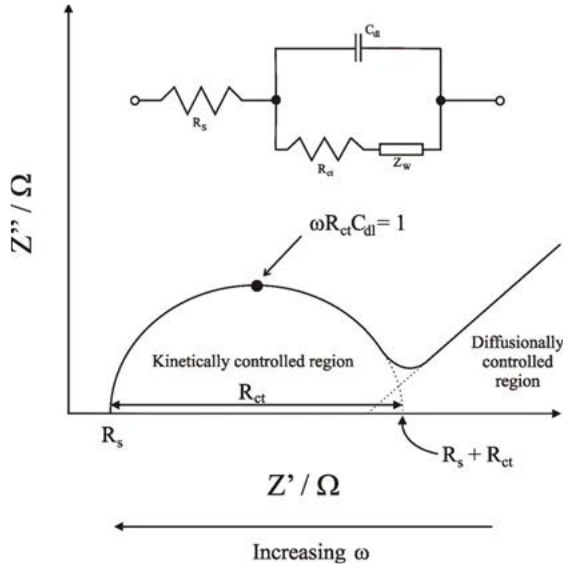

Figure 2.7: Typical Nyquist plot and insert is the corresponding electric equivalent circuit model.[26]

2.6.5 Turnover Frequency

Turnover frequency (TOF) is defined as the total number of H_2 molecules generated per active site of the catalyst per unit of time and is given by Eqn. 2.10.[27,28] As such, the catalyst that gives a high TOF is desirable.

$$TOF = \frac{jA}{2nF} \quad \text{.....Eqn. 2.10}$$

Where *j* is current density, A is the electrode surface area, n is the number of moles of active materials calculated using the electrochemical active surface area (ECSA) of the catalyst, F is Faraday constant (96 485.3 $Cmol^{-1}$) and 2 denotes the 2-electron HER process.

2.6.6 Faradaic Efficiency

Faradaic efficiency (FE) is the ratio of the amount of hydrogen generated during HER to the theoretical amount of hydrogen that can be obtained from the electrolysis reaction. As seen from

Eqn. 2.11, the closer to 1 or 100 % of the Faradaic efficiency percentage value is, the closer to the theoretical amount the hydrogen produced, and thus, the more ideal the catalyst is.

$$FE\ (\%) = \frac{Q1}{Q2} \times 100\ \% \quad \text{.....Eqn. 2.11}$$

Where Q1 is the amount of hydrogen evolved and Q2 is the amount of hydrogen at 100 % Faradaic efficiency.

2.7 Platinum Dichalcogenides

Platinum (Pt) is a noble transition metal deemed a successful HER electrocatalyst. Despite the impressive catalytic activity of Pt, industrialization of Pt-based electrolysers is restricted because of the high cost and scarcity of this material.[29] Materials composed of partial amounts of Pt that equate to the overall performance of pure platinum are attempted by structure manipulation, size control, and composition modification.[30] Pt nanomaterials conforming to different structural properties have been developed and applied in various electrochemical devices. Pt nanoparticles,[31] nanowires,[32] nanorods,[33] and nanotubes[34] are some of the Pt nanostructures that have been prepared and explored for application in various catalytic processes. Generally, nanoparticles have more surface area compared to their bulk counterparts, however, for catalytic reactions, the nanoparticle catalytic activity is not always directly proportional to increased surface area.[35] Size control and optimization are therefore a vital phenomenon in catalysis. Composition modification is achieved by alloying Pt with other transition metals such as nickel,[36] copper,[37] cobalt,[38] and palladium,[39] or the reaction of platinum with various ions, where Pt is oxidized to Pt^{2+} or Pt^{4+}. The latter include platinum phosphides, chalcogenides, oxides, and nitrides.

Platinum chalcogenides are natural minerals comprising sulfur, selenium, or tellurium. The platinum-to-chalcogen ratio may vary tremendously, resulting in the formation of various spinals ranging from binary, and pseudo-binary to ternary.[40] Binary platinum chalcogenide systems are formed in a wide range of atomic ratios. Platinum dichalcogenides (PtX_2, X= S, Se, or Te) are 2-dimensional (2D) transition metal materials. Generally, 2D transition metal dichalcogenides (TMDs) exist as covalently bonded chalcogen-metal-chalcogen layers, connected by weak interlayer van der Waals forces of attraction.[41] The weak interlayer forces can be broken down through an exfoliation process to reduce the number of layers in a specific material. This then results in materials that have properties far different from their bulk form. The few-layered 2D TMDs exhibit excellent electronic and optical properties and have thus found application in catalysis, optoelectronic devices, biosensing, and hydrogen production. These 2D TMDs also show

a layer-dependent band gap, transitioning from an indirect band gap in bulk TMDs to a direct band gap in few-layered structures.[42] Platinum dichalcogenides' properties deviate slightly from the general properties of 2D TMDs. Firstly, the traditional layer-dependent properties of TMDs are more dramatic in Pt dichalcogenides. This observation is best explained by bonding molecular orbital theory. The bonding Pt 5d orbitals energy and the bonding chalcogen p orbital energy levels get closer and closer together as the chalcogen is changed from sulfur to selenium to tellurium (Figure 2.8 (a)).[26] The energy levels of Pt d orbitals and Te p orbitals are almost at the same level (Figure 2.8 (b)). This then results in a much more pronounced hybridization degree between Pt d orbitals and chalcogen p orbitals, resulting in a more covalent bond nature between the two elements. The covalent nature of the Pt-chalcogen bond becomes more pronounced down the chalcogen group.[43] Secondly, the X-Pt-X interlayer interactions are covalent-like because of the extensive chalcogen p_z orbital hybridization, this interaction in turn, intensifies as the chalcogen changes from sulfur to selenium to tellurium.[44] This strays from the conventional van der Waals forces of attraction that exist between the X-M-X layers in most TMDs. These Pt dichalcogenide properties render them interesting for further exploration in catalysis.

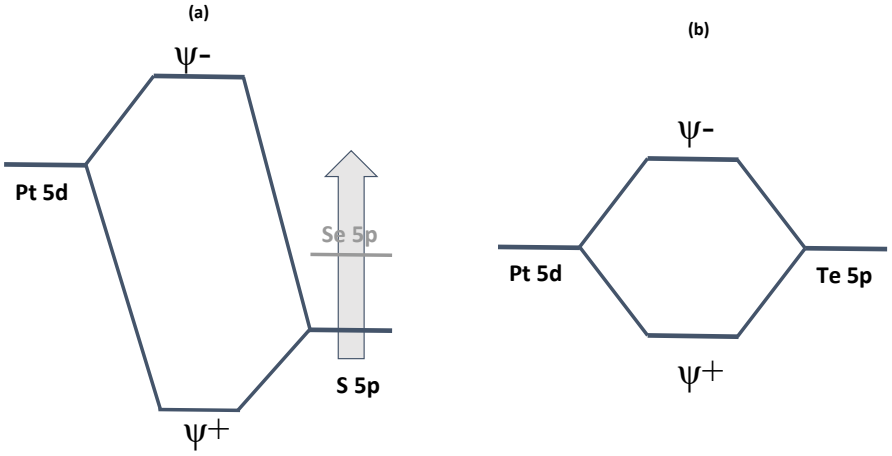

Figure 2.8: Schematic diagram showing the Pt d orbital and chalcogen p orbital interaction change as (a) chalcogen atom is changed from sulfur to selenium, and (b) tellurium.

2.8 Pt Dichalcogenides Crystal Structures

The arrangement of atoms in TMDs, particularly in TMDs with the general formula, MX_2 is similar. As such, MX_2 compounds have similar crystal structures, the hexagonal trigonal prismatic (2H) and tetragonal octahedral (IT) phases being the most common. The structures are shown in Figure 2.9. In both structures, the metal is coordinated to 6 chalcogen atoms, forming two triangular pyramids in the z and -z directions. The difference between the two crystal structures is the symmetry of the pyramids formed, demonstrated in the top view of the structures, of atom

arrangement. In the H-phase, the MX_2 is considered as 1 layer of the TMDs. On the other hand, the triangular pyramid in the -z direction in the 1T phase is rotated at 180 degrees thereby forming a hexagonal atom arrangement, as seen in the top view of the 1T phase.[41] The PtX_2 atom arrangement is reported to have the 1T crystal phase, where each Pt atom bonds to 6 chalcogen atoms in proportion.

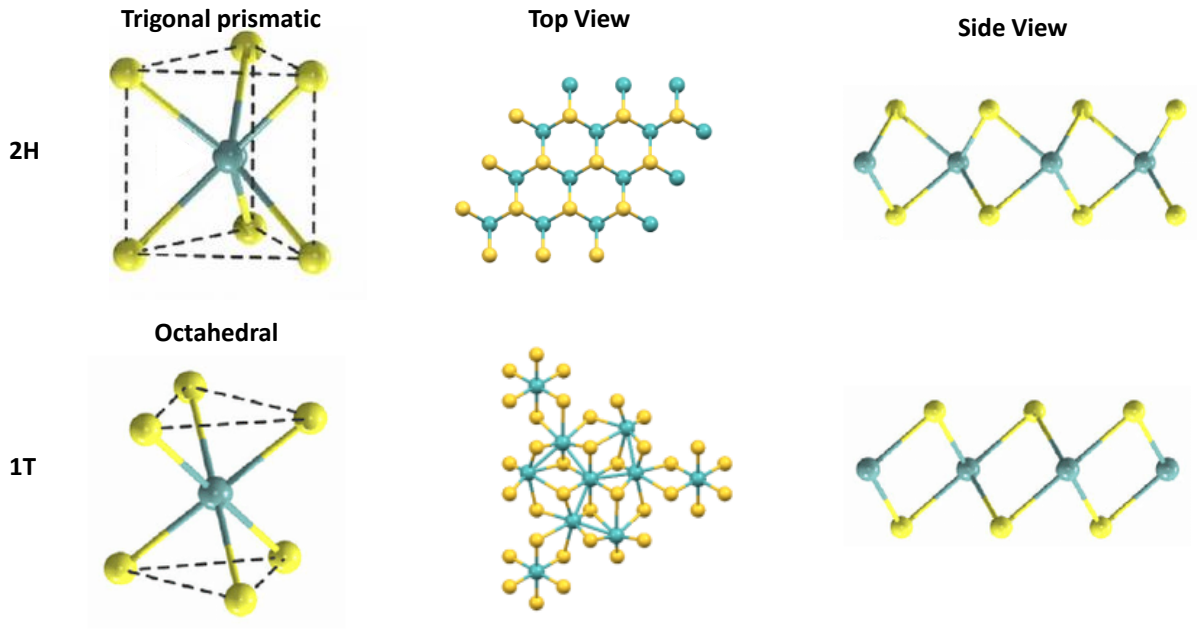

Figure 2.9: Atom arrangement of TMDs trigonal prismatic and (b) octahedral and the corresponding top and side views.

2.9 Synthesis of Platinum Dichalcogenides

The synthesis procedure of TMDs influences the morphology and ultimately the HER activity of the catalysts. Table 2.1 compares the HER performance of platinum group metal (PGM) dichalcogenides prepared by thermally assisted, colloidal, and hydrothermal synthesis methods. This table highlights the notion that the synthesis method chosen for a particular material is crucial and influences the catalytic activity of the compounds. The preparation of 2D TMDs is classified as either top-down or bottom-up. The top-down synthesis procedure involves breaking down the weak van der Waals interlayer interactions in TMDs by ultrasonication of naturally occurring layered TMDs, such as WS_2 and MoS_2.[45] In the bottom-up approach, the layered TMD structures are constructed on a substrate material using specific elemental precursors. The chemical vapor deposition (CVD) method, mechanical exfoliation (ME), and thermally assisted conversion (TAC) are some of the synthesis methods reported for the preparation of Pt dichalcogenides.

Table 2.1: Comparison of the HER performance (Overpotential) of PGM chalcogenides acquired in 1M KOH electrolyte.

Catalyst	Synthesis Procedure	Morphology	Overpotential @-10mAcm^{-2}/mV	Ref
PtS_2	TAC	Nanocluster	95	[46]
$PtSe_2$	TAC	Cauliflower	94	[46]
$PtTe_2$	TAC	Nanostrips	92	[46]
$RuSe_2$	Hydrothermal	Amorphous	27	[47]
PdS	Colloidal	Nanosheets	49	[48]
Rh_3Se_4	TAC	Quasi-spherical	92	[49]

2.9.1 Thermally Assisted Conversion

Thermally assisted conversion (TAC) for Pt dichalcogenide preparation is a twofold process; magnetron sputtering followed by CVD. In the magnetron sputtering, Pt film is prepared by sputtering Pt onto a substrate using a radiofrequency (RF) magnetron sputtering process, depicted in Figure 2.10 (a), and the layer thickness is monitored and controlled by the sputtering duration. The Pt film is then placed in a CVD quartz tube subjected to two different temperature heating zones (Figure 2.10 (b)). Usually, the chalcogen is placed at a relatively low temperature (~200 °C) while the preprepared Pt film is placed at a higher temperature zone (~500-600 °C). The carrier gas transports the vapourised chalcogen source to the Pt film, where PtX_2 is grown.[50] The size and morphology of the resulting nanomaterials can be controlled by tuning the temperature of the furnace, the type of precursors, and the reaction time. This procedure allows the possibility of TMD doping and TMD heterostructure formation. Single and poly-crystalline $PtSe_2$ films,[51–54] $MoS_2/PtSe_2$ heterostructure,[55] PtS_2, and $PtTe_2$[56] have been previously synthesized via this procedure.

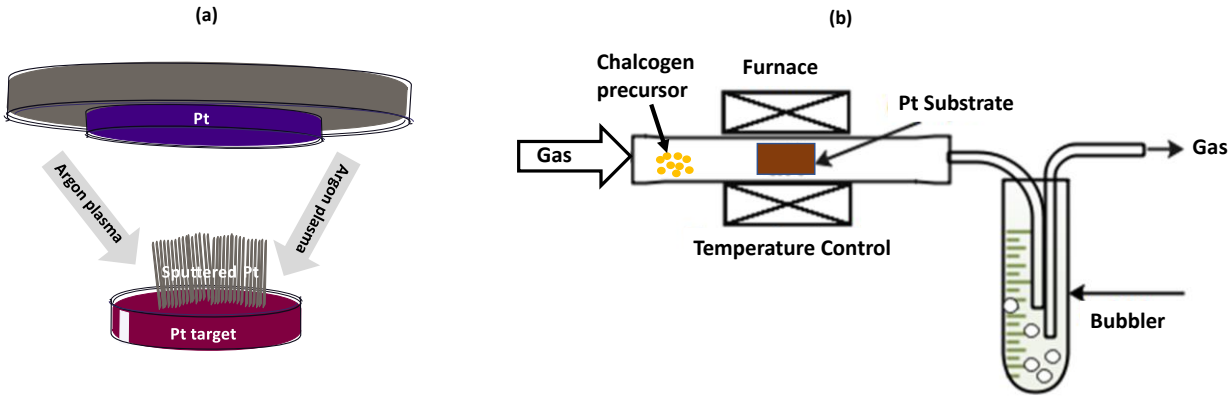

Figure 2.10: (a) Radiofrequency sputtering of Pt on a substrate,[29] and (b) CVD set-up for PtX_2 preparation.

2.9.2 Mechanical Exfoliation

For materials that do not occur in nature as layered structures, their bulk structures are first grown by the chemical vapor transport (CVT) method. After that, the single layer or a few layered materials are produced by either mechanical or chemical exfoliation. For mechanical exfoliation (ME), a scotch tape is fixed onto the bulk crystal and peeled off to produce a few layered PtX_2 material,[57] as demonstrated in Figure 2.11. The limitations of ME include low product yields. Few layered $PtSe_2$ flakes have been prepared through this procedure[58].

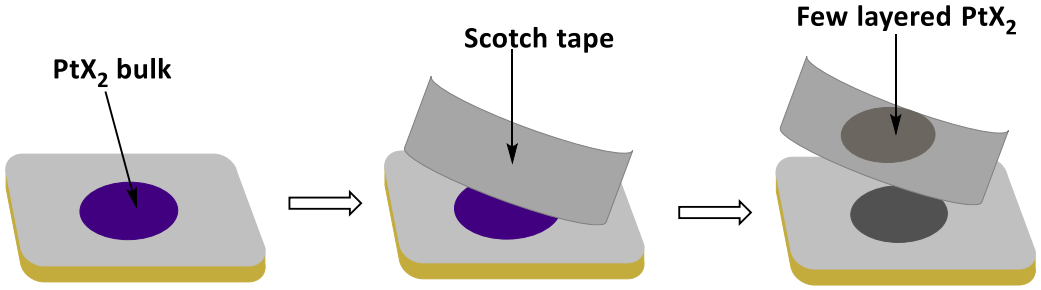

Figure 2.11: Mechanical exfoliation of bulk PtX_2 using scotch tape approach to produce a few layered PtX_2.

2.9.3 Molecular Beam Epitaxy

Molecular beam epitaxy (MBE) is another method employed for the preparation of TMDs thin films. It mimics "spray painting" and involves the subjection of a beam of target atoms or molecules in a high vacuum environment to a hot crystal surface.[59] The high vacuum environment offers excellent control over the purity of the material components and layer thickness. The composition in each layer can be altered by turning off the beam and switching to another beam source. MBE of Pt dichalcogenides is demonstrated in Figure 2.12.

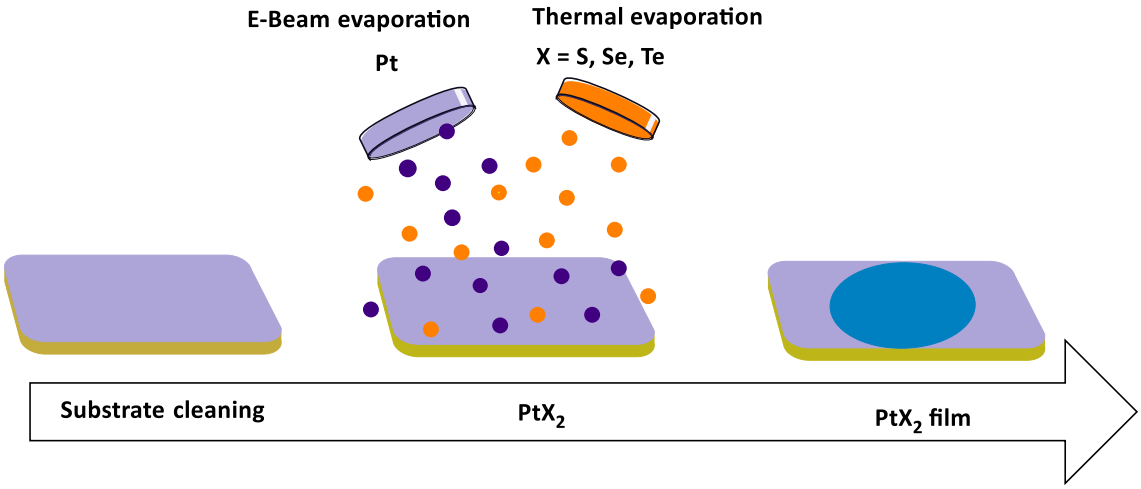

Figure 2.12: Schematic diagram showing steps in the MBE preparation of PtX_2.

2.9.4 Hydrothermal Synthesis

Hydrothermal synthesis is a solution-based low-temperature, high-pressure synthesis method traditionally employed for large-scale synthesis of TMDs. The schematic for the steps taken in this procedure is demonstrated in Figure 2.13. The respective transition metal precursor and the chalcogen precursor are dissolved in a solvent by stirring, and the mixture is transferred to a sealed autoclave vessel and then subjected to high temperature and pressure for a specific time. The nanoparticles formed are usually insoluble in the solvent and can be isolated by filtration or centrifugation. Although this method is popular for other TMDs such as $MoSe_2$, MoS_2, $NiSe_2$, WSe_2, etc, it has not been explored for Pt dichalcogenides.[60–64] The only solution-based synthesis reported for Pt dichalcogenides is the preparation of $PtSe_2$ in water through Pt-Se complex assembly on a surfactant followed by thermal annealing to produce $PtSe_2$.[65] The advantage of using solution processes to prepare TMDs is the ease of scaling up and post-synthesis processing of the materials.

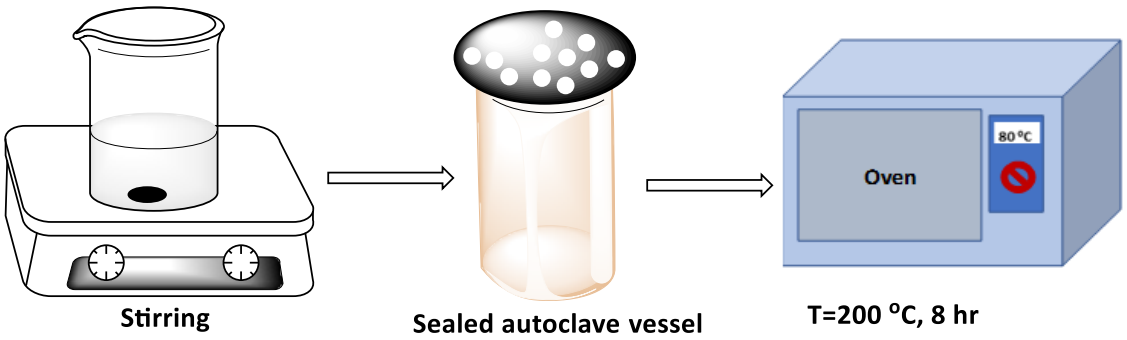

Figure 2.13: Hydrothermal synthesis procedure.

2.9.5 Colloidal Synthesis of TMDs

Metal chalcogenides, metals, metal oxides, and metal phosphines have been prepared by the colloidal synthesis method. The major advantage of employing colloidal synthesis for nanomaterial preparation is the ability to control the size, composition, and morphology of the nanoparticles by manipulating the reaction parameters.[66–68] Reaction parameters that can be manipulated and optimized in colloidal synthesis include the surfactant, precursor concentration and ratio, temperature, and reaction time.[69,70] Additionally, the nanoparticles prepared using this procedure allow for post-synthesis processing appropriate ink formation of the nanoparticles, and suitable ink deposition on the substrate by a suitable, specific technique. Surfactant/capping ligand, solvent, and target material precursors are the three major components of colloidal synthesis, although most often the organic surfactant also serves as a solvent. The choice of surfactant in colloidal synthesis is vital. The nanoparticles' formation mechanism follows a 3-step process, nucleation, growth, and growth termination. The first two steps are explained by the LaMer model shown in Figure 2.14 (a). The first step is the formation of monomers from the precursors and the increase in monomer concentration until supersaturation is reached, C_m, followed by nuclei formation through aggregation and self-nucleation of monomers as the concentration of the monomers escalates and approaches supersaturation, then ultimately the growth and generation of nanocrystals as monomers and nuclei interact. This process continues until such time that the monomer concentration declines below the critical level.[71]

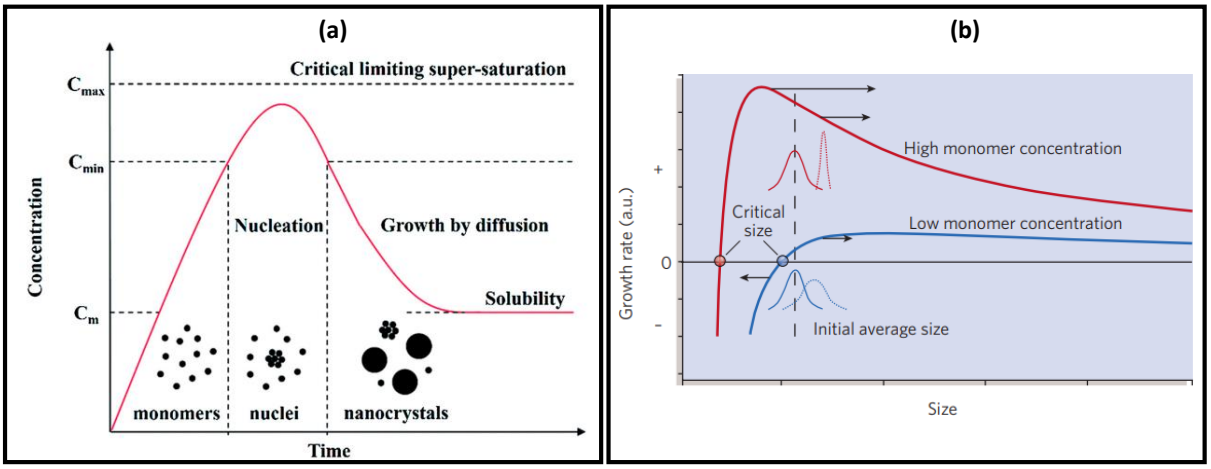

Figure 2.14: (a) LaMer diagram demonstrating the concentration change with nucleation and growth profile of nanoparticles.[71] and (b) effect of monomer concentration on size-distribution of the nanoparticles.[69]

The challenge often faced with the colloidal synthesis process is controlling the size distribution of the resulting nanoparticles. The concentration of the monomer plays a key part in the size of the

nanoparticles, as explained in Figure 2.14 (b). It reveals that if monomer concentration is below the critical threshold, the size distribution broadens as small particles are depleted at the cost of large particle growth. Alternatively, small particles grow faster than large particles at high monomer concentrations. This process produces particles with a narrow size distribution.[69] Generally, this follows the assumption that elevated monomer concentration generates a swift growth of small crystals rather than large crystals.[72]

Rather than allowing nucleation and growth to occur simultaneously, nucleation and growth steps can be disjoined to reduce the nanoparticle size distribution. Injection of precursors into the hot solvent, referred to as burst nucleation, shadowed by solution temperature reduction, helps isolate the two processes. This is the colloidal hot injection process and is shown in Figure 2.15. In a typical hot injection synthesis procedure, the surfactant solution is heated to a high temperature, then the precursors are injected. During the reaction process, the surfactant influences the size of the nanoparticles formed by interacting with the nuclei surface and therefore hindering nuclei agglomeration and haphazard growth.[73,74] Additionally, the surfactant can interact with a specific surface site of the nanoparticles, thereby influencing the shape of the nanoparticle.[75]

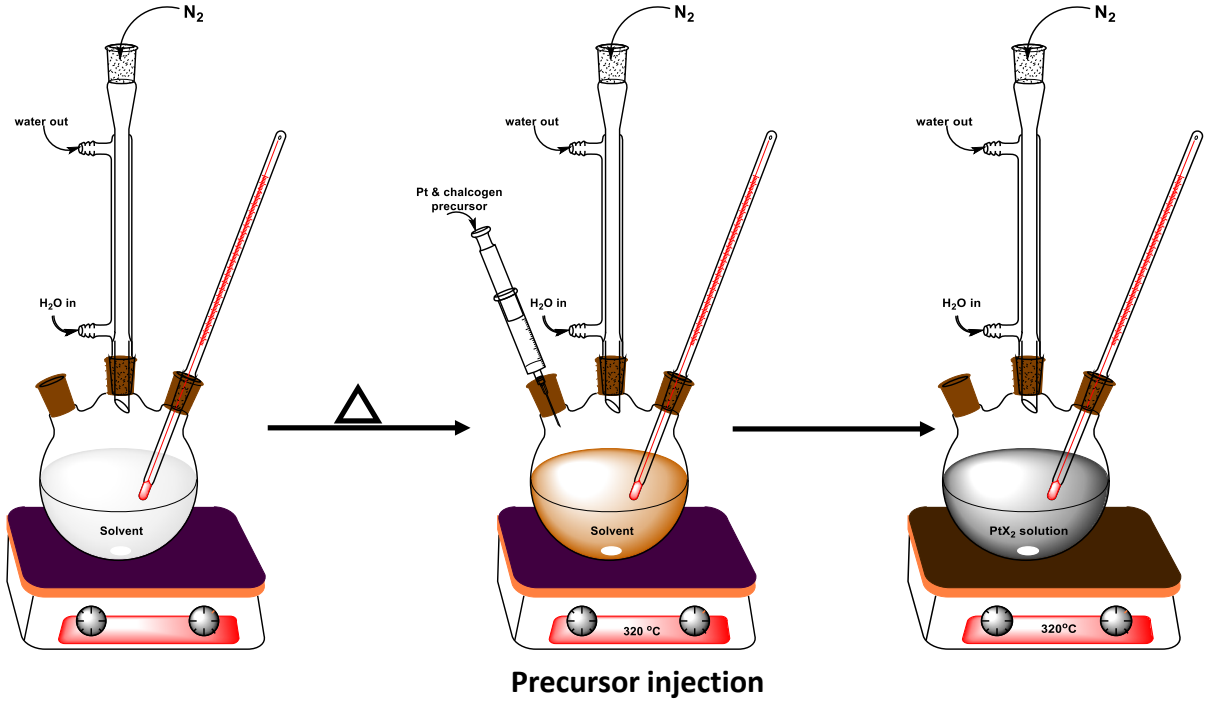

Figure 2.15: Hot-injection colloidal synthesis set-up of PtX_2.

2.10 Introduction to Photo-electrochemical HER

The key components of a PEC cell are the anode, membrane, electrolyte, and cathode. The light can either be irradiated directly at the photoanode or photocathode, resulting in two possible cell

configurations with one photoanode. In Figure 2.16 (a), the anode is exposed to the light source, and the cathode is constructed from a metallic material. In the second configuration (Figure 2.16 (b)), however, light is shone directly onto the cathode while the metal surface is used for the anode.[76] These PEC configurations are referred to as single photoelectrode cell designs and pose a few drawbacks, one of which is finding a semiconductor (SC) material that has a band edge in line with the potential required to split water. Often, additional energy injection may be required to accomplish complete water reduction and oxidation. Alternatively, several other PEC cell designs are developed where both the anode and the cathode are photoelectrodes, or where the water-splitting device is coupled with a photovoltaic cell that provides the energy required for the H_2 and O_2 half-cell reaction.[77,78]

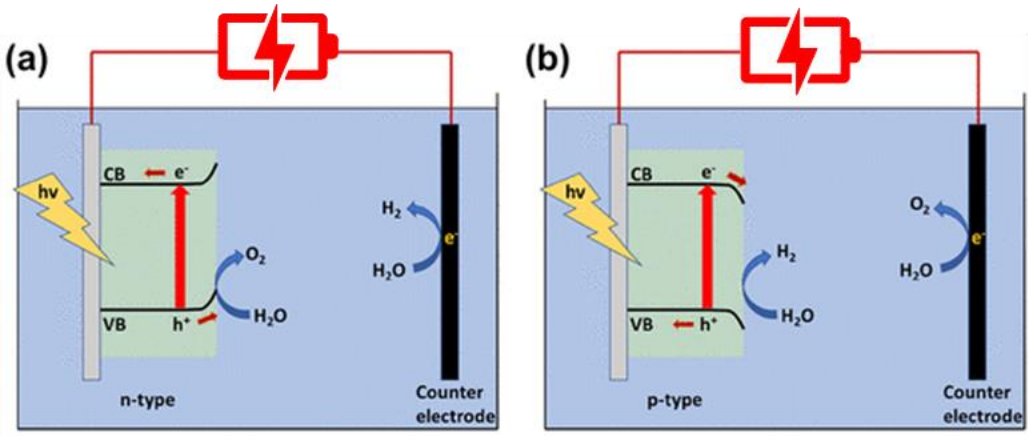

Figure 2.16: The PEC cell architecture with at least one photoelectrode.

The construction of a PEC includes a photoelectrode (anode), usually a narrow bandgap semiconductor, and a cathode electrode immersed in an aqueous electrolyte. The mechanism by which O_2 and H_2 are produced in PEC devices is shown in Figure 2.17. Firstly, light is shone onto a semiconductor thin film anode material. The semiconductor absorbs the light, and the light energy greater than the semiconductor bandgap will cause the excitation of electrons to the conduction band (CB). The excited electrons leave behind positively charged holes (h^+) in the semiconductor valence band (VB). The generated electrons and holes can either recombine or separate. Recombination means that the excited electrons lose energy before they are carried away through the external circuit, and they return to the semiconductor VB where they recombine with the holes. The PEC process is largely obstructed by the electron-hole pair recombination. Otherwise, the excited electrons travel through the external circuit and are harnessed by the counter electrode, where the H^+ ions are reduced to H_2. The h^+ travel to the semiconductor-electrolyte interface, where they facilitate the oxidation of H_2O molecules to O_2.[79] Solar-driven water splitting is an endergonic process accompanied by a Gibbs free energy change of 238 $kJmol^{-1}$,

corresponding to an applied voltage of 1.23 V. According to the energy equation of a photon (Eqn. 2.12), the change in Gibbs free energy of 238 $kJmol^{-1}$ corresponds to a photon with 1000 nm wavelength, or lower. Therefore, the photon wavelength should be lower than 1000 nm to initiate the PEC water splitting. The semiconductor material engineering to achieve the maximum PEC efficiency (η_{PEC}) is achieved by narrowing the bandgap. Bandgap modification can be achieved by doping, shape and size control, surface activation, and cocatalyst development. The implementation of PEC water-splitting devices for H_2 production is restricted by poor overall efficiency brought about by several factors. The recombination of the electron-hole pair, high overpotential, and slow reaction kinetics are highlighted as three root causes of the PEC device's poor efficiency.[80] Consequently, the development of catalysts that address either or all these hindrances is crucial. In this study, $PtSe_2$/N-MWCNTs composites will be evaluated as a PEC photocathode HER catalyst. Both $PtSe_2$ and N-MWCNTs are HER-active materials, and the incorporation of N-MWCNTs is aimed at improving the electron transport properties and surface area of $PtSe_2$, thereby reducing the electron-hole recombination probability.

$$\boldsymbol{E\ (eV) = hf = \frac{hc\ (eV.nm)}{\lambda\ (nm)} = \frac{1240\ eV.nm}{\lambda\ (nm)}} \quad \textbf{.....Eqn. 2.12}$$

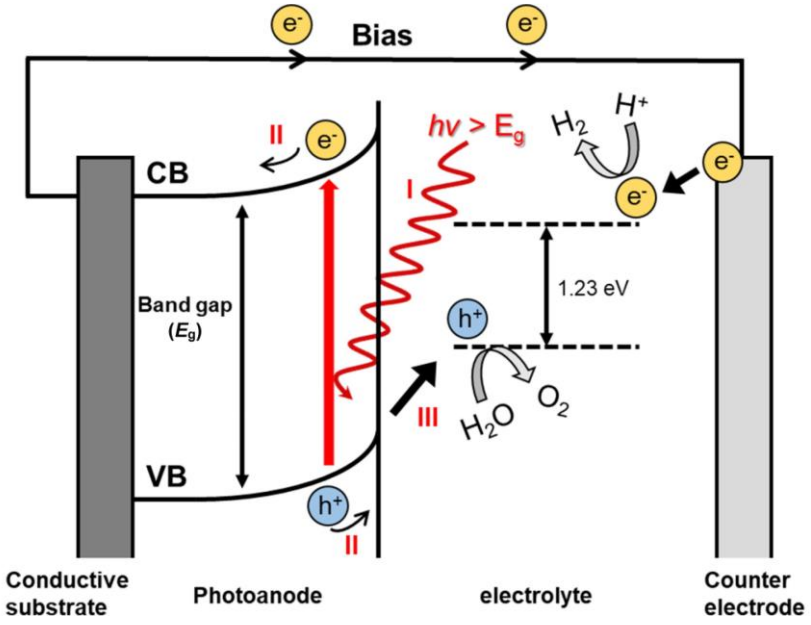

Figure 2.17: PEC water splitting mechanism highlighting (i) semiconductor photo absorption, (ii) charge carrier generation, separation, and migration, and (iii) O_2 and H_2 generation.[81]

2.11 PEC Photoelectrodes

Semiconductors play a crucial role in the PEC water system and should possess the following qualities: wide solar absorption spectrum, stable and corrosion-free in the electrolyte, high-quality,

and compatible band gap to the water splitting process. As shown in Figure 2.16, light can either be directed at the anode or the cathode, and in both cases, the light-harnessing ability of the semiconductor is reliant on its optical properties.[82] Vast research on the use of silicon in PEC was initiated by Candea R. et al. in 1976 who reported, for the first time, the employment of Si in light-driven water electrolysis.[83] Although they concluded that Si is not a good HER catalyst because other reactions dominate near equilibrium, they discovered that the HER catalytic activity of silicon improves when illuminated with light. Their discovery led to intensive research on the manipulation of Si band gap, crystal structures, and morphology and their application as photoelectrodes in light-driven devices. In addition to being HER catalysts, TMDs, particularly monolayer 2D TMDs are studied and found as suitable PEC photocatalysts. Unlike their bulk counterparts which have an indirect band gap, monolayer 2D TMDs have a direct band gap, approximately 2 eV and thus have better optical absorption properties. Also, the VB and CB of monolayer TMDS, such as MoS_2 are compatible with the water splitting process and therefore qualify to be photoelectrodes in PEC water splitting.[84,85] Generally, several approaches are undertaken to improve the semiconductor properties to improve the overall PEC performance and these strategies include band-gap manipulation, cocatalysts formation, doping, and heterostructure development.

2.12 Photoelectrode Performance Improvement

2.12.1 Band-gap Engineering and Doping

Semiconductor (SC) materials have the energy zone between the valence band (VB) and conduction band (CB) which corresponds to the energy required to excite electrons from the VB to the CB and is referred to as the band gap (Figure 2.18 (i)). Band gap influences the optical and electronic properties of different SCs, and the magnitude differs from material to material. The larger the band gap energy is, the poorer the solar absorption spectrum of the SC is. Modification of the band gap through processes such as material composition, doping, and inducing strain is referred to as band gap engineering. Doping to the SC nanomaterial results in the formation of local states with relatively lower energy differences, and these act as prevalent excitation and relaxation optical stations, thereby widening the absorption spectrum of the material (Figure 2.18 (ii)).[86,87] Otherwise, the solar absorption can be widened by shifting the VB to a higher energy level and the CB to a lower energy level, giving way to a smaller band gap energy, as shown in Figure 2.18 (iii).[86]

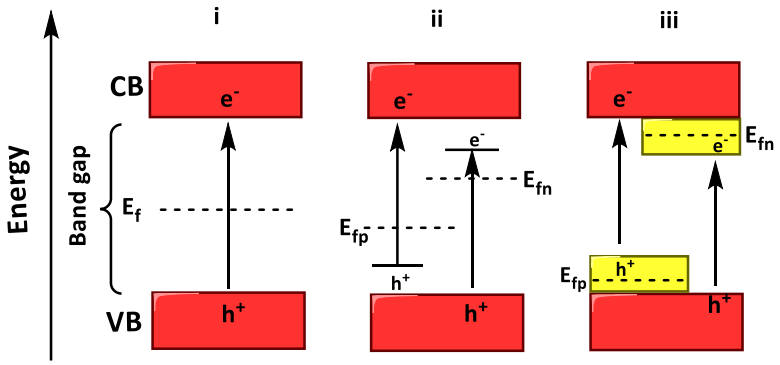

Figure 2.18: (i) A typical direct band gap structure of a semiconductor and the development of local states (ii) and (iii) the shift in VB and CB on the semiconductor due to doping.

2.12.2 Cocatalyts Development

A photoanode constructed from a single SC does not generate enough current and therefore results in a low PEC conversion efficiency. Marrying the single SC material with a photocatalyst improves the charge separation ability of the photoanode, catalyzes surface reaction (oxidation/ reduction), reduce surface oxidation, and therefore hinders photo corrosion of the SC photoanode.[88,89] Noble metals such as Pt have been employed as cocatalysts for silicon electrodes. In the quest to improve the commercialization possibility of various devices, the high-cost noble metal cocatalysts are replaced by earth-abundant TMDs cocatalysts. As an example, Patel M et al developed an n-type WS_2/p-Si photocathode which reduced the overpotential at -10 $mVcm^{-2}$ by a magnitude of 4 from 0.8 V to 0.2 V for bare Si photocathode[90]. This observation initiates further exploration of 2D TMDs for application in PEC photoelectrode application. Molybdenum,[91,92] cobalt,[93] and nickel[94,95] compounds have also been investigated as cocatalysts in PEC photoelectrodes.

2.12.3 Semiconductor Heterostructure Development

A heterostructure is a material constructed from two or more SCs with different band edges and gaps. For a single SC, excited electrons migrate from the conduction band (CB) to the cathode and take part in the reduction reaction, whereas the h^+ from the valence band (VB) participates in the oxidation reaction (Figure 2.19 (a)). The combination of two SCs where the CB of one SC (SC1) lies higher in energy than the CB of the second SC (SC2) is shown in Figure 2.19 (b). An interface is created where an internal electric field emerges and promotes the charge separation of excited electrons and positively charged holes. Electrons migrate from CB1 to CB2 while h^+ migrates from VB2 to VB1. This process yields a higher efficiency e^--h^+ separation and water oxidation and reduction process.[96,97] Typically, TMDs exhibit an n-type or a p-type behaviour which then offers the opportunity to fabricate p-n heterojunction structures purely from TMDs.

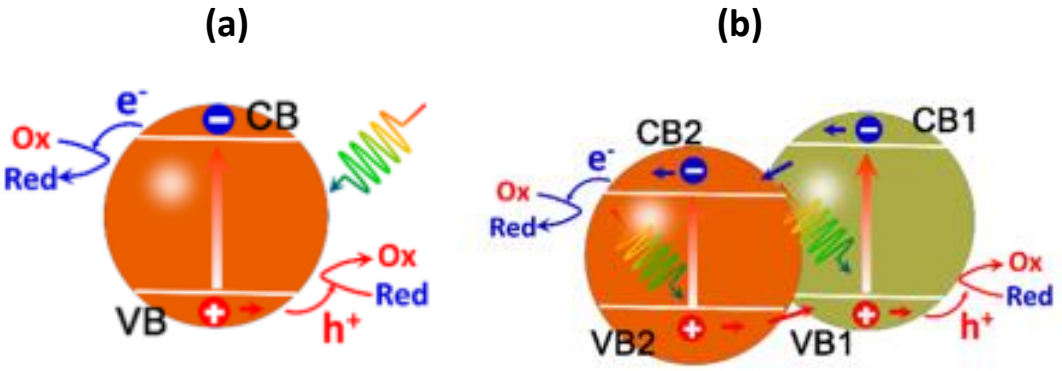

Figure 2.19: Creation and e^- /h^+ pair transfer across various semiconductor heterojunctions.

2.13 PEC Photocathode Performance Indicators

The photocathode performance merits under illumination can be determined by a three-electrode cell like the electrocatalytic HER evaluation of a catalyst. The performance parameters detailed in Section 2.6 such as onset potential, overpotential at -10 $mAcm^{-2}$, Tafel slope, and charge transfer resistance are used to gauge the photocathode activity under light.[98,99] In addition, the incident photon to current efficiency (IPCE) is used to compare different catalysts' light-induced HER performance. IPCE gives an indication of electrons or current generated per photons injected into the PEC device, it is the efficiency of hydrogen production through water reduction to the incident radiation (Eqn. 2.13).[93]

$$IPCE = \frac{1240 \times J\ (mAcm^{-2})}{\lambda\ (nm) \times P\ (mWcm^{-2})} \times 100\ \% \quad \text{.....Eqn. 2.13}$$

Where J is the photocurrent density at a specific wavelength, P is the optical power efficiency and λ is the incident light wavelength.[73]

2.14 Carbon-supported TMDs

The PEC efficiency of various SCs can be improved by hybridizing the SC with carbon materials. The hybridization with carbon compounds improves the SC stability, the photo absorption, and limits charge carrier recombination. Carbon nanotubes, activated carbon, graphene, graphitic carbonitride and graphene oxide are carbon allotropes that have been investigated for this role by various authors.[100] Carbon nanotubes are reported to exhibit high electron conductivity, high surface area, good chemical, and thermal stability[101]. Carbon nanotube-semiconductor composites evaluated for PEC water splitting include MWCNTs-modified ZnO,[102] MWCNTs/WO_3,[103] and MWCNT-modified Fe_2O_3.[104] It is imperative to control the amount of carbon nanotubes in the composite materials. Low % loading of CNTs has been shown to improve the PEC efficiency, whereas high loadings lead to ultrafast electron mobilities leading to SC active site blockage and

initiated charge recombination. Not much research has been channelled towards exploring TMDs/MWCNTs hybrid systems for application in PEC device photoanodes. This study explores the use of 2D PtX_2 supported on N-MWCNTs as photocathode in light-driven hydrogen evolution reaction.

2.15 Preparation of TMDs supported on MWCNTs

2.15.1 Hydrothermal Synthesis

Hydrothermal synthesis is an aqueous-based crystal synthesis method carried out in a closed vessel heated to high temperature and pressure.[105] The precursors are dissolved in water and placed in a Teflon cup. For TMDs/NMWCNTs, the process involves the dissolution of prepared acid-treated MWCNTs by CVD in water and sonicating or stirring the solution for a few hours. This step is aimed at reducing carbon nanotube agglomeration. The TMD precursor is then added to the nanotube solution, and sometimes a reducing agent, transferred to an autoclave and heated to high temperature (usually 150℃ - 200°C) for several hours, typically 6-24 hours. MoS_2/MWCNTs, WS_2/MWCNTs, and Ni_2/MWCNTs composites are some of the transition dichalcogenides grown on the nanotubes.[106–108] Figure 2.20 (a) and (b) show the TEM images of MoS_2/MWCNTs and Ni2/MWCNTs prepared by hydrothermal synthesis. The chalcogen and the metal precursors, reaction time, and reaction temperature influence the morphology and dispersion of the TMDs on the nanotubes. Additionally, the functional groups induced by acid treatment on the nanotube walls are attributed to the interaction of the nanotubes and the metal chalcogenides. They act as nucleation sites for the formation and growth of the metal chalcogenide.

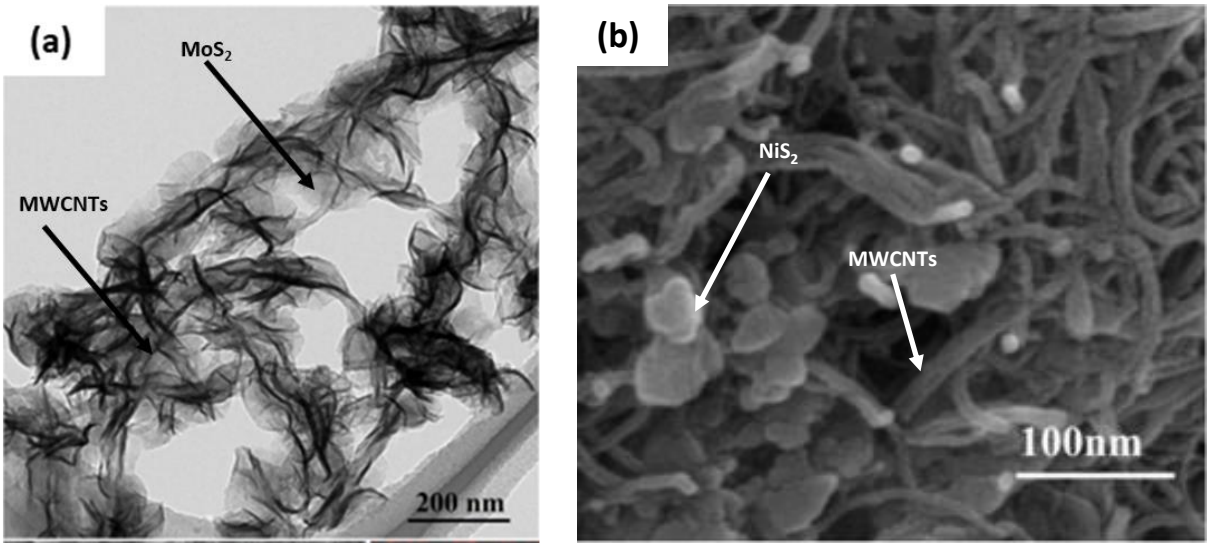

Figure 2.20: (a) MoS_2/MWCNTs,[109] and (b) NiS_2/MWCNTs[110] prepared by hydrothermal synthesis method.

2.15.2 Ultrasonication

Alternatively, MWCNTs and transition metal chalcogenides can be separately prepared, and their hybrids prepared through simple procedures such as stirring and sonication. The treatment time and stirring rate/sonication power play a crucial role in the dispersion and interaction of the individual composite components. This process offers full control of the size, morphology, and transition metal chalcogenide concentration in the target composite materials. Thereafter, surface interaction between the transition metal chalcogenide and nanotubes is initiated by high-power sonication or by stirring for plonged periods in the presence of a solvent.[111–113] In our previous study, we demonstrated that an interaction can be developed between Cu_2ZnSnS_4, and nitrogen-doped multi-walled carbon nanotubes by sonicating the two materials in dimethylformamide (Figure 2.21).[113]

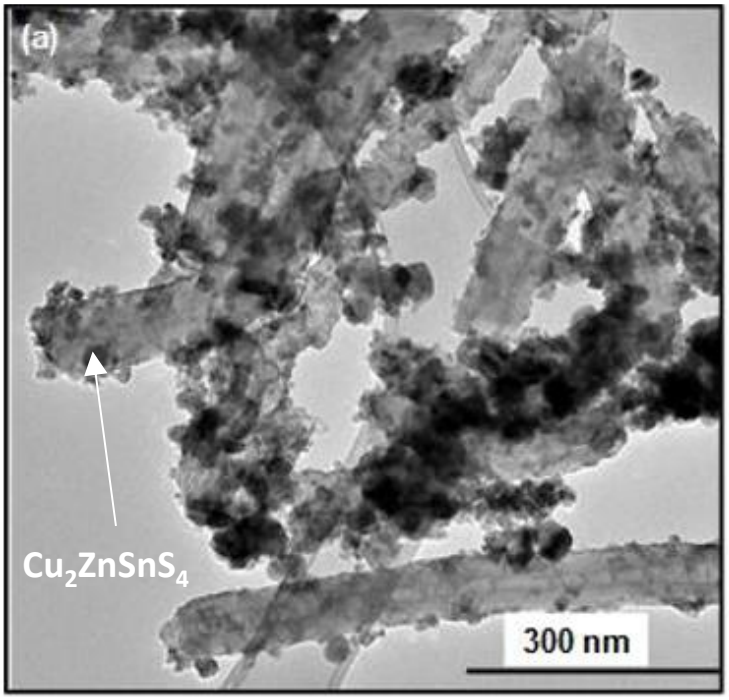

Figure 2.21: TEM image of Cu_2ZnSnS_4/N-MWCNTs hybrid prepared by sonication.[101]

The research and development of efficient HER electrocatalysts is an ongoing hunt, a hunt fuelled by the urgent need to supplement and ultimately replace fossil fuel combustion for energy. Transition metal dichalcogenides research in electrochemical reactions is a hot area of research that is driven by the ease of fabrication of these materials, their high surface area, exposed catalytic sites, and the ability to manipulate their electrochemical properties through atom intercalation, doping, morphology, and hybridization with other materials.

2.16 References

1. Abe, J. O. et al. Hydrogen energy, economy, and storage: Review and recommendation. *Int J Hydrog Energy* 44, 15072 - 15086 (2019).

2. Safari, F. & Dincer, I. A review and comparative evaluation of thermochemical water splitting cycles for hydrogen production. *Energy Convers Manag* 205, 112182 (2020).

3. Becherif, M. et al. Hydrogen energy storage: New techno-economic emergence solution analysis. *Energy Procedia* 74, 371 - 380 (2015).

4. Cau, G. et al. Energy management strategy based on short-term generation scheduling for a renewable microgrid using a hydrogen storage system. *Energy Convers Manag* 87, 820 - 831 (2014)

5. Jovan, D. J. & Dolanc, G. Can green hydrogen production be economically viable under current market conditions. *Energies* 13, 6599 (2020)

6. Shiva K. S. & Lim, H. An overview of water electrolysis technologies for green hydrogen production. *Energy Reports* 8, 13793 - 13813 (2022).

7. You, B. & Sun, Y. Innovative strategies for electrocatalytic water splitting. *Acc Chem Res* 51, 1571 - 1580 (2018).

8. Sun, L., Luo, Q., Dai, Z. & Ma, F. Material libraries for electrocatalytic overall water splitting. *Coord Chem Rev* 444, 214049 (2021).

9. Kumar, S., Kaur, R. & Sharma, S. Recent reports on hydrogen evolution reactions and catalysis. *Results Chem* 4, 100613 (2022).

10. Gebremariam, G. K., Jovanović, A. Z. & Pašti, I. A. The effect of electrolytes on the kinetics of the hydrogen evolution reaction. *Hydrog* 4, 776 - 806 (2023).

11. Kumar, M. et al. Recent trends in photoelectrochemical water splitting: the role of cocatalysts. *NPG Asia Mater* 14, 88 (2022).

12. Chen, Z. et al. Accelerating materials development for photoelectrochemical hydrogen production: Standards for methods, definitions, and reporting protocols. *J Mater Res* 25, 3 - 16 (2010).

13. Lin, Y. *et al.* Semiconductor nanostructure-based photoelectrochemical water splitting: A brief review. *Chem Phys Lett* 507, 209 - 215 (2011).

14. El ouardi, M. *et al.* Review of photoelectrochemical water splitting: From quantitative approaches to effect of sacrificial agents, oxygen vacancies, thermal and magnetic field on (photo)electrolysis. *Int J Hydrog Energy* 51, 1044 - 1067 (2024).

15. https://www.titech.ac.jp/english/news/2019/045462 accessed on 17th of March 2024.

16. Zhu, Y. *et al.* Facilitating alkaline hydrogen evolution reaction on the hetero-interfaced Ru/RuO_2 through Pt single atoms doping. *Nat Commun* 15, 1447 (2024).
17. Cheng, F. *et al.* Accelerated water activation and stabilized metal-organic framework via constructing triangular active-regions for ampere-level current density hydrogen production. *Nat Commun* 13, 6486 (2022).
18. Morales-Guio, C. G., Stern, L. A. & Hu, X. Nanostructured hydrotreating catalysts for electrochemical hydrogen evolution. *Chem Soc Rev* 43, 6555 - 6569 (2014).
19. Zhu, J. et al. Recent advances in electrocatalytic hydrogen evolution using nanoparticles. *Chem Rev* 120, 851 - 918 (2020).
20. Mahmood, N. et al. Electrocatalysts for hydrogen evolution in alkaline electrolytes: Mechanisms, challenges, and prospective solutions. *Adv Sci* 5, 1700464 (2018).
21. Quaino, P. et al. Volcano plots in hydrogen electrocatalysis-uses and abuses. *Beilstein J Nanotechnol* 5, 846 - 854 (2014).
22. Trasatti, S. Work function, electronegativity, and electrochemical behavior of metals: III. Electrolytic hydrogen evolution in acid solutions. *J Electroanal Chem Interfacial Electrochem* 39, 163 - 184 (1972).
23. Tan, Z. H. et al. Recent advances in defect-engineered transition metal dichalcogenides for enhanced electrocatalytic hydrogen evolution: Perfecting imperfections. *ACS Omega* 8, 1851 - 1863 (2022)
24. Li, H. et al. S-doping induced phase engineering of $MoSe_2$ for hydrogen evolution reaction. *Int J Hydrog Energy* 47, 30371 - 30377 (2022).
25. Suliman, M. H. et al. Facile synthesis of ultrathin interconnected carbon nanosheets as a robust support for small and uniformly dispersed iron phosphide for the hydrogen evolution reaction. *Carbon* 144, 764 - 771 (2019).
26. Dai, D. et al. Trends in the structure and bonding in the layered platinum dioxide and dichalcogenides PtQ_2 (Q = O, S, Se, Te). *J Solid State Chem* 173, 114 - 121 (2003).
27. Boudart, M. Turnover rates in heterogeneous catalysis. *Chem. Rev* 95, 661 - 666 (1995).
28. Feng, W. et al. Transition metal selenides for electrocatalytic hydrogen evolution reaction. *ChemElectroChem* 7, 31 - 54 (2020).
29. Hussain, S. et al. Experimental and theoretical insights to demonstrate the hydrogen evolution activity of layered platinum dichalcogenides electrocatalysts. *J Mater* 12, 385 - 398 (2021).
30. Rohaizad, N. et al. Layered platinum dichalcogenides (PtS_2, $PtSe_2$, $PtTe_2$) for non-enzymatic electrochemical sensor. *Appl Mater Today* 19, 100606 (2020).

31. Ahmadi, T. S. et al. Shape-controlled synthesis of colloidal platinum nanoparticles. *Sci* 272, 1924 - 1926 (1996).

32. Chen, J. et al. Single-crystal nanowires of platinum can be synthesized by controlling the reaction rate of a polyol process. *J Am Chem Soc* 126, 10854 - 10855 (2004).

33. Bu, L. et al. Highly distorted platinum nanorods for high-efficiency fuel cell catalysis. *CCS Chem*, 2, 401 - 412 (2020).

34. Zhang, G. et al. Porous dendritic platinum nanotubes with extremely high activity and stability for oxygen reduction reaction. *Sci Rep* 3, 1526 (2013).

35. Isaifan, R. J., Ntais, S. & Baranova, E. A. Particle size effect on catalytic activity of carbon-supported Pt nanoparticles for complete ethylene oxidation. *Appl Catal* 464 - 465, 87 - 94 (2013).

36. Cao, Z. et al. Platinum-nickel alloy excavated nano-multipods with hexagonal close-packed structure and superior activity towards hydrogen evolution reaction. *Nat Commun* 8, 15131 (2017).

37. Zhang, X. et al. Platinum - copper single atom alloy catalysts with high performance towards glycerol hydrogenolysis. *Nat Commun* 10, 5812 (2019).

38. Liu, H. et al. Uniformly dispersed platinum-cobalt alloy nanoparticles with stable compositions on carbon substrates for methanol oxidation reaction. *Sci Rep* 7, 11421 (2017).

39. Miao, R. et al. Platinum-palladium alloy nanotetrahedra with tuneable lattice-strain for enhanced intrinsic activity. *Catal Sci Technol* 10, 6173 - 6179 (2020).

40. Dey, S. & Jain, V. K. Platinum group metal chalcogenides: Their syntheses and applications in catalysis and materials science. *Platin Met Rev* 48, 16 - 29 (2004).

41. Choi, W. et al. Recent development of two-dimensional transition metal dichalcogenides and their applications. *Mater Today* 20, 116 - 130 (2017).

42. Zhang, X. et al. A facile and universal top-down method for preparation of monodisperse transition-metal dichalcogenide nanodots. *Angew Chem Int Ed* 54, 5425 - 5428 (2015).

43. Guo, G. Y. & Liang, W. Y. The electronic structures of platinum dichalcogenides: PtS_2, $PtSe_2$ and $PtTe_2$. *J. Phys. C*: *Solid State Phys* 19, 995 - 1008 (1986).

44. Zhao, Y. et al. Extraordinarily strong interlayer interaction in 2D layered PtS_2. *Adv Mater* 28, 2399 - 2407 (2016).

45. Shanmugam, V. et al. A Review of the synthesis, properties, and applications of 2D materials. *Part Part Sys Charact* 39, 127332 (2022).

46. Chia, X. et al. Layered platinum dichalcogenides (PtS_2, $PtSe_2$, and $PtTe_2$) electrocatalysis: Monotonic dependence on the chalcogen size. *Adv Funct Mater* 26, 4306 - 4318 (2016).

47. Zhao, J. *et al.* Amorphous-crystalline porous ruthenium selenide as highly efficient electrocatalysts for alkaline hydrogen evolution. *Chem Eng J* 485, 150074 (2024).

48. Wang, Y. *et al.* Sulfurization-induced partially amorphous palladium sulfide nanosheets for highly efficient electrochemical hydrogen evolution. *Chem Commun* 57, 1368 - 1371 (2021).
49. Pan, S. *et al.* Activation of rhodium selenides for boosted hydrogen evolution reaction via heterostructure construction. *Mater Today Phys* 18, 100401 (2021).
50. Dionisiev, I. et al. Synthesis and characterizations of 2D platinum diselenide. *Mater Proc* 2, 22 (2020).
51. Wang, Z., Li, Q., Besenbacher, F. & Dong, M. Facile synthesis of single crystal $PtSe_2$ nanosheets for nanoscale electronics. *Adv Mater* 28, 10224 - 10229 (2016).
52. Xu, H. et al. Controlled doping of wafer-scale $PtSe_2$ films for device application. *Adv Funct Mater* 29, 1805614 (2019).
53. Daws, S. et al. Platinum diselenide $PtSe_2$: An ambient-stable material for flexible electronics. *Mater Sci Eng B* 283, 115824 (2022).
54. Zeng, L. et al. Ultrafast and sensitive photodetector based on a $PtSe_2$/silicon nanowire array heterojunction with a multiband spectral response from 200 to 1550 nm. *NPG Asia Mater* 10, 352 - 362 (2018).
55. Wang, W. et al. Investigation of the band alignment at $MoS_2/PtSe_2$ heterojunctions. *Appl Phys Lett* 114, 201601 (2019).
56. Song, S. et al. Air-stable van der Waals $PtTe_2$ conductors with high current-carrying capacity and strong spin-orbit interaction. *iSci* 25, 105346 (2022).
57. Zhao, Y. et al. High-electron-mobility and air-stable 2D layered $PtSe_2$ FETs. *Adv Mater* 29, 1604230 (2017).
58. Avsar, A. et al. Defect induced, layer-modulated magnetism in ultrathin metallic $PtSe_2$. *Nat Nanotechnol* 14, 674 - 678 (2019).
59. Kim, H. S. et al. Improvement of electrical performance using $PtSe_2/PtTe_2$ edge contact synthesized by molecular beam epitaxy. *Appl Surf Sci* 585, 152507 (2022).
60. Wen, R. et al. Hydrothermal synthesis of WSe_2 films and their application in high-performance photodetectors. *Appl Phys A Mater Sci Process* 124, 1 - 8 (2018).
61. Aliabadi, M. Controllable synthesis of $NiSe_2$ nanostructures via hydrothermal process for photocatalytic and solar cell applications. *J Inorg Organomet Polym Mater* 27, 73 - 79 (2017).
62. Khan, A. U. et al. Hydrothermal assisted synthesis of novel $NiSe_2$/CuO nanocomposite: Extremely stable and exceptional energy storage performance for faradaic hybrid supercapacitors. *J Electroanal Chem* 920, 116624 (2022).
63. Luo, L. et al. Hydrothermal synthesis of MoS_2 with controllable morphologies and its adsorption properties for bisphenol A. *J Saudi Chem Soc* 23, 762 - 773 (2019).

64. Wang, Z. et al. One-pot hydrothermal synthesis of $MoSe_2$ nanosheets spheres-reduced graphene oxide composites and application for high-performance supercapacitor. *J Mater Sci: Mater Electron* 30, 8537 - 8545 (2019).
65. Umar, A. A., Saad, S. K. & Salleh, M. M. Scalable mesoporous platinum diselenide nanosheet synthesis in water. *ACS Omega* 2, 3325 - 3332 (2017).
66. Loiudice, A., Lecina, O. S. & Buonsanti, R. Atomic control in multicomponent nanomaterials: when colloidal chemistry meets atomic layer deposition. *ACS Mater Lett* 2, 1182 - 1202 (2020).
67. Saldanha, P. L., Lesnyak, V. & Manna, L. Large scale syntheses of colloidal nanomaterials. *Nano Today* 12, 46 - 63 (2017).
68. Strach, M. et al. Insights into reaction intermediates to predict synthetic pathways for shape-controlled metal nanocrystals. *J Am Chem Soc* 141, 16312 - 16322 (2019).
69. Yin, Y. & Alivisatos, A. P. Colloidal nanocrystal synthesis and the organic-inorganic interface. *Nat* 437, 664 - 670 (2005).
70. Peng, Z. A. & Peng, X. Nearly monodisperse and shape-controlled CdSe nanocrystals via alternative routes: Nucleation and growth. *J Am Chem Soc* 124, 3343 - 3353 (2002).
71. Chang, J. & Waclawik, E. R. Colloidal semiconductor nanocrystals: Controlled synthesis and surface chemistry in organic media. *RSC Adv* 4, 23505 - 23527 (2014).
72. Reiss, H. The growth of uniform colloidal dispersions. *J Chem Phys* 19, 482 - 487 (1951).
73. Du, Y. et al. Near-infrared photoluminescent Ag_2S quantum dots from a single source precursor. *J Am Chem Soc* 132, 1470 - 1471 (2010).
74. Ndala, Z. B. et al. Unravelling the effects of surface functionalization on the catalytic activity of $ReSe_2$ nanostructures towards the hydrogen evolution reaction. *Appl Surf Sci* 612, 155971 (2023).
75. Khan, M. D., Opallo, M. & Revaprasadu, N. Colloidal synthesis of metal chalcogenide nanomaterials from metal-organic precursors and capping ligand effect on electrocatalytic performance: Progress, challenges and future perspectives. *Dalton Trans* 50, 11347 - 11359 (2021).
76. Kaur, M., Kumar, P. & Ghotra, H. S. A review on advances in photoelectrochemical (PEC-type) photodetectors: A trending thrust research area. *Int J Hydrog Energy* 49, 1095 -1112 (2024).
77. Queyriaux, N. et al. Molecular cathode and photocathode materials for hydrogen evolution in photoelectrochemical devices. *J Photochem Photobiol C* 25, 90 - 105 (2015).
78. Ahmed, M. & Dincer, I. A review on photoelectrochemical hydrogen production systems: Challenges and future directions. *Int J Hydrog Energy* 44, 2474 - 2507 (2019).

79. Zhuang, H. et al. Construction of g-C_3N_4-based photoelectrodes towards photoelectrochemical water splitting: A review. *J Alloys Compd* 969, 172302 (2023).
80. Kumar, M. et al. Recent trends in photoelectrochemical water splitting: the role of cocatalysts. *NPG Asia Mater* 14, 88 (2022).
81. Kim, J. Y. et al. MXene-based hybrid materials for electrochemical and photoelectrochemical H_2 generation. *J Energy Chem* 93, 111 - 125 (2024).
82. Ding, P. et al. Photocathode engineering for efficient photoelectrochemical CO_2 reduction. *Mater Today Nano* 10, 100077 (2020).
83. Candea, R. M. et al. Photoelectrolysis of water: Si in salt water. *J Appl Phys* 47, 2724 - 2726 (1976).
84. Kang, J. et al. Band offsets and heterostructures of two-dimensional semiconductors. *Appl Phys* Lett 102, 012111 (2013).
85. Kwon, K. C. et al. Wafer-scale transferable molybdenum disulfide thin-film catalysts for photoelectrochemical hydrogen production. *Energy Environ Sci* 9, 2240 - 2248 (2016).
86. Li, J. & Wu, N. Semiconductor-based photocatalysts and photoelectrochemical cells for solar fuel generation: A review. *Catal Sci Technol* 5, 1360 - 1384 (2015).
87. Gao, M. et al. Solar absorber material and system designs for photothermal water vaporization towards clean water and energy production. *Energy Environ Sci* 12, 841 - 864 (2019).
88. Xu, X. T. et al. Rational design and construction of cocatalysts for semiconductor-based photo-electrochemical oxygen evolution: A comprehensive review. *Adv Sci* 6, 1801505 (2019).
89. Ma, J., Ahn, S. H. & Kim, S. Y. Integration of earth-abundant cocatalysts for high-performance photoelectrochemical energy conversion. *J Energy Chem* 88, 336 - 355 (2024).
90. Patel, M. et al. WS_2/p-Si-based photocathodes with high activity originated from the unique vertical geometry of the 2D WS_2 nanoplatelets. *FlatChem* 33, 100361 (2022).
91. Morales-Guio, C. G. et al. Solar hydrogen production by amorphous silicon photocathodes coated with a magnetron sputter deposited Mo_2C catalyst. *J Am Chem Soc* 137, 7035 - 7038 (2015).
92. Hasani, A. et al. Direct synthesis of two-dimensional MoS_2 on p-type Si and application to solar hydrogen production. *NPG Asia Mater* 11, 47 (2019).
93. Kempler, P. A. et al. Hydrogen evolution with minimal parasitic light absorption by dense Co-P catalyst films on structured p-Si photocathodes. *ACS Energy Lett* 3, 612 - 617 (2018).
94. Wang, Z. et al. Nickel-based cocatalysts for photocatalysis: Hydrogen evolution, overall water splitting and CO_2 reduction. *Mater Today Phys* 15, 100279 (2020).

95. Chen, F. et al. Efficient photoelectrochemical hydrogen evolution on silicon photocathodes interfaced with nanostructured NiP_2 cocatalyst films. *ACS Appl Mater Interfaces* 8, 31025 - 31031 (2016).
96. Li, J. & Wu, N. Semiconductor-based photocatalysts and photoelectrochemical cells for solar fuel generation: A review. *Catal Sci Technol* 5, 1360 - 1384 (2015).
97. Yang, X. & Wang, D. Photocatalysis: From fundamental principles to materials and applications. *ACS Appl Energy Mater* 1, 6657 - 6693 (2018).
98. Heo, J. et al. Surface engineering of Cu_2O photocathodes via facile graphene oxide decoration for improved photoelectrochemical water splitting. *ACS Omega* 8, 32794 - 32803 (2023).
99. Cheng, J., Wu, L. & Luo, J. Improving the photovoltage of Cu_2O photocathodes with dual buffer layers. *Nat Commun* 14, 7228 (2023).
100. Khusnun, N. F. et al. An avant-garde of carbon-doped photoanode materials on photo-electrochemical water splitting performance: A review. *J Electroanal Chem* 929, 117139 (2023).
101. Wei, B. Q., Vajtai, R. & Ajayan, P. M. Reliability and current carrying capacity of carbon nanotubes. *Appl Phys Lett* 79, 1172 - 1174 (2001).
102. Wei, Y. et al. Multi-walled carbon nanotubes modified ZnO nanorods: A photoanode for photoelectrochemical cell. *Electrochim Acta* 143, 188 - 195 (2014).
103. Yousefzadeh, S. et al. MWCNT/WO_3 nanocomposite photoanode for visible light-induced water splitting. *J Solid State Chem* 204, 341 - 347 (2013).
104. Rai, S. et al. Photoactivity of MWCNTs modified α-Fe_2O_3 photoelectrode towards efficient solar water splitting. *Renew Energy* 83, 447 - 454 (2015).
105. Yang, G. & Park, S. J. Conventional and microwave hydrothermal synthesis and application of functional materials: A review. *Mater* 12, 1177 (2019).
106. Li, X. et al. Carbon nanotube hybrids with MoS_2 and WS_2 synthesized with control of crystal structure and morphology. *Carbon* 85, 168 - 175 (2015).
107. Zhao, D. et al. Multifunctional flower-like WS_2 hybrids with carbon nanotube veins and WS_2 petals: Its sodium ion storage and hydrogen evolution properties. *Chem Phys* 545, 111146 (2021).
108. Zhang, Z. et al. Friction and wear behaviors of MoS_2-multi-walled-carbon nanotube hybrid reinforced polyurethane composite coating. *Friction* 7, 316 - 326 (2019).
109. Cao, J. et al. A clean and facile synthesis strategy of MoS_2 nanosheets grown on multi-wall CNTs for enhanced hydrogen evolution reaction performance. *Sci Rep* 7, 8825 (2017).
110. Zhang, W. X. et al. NiS_2@MWCNTs as a promising anode material for lithium and sodium-ion batteries with superior cycling stability. *J Alloys Compd* 971, 172669 (2024).

111. Azad, M., Hussain, Z. & Baig, M. M. MWCNTs/NiS_2 decorated Ni foam-based electrode for high-performance supercapacitors. *Electrochim Acta* 345, 136196 (2020).
112. Serhan, M. et al. Ni-Doped ZrO_2 Nanoparticles decorated MW-CNTs nanocomposite for highly sensitive electrochemical detection of 5-Amino salicylic acid. *Analyst* 146, 664 - 673 (2021).
113. Mxakaza, L. et al. Cu_2ZnSnS_4/N-MWCNTs hybrid systems as counter electrode substitutes for platinum in dye-sensitized solar cells. *J Mater Res* 39, 689 - 701 (2024).

Chapter 3

Synthesis and characterization of $PtSe_2$ and $PtTe_2$ nanomaterials via colloidal synthesis: Tailoring chalcogenide precursors for enhanced alkaline hydrogen evolution reaction performance

3.1 Introduction

The enormous need to expand the global energy systems brought about by the escalating energy demand can be fulfilled by renewable energy. While hydrogen is not a renewable energy source, it is regarded as a renewable energy storage.[1,2] Energy harnessed from renewable energy reservoirs, wind, and solar, is used to produce hydrogen through the splitting of water molecules to H_2 and O_2. H_2 produced from water electrolysis has a high calorific value and zero carbon emission rendering this type of hydrogen a suitable alternative energy source to fossil fuels.[3,4] Highly efficient hydrogen evolution reaction (HER) catalysts currently employed in this process are noble metals such as Pt/C or Ru.[5] However, these are poisoned by the electrolytes used in HER, are expensive, and have limited reserves in the earth's crust. A vast amount of research has been channelled toward HER in acid media.[6–8] This is because acid HER is kinetically easier to achieve than HER in alkaline media. Acid medium HER uses a proton-exchange membrane (PEM), imparting efficient energy usage and high hydrogen production rate. PEMs are constructed from expensive polymers, and their conductivity is reduced by cationic impurity poisoning.[9] The HER efficiency of most electrocatalysts is reported to decline with increasing electrolyte pH, even for platinum. However, alkaline HER is more industrially feasible as it eliminates the employment of pricey proton-exchange membranes.[5,10,11] Anion exchange membranes, which transport OH^- ions, are employed in alkaline electrolysis and offer low cost, and resistance to carbonate impurity formation benefits.[12] More accessible, highly stable, and highly efficient alkaline HER catalyst substitutes are therefore sought after, to reduce the overall cost of the HER process. Transition metal dichalcogenides (TMDs), particularly group 6 TMDS, such as NiS_2 and $MoTe_2$ have been explored as HER catalysts in an acidic medium.[13–15] There is limited research on employing group 10 TMDs as HER catalysts. Group 10 TMDs are a fascinating class of TMDs because of the more intensive electronic interaction between the chalcogen p-orbitals and the Group 10 transition metal d-orbitals, due to the vicinity of the energy levels of these orbitals.[16] Interestingly, the extent of hybridization for Pt dichalcogenides increases down the chalcogen group, resulting in PtS_2 being semi-conductive, and $PtSe_2$ being semi-metallic or semiconductive depending on the number of layers.[17] $PtSe_2$ naturally occurs in 1T phase and a few layers (1- 4 layers) of this material illustrate

a p-type indirect band gap semiconductor nature.[18] On the other hand, greater than 5 layers of $PtSe_2$ display a semi-metallic nature without a bandgap.[19] These studies were largely based on computational studies rather than experimental data. Pt-Te systems exhibit a more metallic nature. Pt_xTe_y exists in several stoichiometries; PtTe, $PtTe_2$, Pt_2Te_3, and Pt_3Te_4.[20] The crystal structure, properties, and crystallinity of PtX_2, as with other TMDs, largely depend on the preparation method employed. Mechanical exfoliation, chemical vapor deposition method, and thermally assisted conversion are some of the most common synthesis methods for PtX_2.[21–23] The shortcomings of these synthesis procedures is the limited control of the size and low yields of the prepared nanosheets of PtX_2. Umar et al. reported, for the first time, a solution-based synthesis of $PtSe_2$ in aqueous medium, to produce mesoporous $PtSe_2$ sheets.[24] This synthesis method offers the possibility of preparing sizeable amounts of catalysts. Hot-injection colloidal synthesis involves rapid elemental precursor solution addition to a hot solvent. This provides a monomer supersaturation and nucleation that results in a narrow size distribution of the quantum dots produced.[25,26] Colloidal synthesis has been previously explored for TMDs and optimizing the reaction conditions resulted in the formation of TMDs with different morphologies, ranging from nanoflowers to nanosheets, and flakes.[7,27] Using this synthesis process to prepare $PtSe_2$ and $PtTe_2$, we explore how different Se and Te precursors; elemental selenium (Se), selenourea (SeU), sodium selenite (Na_2O_3Se), elemental tellurium, sodium tellurite (Na_2O_3Te), and tellurium tetrachloride ($TeCl_4$) influence the morphology and stoichiometry of platinum selenide and platinum telluride, and ultimately the role the properties play in the hydrogen evolution reaction in an alkaline medium.

Te and Se are semi-metallic elements that exist as either amorphous or crystalline structures. The hexagonal Se and Te crystal structure is comprised of clusters of long-chain covalently bonded Se/Te atoms, shown in Figure 3.1 (a). These chains are held together by weak van der Walls interactions in Se whereas π interactions exist between Te chains.[28,29] Generally, Te-Te bond strength is weaker than that of Se-Se and S-S bond.[30] SeU is a seleno-carbonyl derivative prepared by direct substitution of oxygen in urea with a selenium atom. This compound features one lone pair of electrons on each of the nitrogen atoms, which influences its reaction properties.[31] The lone pair orbitals on nitrogen contain labile electrons that are delocalized resulting in three resonance forms of SeU, shown in Figure 3.1 (b), with the first being the more stable form.[32] This charge delocalization from the two nitrogen atoms results in a relatively elongated C=Se bond and a much stronger and shorter C-N sigma bond than its parent structure, urea.[33] Subsequently, this electron-donating effect of the nitrogen atoms renders this molecule an effective ligand that can interact with transition metals through the Se atom. Na_2O_3Se is an inorganic salt commonly used in

biological applications as a Se source. The crystal structure of Na_2O_3Se contains two Na^+ ions and selenium oxyanions (SeO_3^{2-}). The SeO_3^{2-} acts as both a monodentate and a chelating ligand in the structure. The coordination of the two Na^+ ions in the structure varies, with four monodentate and one chelating SeO_3^{2-} binding to one Na^+ ion (Figure 3.1 (c)), while two monodentate and two chelating selenite ions are coordinated to the 2nd Na^+ ion (Figure 3.1 (d)). Anhydrous sodium tellurite, Na_2O_3Te, is an inorganic, slightly reducing tellurium compound that has a similar crystal structure to Ag_2O_3Te. In the TeO_3^{2-}, Te is coordinated to 6 oxygen atoms, three at a bond length of 1.87 Å and three with a longer bond length of 2.9 Å and has a +4 oxidation number. These result in a distorted octahedral geometry.[32] $TeCl_4$ is a tetrameric inorganic compound that forms a cubane structure with four Te and four bridging Cl atoms alternating in the cubic structure and three terminal Cl ligands each Te, shown in Figure 3.1 (e).[34] The bond length between Te and terminal Cl atoms is 2.31 Å while the distance between the Te atoms and the bridging Cl atoms is slightly longer at 2.93 Å.[35]

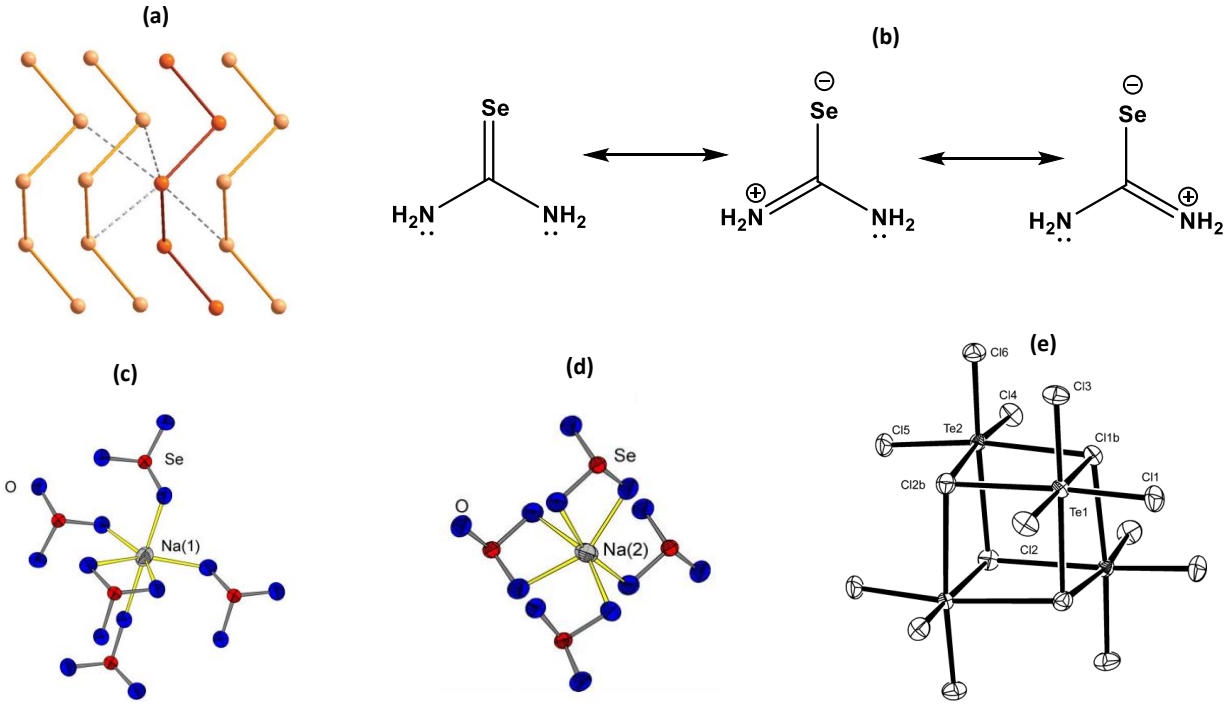

Figure 3.1: (c) The crystal structure of sodium selenite showing different bonding environments of the two Na^+ ions.[32]

3.2 Methodology

3.2.1 Chemicals and Materials

Oleylamine (OLA, 70 %, $C_{18}H_{37}N$, Sigma-Aldrich), oleic acid ($C_{18}H_{34}O_2$, O.A., 90 %, Sigma-Aldrich), platinum (II) acetylacetonate ($C_{10}H_4O_4Pt$, Pt $(AcAc)_2$, Sigma-Aldrich), selenium powder (Se, 99.5 %, Sigma-Aldrich), selenourea (CH_3N_2Se, SeU, 99 %, Sigma-Aldrich), sodium selenite (Na_2O_3Se, 99 %, Sigma-Aldrich), tellurium (Te, 99.8 %, Sigma-Aldrich) trioctylphosphine ($C_{24}H_{51}P$, 97 %, Sigma-Aldrich), platinum tetrachloride ($PtCl_4$, 96 %, Sigma-Aldrich) sodium tellurite (Na_2O_3Te, 99 %, Sigma-Aldrich), tellurium tetrachloride ($TeCl_4$, 99 %, Sigma-Aldrich), toluene (C_7H_8, 99 %), Nafion perfluorinated resin solution (5 weight %), isopropanol (C_3H_8O, 99 %, Sigma-Aldrich), ultra-pure water, ethanol (C_3H_5OH, 99.9 %, Sigma-Aldrich), 40 % commercial Pt/C (Tanaka Kikinzoku Kogyo), graphite rod (Metrohm), Ag/AgCl auxiliary reference electrode (Metrohm), glassy carbon electrode (GC, Metrohm), potassium hydroxide (KOH, 85 %, Sigma-Aldrich) and annealed carbon black (Johnson and Mathey).

3.2.2 Colloidal Synthesis of $PtSe_2$

A hot injection synthesis procedure of platinum and selenium precursors in a hot organic solvent was employed to prepare $PtSe_2$. The procedure was adapted and modified from the reported colloidal synthesis of metal selenides.[36–38] A 1:1 v/v (total volume = 10 mL) ratio of OLA and O.A was added to a three-neck glass round bottom flask connected to a condenser with a constant nitrogen flow. The solvent mixture was then heated to 320 ℃ using an electro mantle with a maximum heating temperature of 380 ℃ equipped with a magnetic stirrer. The solution was systematically stirred to ensure uniform heat distribution. At this point, a mixture of $Pt(Acac)_2$, (0.244 mol) and Se precursor (0.488 mol; Se, SeU, sodium selenite) was injected. The solvent solution immediately changed color from pale yellow to black. The reaction temperature was then maintained at 320 ℃ for 1 h, followed by cooling to 60 ℃ and the addition of toluene to precipitate out the nanoparticles. The $PtSe_2$ nanoparticles were ultimately isolated by centrifuging the obtained solution at 8000 rpm for 10 min for three cycles, then dried in the fume hood.

3.2.3 Colloidal Synthesis of $PtTe_2$

Similarly, a hot injection colloidal synthesis procedure adapted and modified from the colloidal synthesis of WTe_2 and $MoTe_2$, was employed for the preparation of $PtTe_2$.[39,40] 8 mL of OLA and 2 mL of TOP were added to a three-neck round bottom flask, connected to the Schlenk line. The system was saturated with nitrogen gas while stirring and heating the solution to 320 ℃, using a

magnetic stirrer equipped electric heating mantle. Steady stirring of the solution was carried out to ensure uniform heat distribution. In a vial, $PtCl_4$ (0.270 mol) and tellurium precursor (0.54 mol, Te, $TeCl_4$, or Na_2O_3Te) were then injected into the hot pale-yellow solution which immediately turned black. The solution temperature was then maintained at 320 ℃ for 1 h. The reaction solution temperature was then allowed to decline to 60 ℃ and toluene was added to precipitate out the $PtTe_2$ nanoparticles. The cool solution was then placed in centrifuge tubes, transferred to the centrifuge, and rotated for 10 min at 8000 rpm. The liquid was discarded and the black product dried in the fume hood, crushed, and analyzed.

3.2.4 Physical Characterization Techniques

The Raman spectra were recorded on a Horiba Scientific MacroRam Raman Spectrometer equipped with a 785 nm laser, Olympus BX41 microscope, and the crystallographic parameters of the nanoparticles were analyzed by X-ray diffraction (XRD) using a Bruker D2 Phaser Powder X-ray diffractometer fitted with a Cu Kα X-ray source (1.54 nm). Measurements were taken over 2θ angle range 10-90° in steps of 0.026° with a step time of 5s at ambient conditions. The Scherrer formula, Eqn 3.1, was employed to estimate the crystallite size of the nanoparticles. The peaks between 2θ angle range of 10-55° were employed in the calculations and Origin software was used to determine the peak positions and FWHM. Fourier Transform Infra-Red (FTIR) analysis was conducted using a Thermo Scientific OMNIC Macros/Basic Omnic Spectroscopy equipped with Nicolet iS20 software. High-Resolution Transmission Electron Microscopy (HRTEM, using JEOL JEM 2100 at 200 kV equipped with a Thermo Fischer detector for EDS analysis), and X-ray photoelectron spectroscopy (XPS, Thermo Scientific ESEAlab 250Xi using a 300 W Monochromatic Al kα (1486.7 eV) X-ray beam with a diameter of 900 µm and 20 eV pass energy) characterization techniques were employed to ascertain the morphology and the elemental oxidation states in the nanomaterials.

$$D_p = \frac{K\lambda}{\beta cos\theta} \quad \text{.....Eqn 3.1}$$

Where D_p is the crystallite size, K is a shapeless dimension factor taken as 0.94 in this study, β is the line broadening at half maximum peak height (FWHM), λ is the X-ray source wavelength and θ is the Bragg`s angle.

3.2.5 Electrochemical Characterization Techniques

The HER activity and the resistance of the prepared catalysts were determined through electrochemical measurements carried out using the Biologic SP 300, rotating disk potentiostat. A

three-electrode cell set-up comprising of graphite rod (counter electrode), Ag/AgCl (reference electrode), and modified glassy carbon working electrode (glassy carbon coated with an ink of the prepared catalysts, area = 0.196 cm^2) all immersed in 1 M KOH (pH = 14) electrolyte were used for the measurements. A 2.55 mL dissolving solution containing 1 mL isopropanol, 1.5 mL ultrapure water, and 50 µL of Nafion was used to disperse 3.0 - 3.2 mg of the $PtSe_2$ and $PtTe_2$ catalysts and 1.0 - 1.2 mg of carbon black. The ink mixture was sonicated and then 10 µL of the ink was drop-casted on a pre-cleaned 0.196 cm^2 glassy carbon electrode (previously cleaned by scrubbing on a 1.0 µm and 0.5 µm alumina paste and rinsing with ultra-pure water). The ink formulation, electrode fabrication, and the electrochemical measurements set-up are illustrated in Figure 3.2. The ink was dried by rotating the glassy carbon at 250 rpm for approximately 45 min. The calculated catalyst loading was 80 - 88 μgcm^{-2} using Eqn. 3.2. The Pt, Se, and Te quantities in the ink were determined by ICP-OES conducted on a Thermo Icap 6500 ICP-OES. Linear sweep voltammetry scans of the electrode at 5 mV/s were obtained by applying a potential (-2 V to 0.5 V) to the working electrode while rotating the working electrode at 1600 rpm. The electrochemical impedance spectroscopy (EIS) was carried out by applying potential from the LSV curve at onset potential at a frequency range of 0.1 Hz-100 kHz while rotating at 1600 rpm. The stability of the electrodes was determined by running the LSV before and after 1000 CV cycles, and by studying the current density response over time using current-time chronoamperometry (CA) studies carried out at η_{-10}. Temperature dependence LSV studies were done by connecting the cell to a water bath fitted with a small pump. LSV curves were then obtained when the electrolyte temperature was set at 298 K, 308 K, 318 K, 328 K, and 338 K in the potential window of -0.2 V to 0.5 V. All measurements were performed in a 150 mL electrochemical cell conjugated with argon gas at a scan rate of 5 mVs^{-1}. Before plotting, the potential was corrected against the reference hydrogen electrode (RHE) using Eqn. 3.3 and Eqn. 3.4.

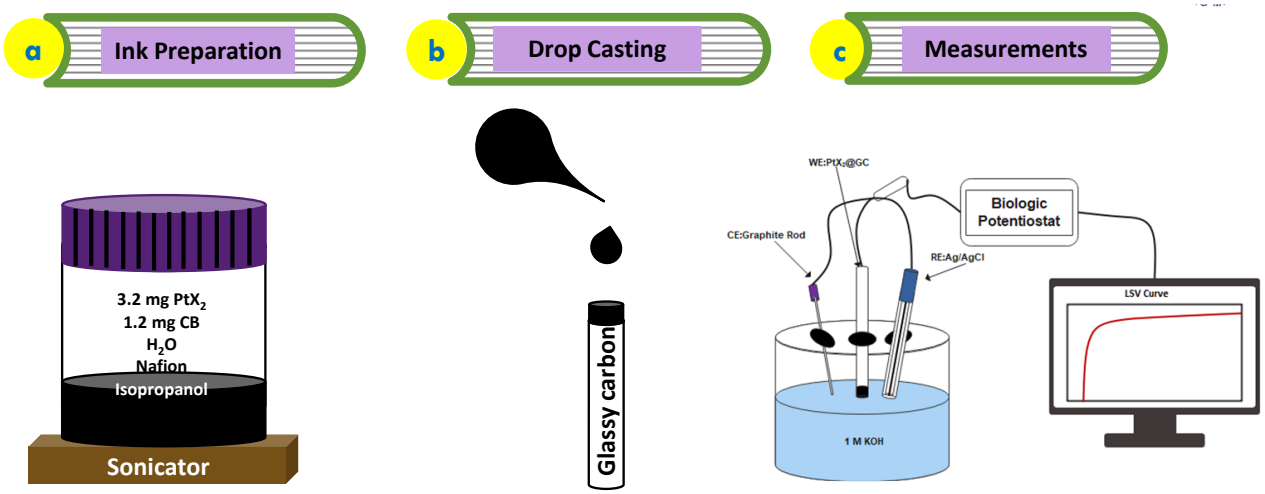

Figure 3.2: Schematic diagram depicting the catalyst (a) ink formulation, (b) electrode fabrication, and (c) the electrochemical measurement set-up.

Catalyst Loading Calculation:

Dissolving solution = 2.55 µL

Catalyst: Carbon black = 1.0 mg – 1.2 mg

$PtSe_2/PtTe_2$ = 3.0 mg – 3.2 mg

Catalyst total mass = **4.0 mg – 4.4 mg**

[Ink] = (4.0 mg – 4.4 mg)/2.55 µL of which **10 µL** was drop cast on the glassy carbon electrode (Area = **0.195 cm^2**).

Catalysts loading = $\frac{Mass\ of\ catalyst}{Volume\ of\ solvent} \times \frac{Volume\ of\ ink\ taken}{1} \times \frac{1}{Area\ of\ electrode}$ ……..….**Eqn 3.2**

∴ **Catalysts loading =** $\left(\frac{4.0}{2.55} \times 10\ \mu L \times \frac{1}{0.196}\right)$ **to** $\left(\frac{4.4}{2.55} \times 10\ \mu L \times \frac{1}{0.196}\right)$ **= 80 – 88 µg/cm^2**

$$E_{RHE} = E_{corrected} + (0.059 * pH) + E_{calibrated} \quad \text{..... Eqn 3.3}$$

$$E_{corrected} = E_{measured} - (iR) \quad \text{.....Eqn 3.4}$$

Where *i* is the measured current, R is solution resistance and $E_{calibrated}$ is the Ag/AgCl potential (0.197 V).

3.3 Results and Discussion

3.3.1 Optimizing $PtSe_2$ nanomaterials for efficient alkaline hydrogen evolution performance

3.3.1.1 Structure and Crystallite Size Determination of $PtSe_2$

The crystal phase of $PtSe_2$ prepared from Se, SeU, and Na_2O_3Se was determined by XRD analysis, and patterns are shown in Figure 3.3 (a). The XRD plots of the three samples exhibit three major peaks at $2\theta = 17°$, 32° and 49°, and were matched to the Sudovikovite $PtSe_2$, syn (PDF: 03-065-3374) with P-3M1 crystal planes and a = 3.724 and c = 5.067. The peaks for $PtSe_2$-SeU are broader which could be due to the relatively smaller grain sizes of this material. $PtSe_2$-Na_2O_3Se exhibits much sharper peaks, indicating that this material is relatively more crystalline than the other materials and mostly likely exhibits larger particle sizes. Unlike other prepared $PtSe_2$ catalysts, $PtSe_2$-Na_2O_3Se has traces of elemental Pt. These assumptions were further confirmed by calculating the crystallite sizes of the materials, depicted in Table 3.1, using the Scherrer equation. The obtained values were 6.9 ± 2.8 nm, 3.4 ± 0.8 nm, and 9.5 ± 3.7 nm for $PtSe_2$-Se, $PtSe_2$-SeU, and $PtSe_2$-Na_2O_3Se, respectively. $PtSe_2$-SeU is the smallest-sized, and most monodispersed material, whereas $PtSe_2$-Na_2O_3Se has the largest crystallite size and is the most polydispersed material. The small size of $PtSe_2$-SeU is responsible for the broad peaks observed in the XRD pattern of this catalyst. The variation of Se precursors influences the crystallite size of the $PtSe_2$ obtained. The HER activity of nanoparticles is dependent on their size. Klein et al. discovered that the maximum HER activity of Pt nanoparticles was achieved when the nanoparticle size was between 2.2 - 3.5 nm, and declined when the particle size was increased.[41]

Table 3.1: Crystallite size distribution of the $PtSe_2$ catalysts.

Catalyst	Mean D_p (nm)	Std Dev (nm)
$PtSe_2$-Se	6.9	2.8
$PtSe_2$-SeU	3.4	0.8
$PtSe_2$-Na_2O_3Se	9.5	3.7

3.3.1.2 Molecular signature and surface analysis of $PtSe_2$

Figure 3.3 (b) shows the Raman spectroscopy analysis of the three materials and two distinct peaks at ~ 179 cm^{-1} and ~ 209 cm^{-1}. $PtSe_2$ has four vibrational modes, two of which are Raman active, the E_{2g} and A_{1g}, and two which are FTIR active, $2A_{2u}$ and $2E_u$.[42] The low energy vibration mode is attributed to the in-plane Pt-Se stretching whereas the higher energy vibration mode is assigned to the out-of-plane stretching of the Pt-Se bond. The crystal lattice and the presence of the two Raman spectroscopy modes confirm that using elemental Se, SeU, or Na_2O_3Se as selenium precursors at 320 °C for 1 h results in the formation of $PtSe_2$. In addition to material identity determination, Raman spectroscopy is employed to determine the degree of crystallization, i.e., whether the material is crystalline or amorphous, and the type of order or disorder within the material.[43] The peak positions for both $PtSe_2$-Se and $PtSe_2$-Na_2O_3Se are identical. The peak positions and the corresponding FWHM values for the $PtSe_2$ catalysts are summarized in Table 3.2. The A_{1g} vibrational mode of $PtSe_2$-SeU is identified at a lower energy, and this peak has a slightly higher FWHM, these observations together suggest that $PtSe_2$-SeU is less crystalline than the other two catalysts.[44] This confirms the reason for broader XRD peaks of $PtSe_2$-SeU. $PtSe_2$-Na_2O_3Se has the highest FWHM for the E_{2g} peak, which can be attributed to the disorder brought about by the presence of residual Pt, as observed in the XRD pattern of this catalyst.

Table 3.2: Raman spectroscopy peak analysis of $PtSe_2$-Se, $PtSe_2$-SeU, and $PtSe_2$-Na_2O_3Se.

Catalyst	Assignment	Raman shift (cm^{-1})	FWHM (cm^{-1})
$PtSe_2$-Se	E_{2g}	178.8	18.3
	A_{1g}	208.4	20.2
$PtSe_2$-SeU	E_{2g}	178.8	19.4
	A_{1g}	206.3	21.4
$PtSe_2$-Na_2O_3Se	E_{2g}	178.8	38.1

A_{1g}	208.4	21.1

FTIR, shown in Figure 3.3 (c)-(e), for $PtSe_2$-Se, $PtSe_2$-SeU, and $PtSe_2$-Na_2O_3Se, respectively, shows the comparison of the FTIR spectrum of the organic ligands used in the colloidal synthesis to the respective $PtSe_2$. The baseline of the FTIR spectra of $PtSe_2$ were all corrected. FTIR analysis was carried out to determine the presence of the capping ligands and the mode of ligand functional group moiety interaction with $PtSe_2$. All the $PtSe_2$ samples show the presence of O-H functional groups between 3000 cm^{-1} and 3500 cm^{-1}. This suggests the presence of moisture on the $PtSe_2$. In both the ligands, we concentrated our attention on specific vibration modes. In OLA, our focus was on the C-N, =C-H, and the N-H bonds whereas for O.A., we focused on the C=C and C=O bonds. The presence of the alkene hydrogen in all the samples is evidenced by a small peak at ~ 3100 cm^{-1}. For all the catalysts, the two peaks between 750 cm^{-1} and 850 cm^{-1} suggest the presence of N-H functional groups in the material. This observation leads to the conclusion that OLA is present in both these materials. However, for $PtSe_2$-Se, the N-H peak is observed and is at the same position as in the OLA spectrum, in $PtSe_2$-Na_2O_3Se this peak completely disappears. This suggests that $PtSe_2$-Se, $PtSe_2$-SeU, and $PtSe_2$-Na_2O_3Se catalysts contain OLA. For all the samples, the C-O bond (~1700 cm^{-1}) is not observed yet there seems to be emergence of a peak around 1600 cm^{-1}. This is in line with the observation made by several authors for oleic acid-capped nanoparticles and the peaks at 1600 cm^{-1} in the FTIR spectrum of the nanomaterial are assigned to the formation of the oleate salt.[45,46] Therefore, we can conclude that both the $PtSe_2$-Se, $PtSe_2$-SeU, and $PtSe_2$-Na_2O_3Se materials are OLA and O.A. capped.

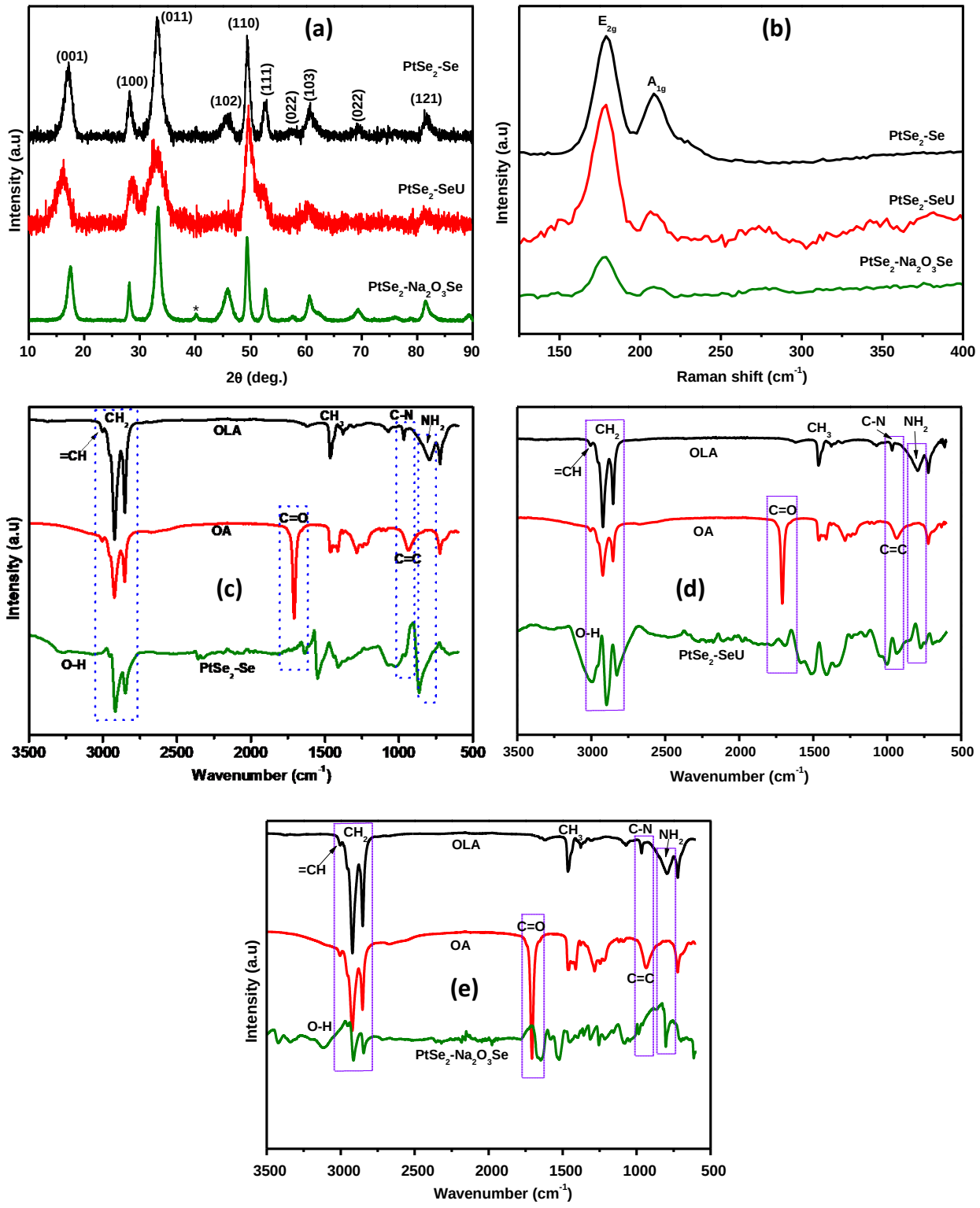

Figure 3.3: (a) XRD patterns, (b) Raman spectroscopy and comparison of FTIR spectra of OLA and OA to (c) $PtSe_2$-Se, (d) $PtSe_2$-SeU, and (e) $PtSe_2$-Na_2O_3Se.

3.3.1.3 Morphology determination of $PtSe_2$

To understand the atomic structure of $PtSe_2$ prepared from the three precursors, transition electron microscopy (TEM) analysis was carried out. Figures 3.4 (a)-(c) show the low magnification TEM

images of $PtSe_2$-Se, $PtSe_2$-SeU, and $PtSe_2$-Na_2O_3Se, respectively. Both $PtSe_2$-Se and $PtSe_2$-Na_2O_3Se exhibit almost similar petal-like structures that consist of laterally defined sheets that are stacked together and aligned either horizontally or vertically. $PtSe_2$-Selenourea exists as thin layers of crumbled-up sheets-like material. The crystallite size of $PtSe_2$-SeU was determined to be the smallest, this speaks to the much thin-layered structure of $PtSe_2$-SeU observed in the TEM image. The EDS spectrum of $PtSe_2$ in Figure 3.4 (d) shows that the main elements in this material are Pt and Se atoms. The Cu and O are attributed to the copper grid and surface oxidation.

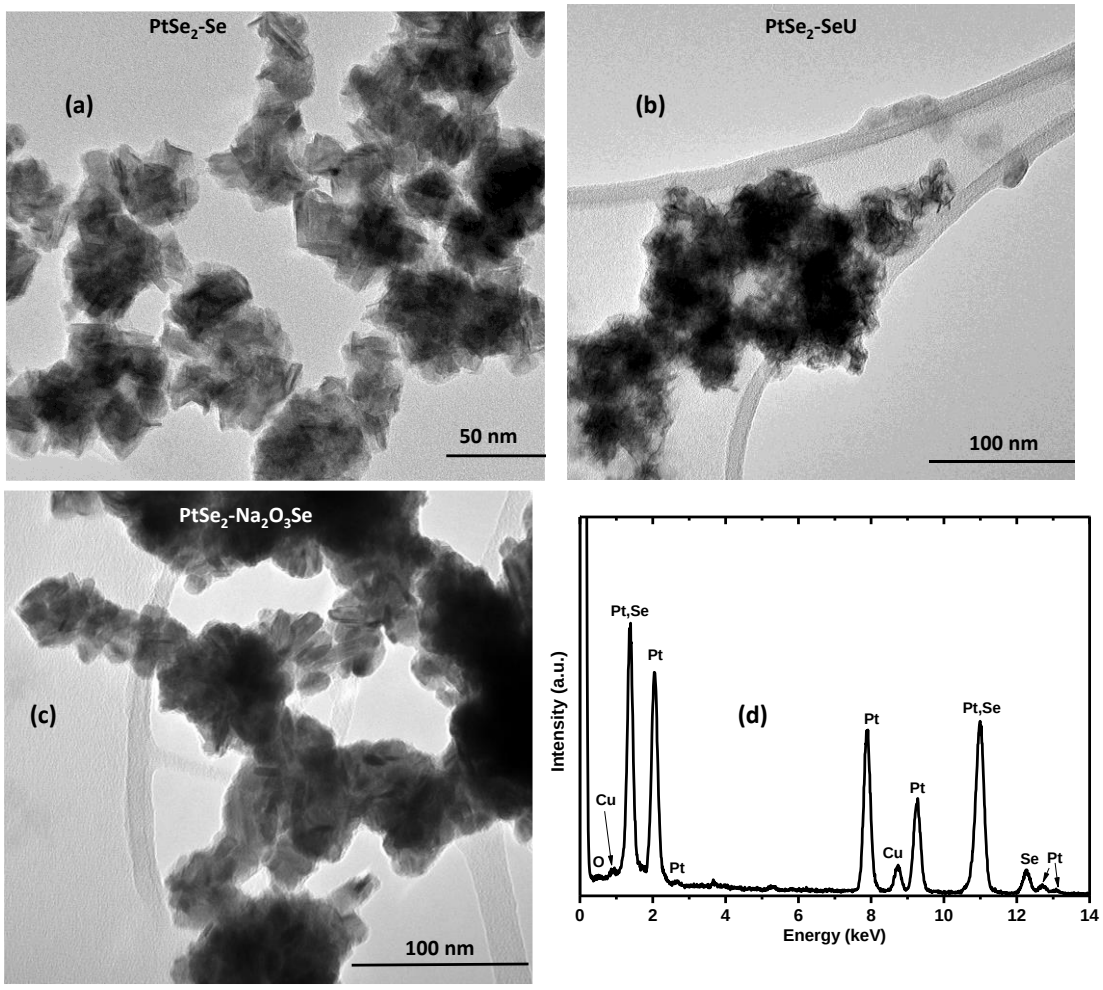

Figure 3.4: TEM images of (a) $PtSe_2$-Se, (b) $PtSe_2$-SeU, (c) $PtSe_2$-Na_2O_3Se, and (d) is the EDS spectra of $PtSe_2$-Se.

3.3.1.4 Elemental Composition Analysis of $PtSe_2$

The XPS analysis of $PtSe_2$-Se was carried out to determine the identity and oxidation states of the elements in $PtSe_2$. The survey spectrum of $PtSe_2$, shown in Figure 3.5 (a), shows that the material contained predominantly platinum, selenium, carbon, oxygen, and some traces of nitrogen. Carbon, oxygen, and nitrogen are attributed to the capping agents used in the synthesis of $PtSe_2$. The high-resolution spectrum of Pt in Figure 3.5 (b) shows the presence of two types of platinum oxidation

states. The peak pair at ~76.2 eV and 72.9 eV are attributed to Pt^{2+} whereas the peaks at 75.2 eV and 71.9 eV are attributed to elemental platinum (Pt^0). We can conclude that there is no presence of oxidized Pt within the $PtSe_2$ samples due to the absence of the PtO_2 peak at ~73.9 and ~77.3 eV.[24] The high-resolution scan of Se in Figure 3.5 (c) shows a broad peak deconvoluted into two peaks at 55.0 eV and 53.9 eV. These peaks are consistent with the Se^{2-} peaks observed for various metal selenide materials.[25] These observations suggest that colloidal synthesis of $PtSe_2$ in a mixture of oleylamine and oleic acid resulted in the formation of $PtSe_2$, with traces of unreacted Pt. These results are consistent with XPS data obtained by other authors for $PtSe_2$.[22]

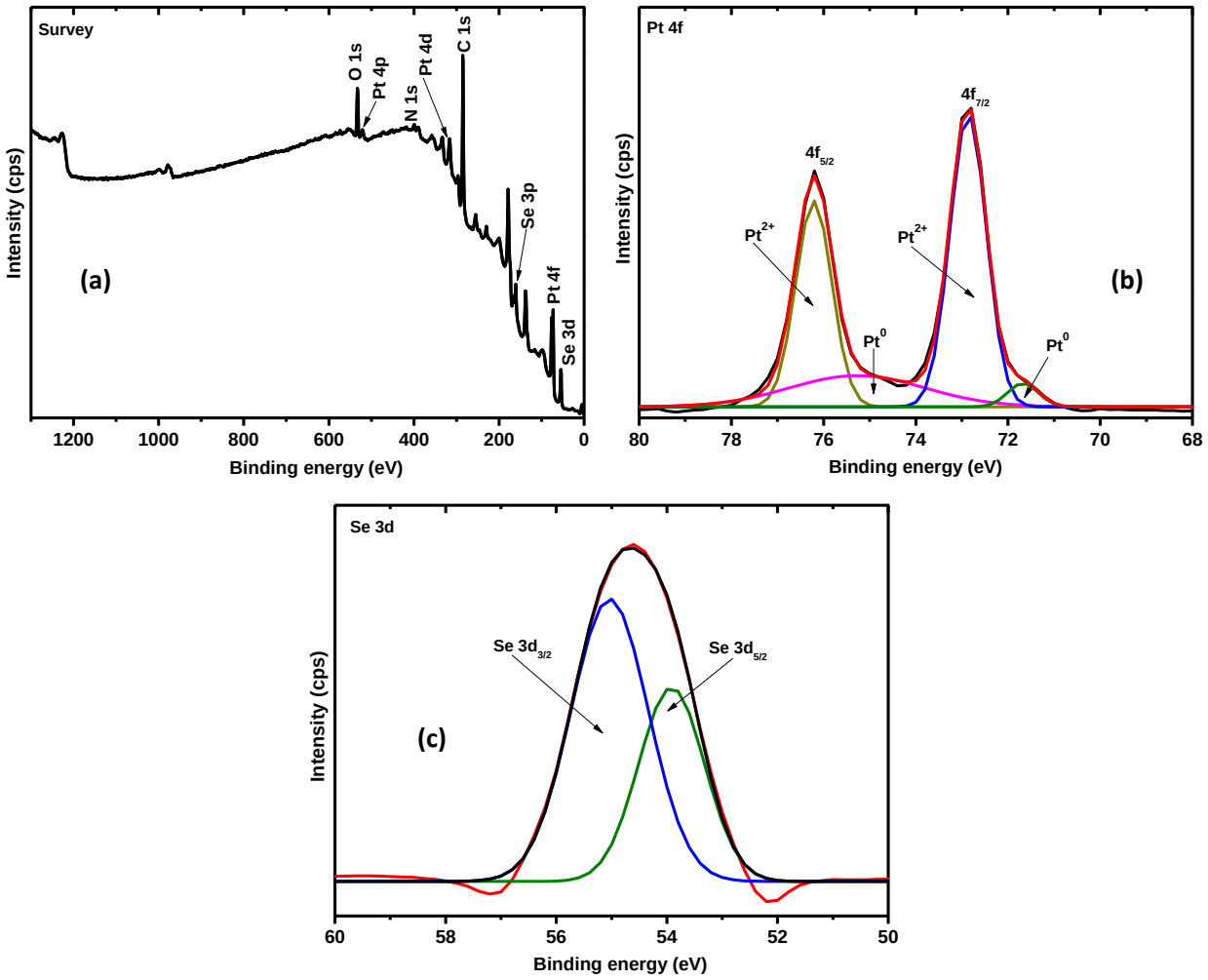

Figure 3.5: (a) XPS survey spectrum and the high-resolution spectra of (b) platinum and (c) selenium of $PtSe_2$-Se.

3.3.1.5 Hydrogen evolution reaction of $PtSe_2$

The HER activity of $PtSe_2$ catalysts prepared from Se, SeU, and Na_2O_3Se precursors was studied at 25 °C in 1 M KOH at 5 mVs^{-1} under inert conditions and the electrochemical performance parameters are summarised in Table 3.3. Cyclic voltammetry scans of $PtSe_2$-Se, $PtSe_2$-SeU and

$PtSe_2$-Na_2O_3Se catalysts are shown in Figure 3.6 (a). The reduction peak is observed at around 0.6 V while the oxidation peak is observed at 1.0 eV. The intensity of both peaks is much higher when the $PtSe_2$-Se is used, indicating a higher current response when this catalyst is utilized. A high current response could be attributed to the crystallite size of this catalyst. In the XRD analysis of the catalysts, it is noted that the size changes from 6 nm to 3.4 nm, and 9.5 nm for $PtSe_2$-Se, $PtSe_2$-SeU, and $PtSe_2$-Na_2O_3Se, respectively. The linear sweep voltammetry (LSV) curves shown in Figure 3.6 (b) show that $PtSe_2$-Se has an earlier onset potential (E_{onset}) of 46 mV. The E_{onset} of $PtSe_2$-SeU and $PtSe_2$-Na_2O_3Se are much larger at 91 mV and 71 mV, respectively. This observation suggests that the more amorphous $PtSe_2$ prepared from SeU, is a poor HER catalyst compared to $PtSe_2$-Na_2O_3Se. The trend in catalytic activity based on Eonset is PtSe2-Se > $PtSe_2$-Na_2O_3Se > PtSe2-SeU. Although $PtSe_2$-Se and $PtSe_2$-Na_2O_3Se have comparable crystallite sizes and similar morphologies, $PtSe_2$-Na_2O_3Se is more polydisperse and this can negatively affect the HER activity. E_{onset} is the potential induced to initiate the HER and is indicative of the catalytic activity of an electrode material.[47] As such, the catalytic activity of $PtSe_2$-Se can be reckoned to be higher than that of $PtSe_2$-SeU and $PtSe_2$-Na_2O_3Se. The overpotential (η_{-10}) for the three $PtSe_2$ catalysts required to produce a current density of 10 $mAcm^{-2}$ was also compared and the potential for $PtSe_2$-Se was the lowest at 162 mV. This implies that for $PtSe_2$-Se, the lowest amount of energy of the three catalysts is required to produce the same current density. On the other hand, the η_{-10} for $PtSe_2$-Na_2O_3Se is 248 mV, slightly lower than that of $PtSe_2$-SeU (255 mV). $PtSe_2$-SeU and $PtSe_2$-Na_2O_3Se show comparable overpotential values and thus require almost the same amount of energy to produce a current density of 10 $mAcm^{-2}$. The difference in the catalytic properties can be attributed to the difference in morphology of the three $PtSe_2$ materials. Both $PtSe_2$-Se and $PtSe_2$-Na_2O_3Se exist as stacked up, distinct shaped petal-like materials. This means that more edge sites are available in the two materials over the more sheet-like morphology without the distinct shape of $PtSe_2$-SeU. For $PtSe_2$-Se, which has a smaller crystallite diameter than $PtSe_2$-Na_2O_3Se, possibly more of the basal plane sides are exposed over the edge site, which is usually attributed to HER active sites in 2D TMDs.[48,49]

Tafel slope in hydrogen evolution reaction is a vital parameter related to HER kinetics on various electrode surfaces.[50] Tafel slope is obtained from the plot of overpotential against the logarithm of current density obtained from the polarization curve based on the relationship that:

$$\eta = b\log j + a \quad \text{Eqn 3.5}$$

Where η is the overpotential, b is the Tafel slope, j is the current density, and a is the intercept.

A high Tafel slope indicates a slow HER rate whereas a low Tafel slope indicates a faster kinetic reaction[51]. The value of the Tafel slope in turn gives information on the mechanism by which the HER occurs on the electrode surface. The values obtained for all the $PtSe_2$ materials indicate that the HER on $PtSe_2$ is slow compared to other studies.[52] The mechanism for HER in the basic medium involves the adsorption of water on the electrode surface (M), followed by the dissociation of the H_2O molecule to adsorbed (MH) and OH^- ions (Eqn. 3.6), and the combination of adsorbed hydrogen to produce H_2 gas (Eqn. 3.7). The specific pathways for H_2 production occur via either of the two pathways, the Volmer-Hevrosky reaction pathway or the Hevrosky-Tafel reaction pathway.[50]

i. Adsorption/dissociation step:

Volmer: $\boldsymbol{H_2O + M + e^- \rightarrow MH + OH^-}$ **.....Eqn 3.6**

ii. Desorption step

Tafel: $\boldsymbol{2MH \rightarrow H_2}$ **.....Eqn 3.7**

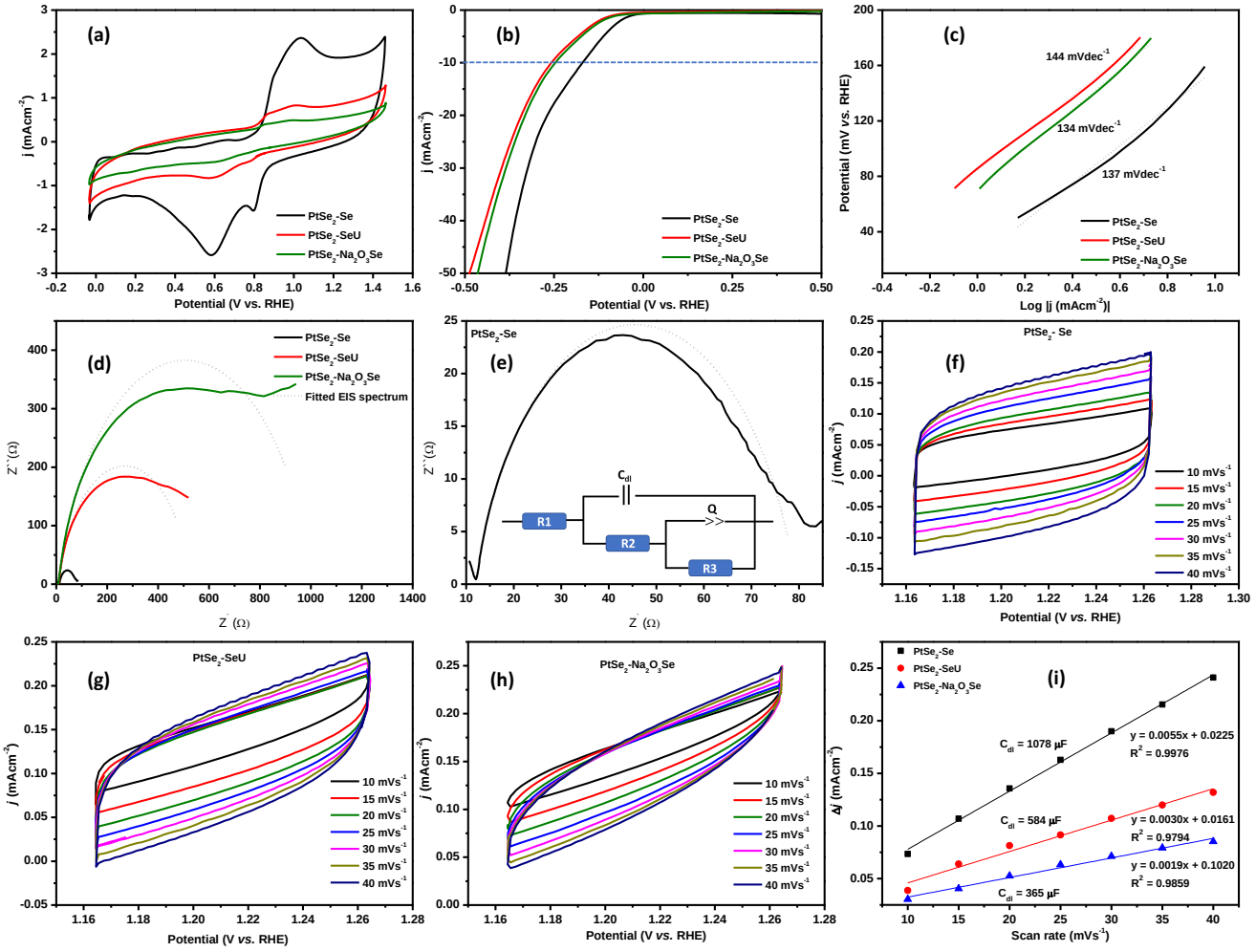

Figure 3.6: (a) CV, (b) LSV, (c) Tafel plots, (d) EIS spectra of $PtSe_2$-Se, $PtSe_2$-SeU and $PtSe_2$-Na_2O_3Se, (e) zoomed-in EIS spectrum of $PtSe_2$-Se, CV scans at increasing scan rate for (f) $PtSe_2$-Se (g) $PtSe_2$-SeU and (h) $PtSe_2$-Na_2O_3Se (i) is the C_{dl} spectra of $PtSe_2$-Se (black), $PtSe_2$-SeU, (red) and $PtSe_2$-Na_2O_3Se (blue).

The Tafel plots for the prepared catalysts are extrapolated from the LSV curves and are shown in Figure 3.6 (c). The Tafel slopes of $PtSe_2$-Se, $PtSe_2$-SeU, and $PtSe_2$-Na_2O_3Se were found to be comparable at 112, 135, and 167 $mVdec^{-1}$, respectively. This observation suggests the kinetics of HER on $PtSe_2$ is slow and the reaction mechanism on all the $PtSe_2$ samples is similar. The high Tafel slopes indicate that the Volmer step (adsorption/dissociation) is the rate-determining step of HER on $PtSe_2$.[53] This observation implies that H_2 gas is desorbed from the electrode surface faster than the H_2O is adsorbed or dissociated. Ideally, for the HER to be at maxima, both the absorption/dissociation steps and the desorption steps should occur at the same speed.[54] The dissociation of H_2O on the electrode surface is facilitated by the electron transfer of the working electrode. The rate of electrode transfer can be studied by comparing the exchange current density (j_o) of the catalyst and electrochemical impedance spectroscopy (EIS) study. J_o indicates the rate of electron transfer between the electrode and the electrolyte at equilibrium.[55] This parameter is obtained from the Tafel plot when the overpotential is zero. ($0 = \text{blog}j + a$). The j_o values for $PtSe_2$-Se were highest at 513 μAcm^{-2} followed by $PtSe_2$-SeU with a j_o of 239 μAcm^{-2}.

The obtained EIS spectra of the respective electro-catalysts are shown in Figure 3.6 (d) and a closer inspection of the spectrum (Figure 3.6 (e)) displays an incomplete semi-circle. Fitting the spectra on an electrochemical circuit (insert of Figure 3.6 (e)) resulted in R_{ct} values of 67 **Ω**, 520 **Ω**, and 996 **Ω** for $PtSe_2$-Se, $PtSe_2$-SeU, and $PtSe_2$-Na_2O_3Se, respectively. Although the HER follows the same pathway for all the catalysts, $PtSe_2$-Se has a much lower electron transfer resistance. Consequently, the HER activity of $PtSe_2$-Se is concluded to surpass that of $PtSe_2$-SeU, and $PtSe_2$-Na_2O_3Se and attributed to better electron transport properties of this catalyst.

But why does $PtSe_2$-Se perform better as an HER electrocatalyst? It is necessary to estimate the electrochemical surface area (ECSA) of the prepared $PtSe_2$ materials to elucidate the better performance of $PtSe_2$-Se relative to $PtSe_2$-SeU, and $PtSe_2$-Na_2O_3Se. The "Capacitance" method was employed to estimate the ECSA of the catalysts by running the CV scans at increasing scan rates (10 - 40 mVs^{-1}) in the non-Faradaic region of the complete CV scan (Figure 3.6 (f)-(h)). The current at each scan rate at half voltage of the spectrum was determined by subtracting the cathodic current from the anodic current ($i = i_a - i_c$) as shown in Figure 3.6 (i). The slope, which is the double-layer capacitance (C_{dl}) at the electrolyte-electrode interface was then determined from the

plot of scan rates vs current. ECSA is obtained from the quotient of C_{dl}, and C_s (40 µFcm^{-2}), as shown by Eqn. 3.8.[53] The obtained ECSA increases in the order $PtSe_2$-Na_2O_3Se (9.1 cm^2) < $PtSe_2$-SeU (14.6 cm^2) < $PtSe_2$-Se (90.7 cm^2). The high HER efficiency of $PtSe_2$-Se catalyst, based on the early onset, low Tafel slope, j_o, η_{-10}, and low R_{ct} can therefore be attributed to the high ECSA of this catalyst. This observation suggests that more electrochemically HER active sites are present in $PtSe_2$-Se than in $PtSe_2$-SeU, and $PtSe_2$-Na_2O_3Se. All the electrochemical performance parameters of $PtSe_2$-SeU, and $PtSe_2$-Na_2O_3Se are comparable.

ECSA = $\frac{C_{dl}}{Cs}$**……Eqn 3.8**

Where C_{dl} is the double-layer capacitance and C_s is the specific capacitance. C_{dl} is the slope of scan rate versus change in current plot, for scan rate versus current density plot, the slope is multiplied by electrode area.

Table 3.3: Electrochemical performance parameters obtained from LSV, EIS, and cyclic voltammetry studies for $PtSe_2$-Se, $PtSe_2$-SeU, and $PtSe_2$-Na_2O_3Se.

Catalyst	**E_{onset} /mV**	**η_{-10} /mV**	**Tafel Slope /mVdec^{-1}**	**j_o /µAcm^{-2}**	**R_{ct} /Ω**	**ECSA /mFcm^{-2}**
$PtSe_2$-Se	46	162	112	513	67	90.7
$PtSe_2$-SeU	91	255	135	239	520	14.6
$PtSe_2$- Na_2O_3Se	71	248	167	416	996	9.1

The stability of the electrodes upon extended exposure to the electrolyte is a vital parameter in electrochemical studies. The durability of $PtSe_2$-Se, $PtSe_2$-SeU, and $PtSe_2$-Na_2O_3Se was determined by running LSV before, and after 1000 CV cycles as shown in Figure 3.7 (a)-(c). The corresponding chronoamperometry (CA) curves are also shown. A drastic decline in the catalytic activity, evidenced by the onset potential moving more towards negative values, is observed for all electrocatalysts. The poor stability is further evidenced by the declining current density at onset potential as time is increased from 1 h to 24 h. The CA curves of the catalysts show that current density declines with time and does not stabilize even after extended periods.

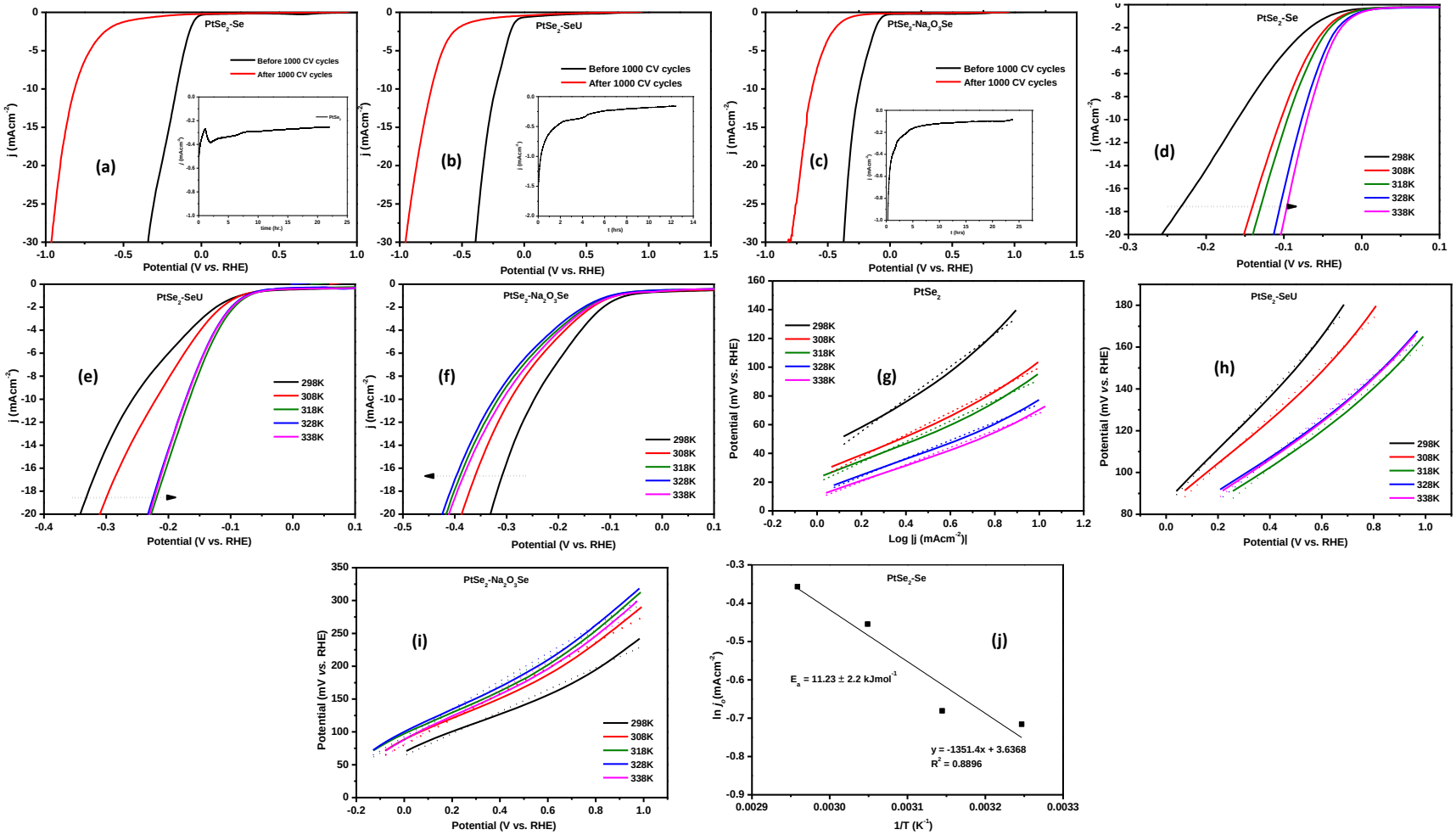

Figure 3.7: Stability evaluation of (a) $PtSe_2$-Se, (b) $PtSe_2$-SeU, and (c) $PtSe_2$-Na_2O_3Se by running LSV before and after 1000 CV cycles. Insert is corresponding stability by chronoamperometry studies. LSV curves at increasing temperature for (d) $PtSe_2$-Se, (e) $PtSe_2$-SeU, and (f) $PtSe_2$-Na_2O_3Se, and corresponding Tafel plots (g)-(i), respectively, and (j) Arrhenius plot for $PtSe_2$-Se electrocatalyst.

Table 3.4: Electrochemical parameters obtained from LSV curves of $PtSe_2$-Se, $PtSe_2$-SeU, and $PtSe_2$- Na_2O_3Se at increasing temperature.

Parameters	Electrocatalysts		
	$PtSe_2$-Se	$PtSe_2$-SeU	$PtSe_2$-Na_2O_3Se
298K			
E_{onset} /mV	46	91	71
η_{-10}/mV	162	255	248
b/mVdec^{-1}	113	135	167
J_o/μAcm^{-2}	513	239	416
308K			
E_{onset} /mV	24	85	91
η_{-10}/mV	103	217	296
b/mVdec^{-1}	78	118	195
J_o/μAcm^{-2}	519	209	388
318K			
E_{onset} /mV	21	72	98
η_{-10}/mV	98	165	319
b/mVdec^{-1}	72	100	208
J_o/μAcm^{-2}	535	240	375
328K			
E_{onset} /mV	18	72	105
η_{-10}/mV	77	174	325
b/mVdec^{-1}	63	99	212
J_o/μAcm^{-2}	656	205	367
338K			
E_{onset} /mV	13	72	92
η_{-10}/mV	73	172	312
b/mVdec^{-1}	60	99	207
J_o/μAcm^{-2}	723	216	406

The effect of temperature on the HER activity $PtSe_2$-Se, $PtSe_2$-SeU, and $PtSe_2$- Na_2O_3Se was examined by running LSV at 298 K, 308 K, 318 K, 328 K, and 338 K. The LSV curves obtained at increasing temperatures are shown in Figure 3.7 (d)-(f), and the corresponding

Tafel plots are shown in Figure 3.7 (g)-(i). The E_{onset}, η-10, b, and j_0 values of the catalysts obtained at different temperatures are summarised in Table 3.4. The E_{onset} and the η_{-10} of $PtSe_2$-Se are observed to improve linearly with increasing temperature. This relationship is explained by the Gibbs free energy equation, Eqn. 3.9.

$\Delta G = \Delta H - T\Delta S$……...……..Eqn 3.9

Where ΔG is the change in Gibbs free energy, ΔH is the enthalpy of the reaction, ΔS is entropy change, and T is temperature. The j_0 increased, and Tafel slopes decreased as the temperature was increased for $PtSe_2$-Se. The catalytic activity of colloidally prepared $PtSe_2$ from elemental selenium precursor improves with increasing electrolyte temperature. On the other hand, the opposite was observed for $PtSe_2$-SeU and $PtSe_2$-Na_2O_3Se. For these two catalysts, the catalytic activity decreases as the temperature is increased. The Arrhenius equation was therefore employed for $PtSe_2$-Se to calculate the minimum amount of energy needed to generate H_2 in a basic medium. The plot ln (j_o) versus $\frac{1}{T}$ shown in Figure 3.7 (j) was fitted to a straight line. The activation energy of the catalysts, E_a, was calculated by equating the slope to $\frac{-E_a}{R}$. The activation energy of $PtSe_2$-Se was found to be low at 11 $kJmol^{-1}$.

3.3.2 Optimizing $PtTe_2$ nanomaterials for efficient alkaline hydrogen evolution performance

3.3.2.1 Structure and Crystallite Size Determination of $PtTe_2$

XRD analysis was employed to determine the crystal phase, purity, and composition of the prepared Pt-Te nanomaterials. The XRD pattern of platinum telluride prepared from elemental Te precursor, shown in Figure 3.8 (a) (black) confirms the formation of moncheite $PtTe_2$ (PDF 01-072-2993) and crystalizes in the hexagonal P-3m1 space group. The XRD pattern of $PtTe_2$ has four predominant peaks at 2θ = 17.4°, 31.1°, 43.8°, and 45.3°, which are attributed to the (001), (011), (102) and (110) Millar indices of moncheite $PtTe_2$. The $PtTe_2$ XRD pattern has one unidentified peak at 32° (marked *) and could be attributed to traces of possible chloride salts that can also form in this reaction. On the other hand, the XRD pattern of platinum telluride prepared from $TeCl_4$ in Figure 3.8 (a) (red) shows the peaks attributed to $PtTe_2$ and 5 additional peaks. These additional peaks suggest that the sample has a high quantity of unreacted $TeCl_4$. As a result of attempting to reduce the unreacted $TeCl_4$, the molar ratio of $PtCl_4$ to $TeCl_4$ was reduced from 1:2 to 1:1 (Figure 3.8 (b)). Surprisingly, instead of forming $PtTe_2$, the XRD pattern matched PtTe instead, with the preidentified

impurities of $TeCl_4$. This suggests that in the colloidal synthesis of platinum telluride species, the Te precursor and its concentration influence the stoichiometry of Pt and Te in the product formed. The effect of changing the Te precursor to Na_2O_3Te was studied and revealed the formation of a mixed-phased platinum telluride material (Figure 3.8 (a), green). Na_2O_3Te resulted in the formation of a mixture of PtTe and $PtTe_2$, and this material was referred to as PtTe:$PtTe_2$ throughout this work. In addition to the $PtTe_2$ peaks, the peaks at 2θ = 13.6°, 26.8°, 27.8°, 29.1°, 31.9°, 56.9°, 75.6° and 85.8° were indexed to (001), (110), (002), (200), (111), (203), (131), and (330) PtTe (PDF 01-089-6166) Millar indices, respectively. PtTe crystallizes in the monoclinic C2/m space group. Additional peaks observed in this pattern (marked *) are assumed to occur from NaCl traces (XRD pattern of NaCl is shown in Figure S1 (b)).[56]

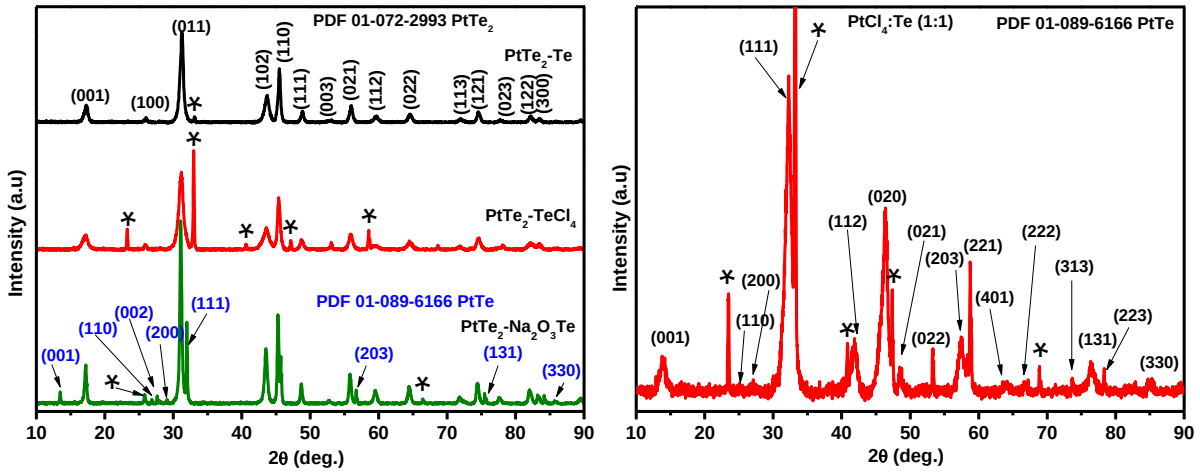

Figure 3.8: (a) XRD patterns showing the effect of varying Te precursor in the colloidal synthesis of platinum telluride using 1:2 molar ratio of platinum precursor to tellurium precursor, (b) XRD pattern of platinum telluride prepared from 1:1 molar ratio of $PtCl_4$ to $TeCl_4$.

The crystallite sizes of $PtTe_2$, PtTe and PtTe:$PtTe_2$ (summarised in Table 3.5) were estimated using the Scherrer equation shown in Eqn. 1. PtTe has the smallest crystallite size of 6.2 nm while the mixed phase PtTe:$PtTe_2$ has the largest crystallite size and a high standard deviation. This is because the crystallite sizes of PtTe and $PtTe_2$ structures in PtTe:$PtTe_2$ vary, making this material polydisperse. $PtTe_2$ crystallite size is calculated as 12.4 $\pm$ 1.3 nm.

Table 3.5: Crystallite size distribution of the Pt-Te catalysts.

Catalyst	Mean D_p (nm)	Std Dev (nm)
$PtTe_2$	12.4	1.3
PtTe	6.2	1.2
PtTe:$PtTe_2$	21.6	3.3

3.3.2.2 Surface Analysis of $PtTe_2$

^{1}H NMR was employed to determine the presence and the binding mode of the organic ligands used in the synthesis method to the surface of the platinum telluride materials. The ^{1}H NMR spectra of $PtTe_2$, PtTe, and PtTe:$PtTe_2$ reveal that although all the materials are prepared in a mixture of OLA and TOP, none of the materials bind to the two ligands simultaneously (Figure S2, S3, S4). $PtTe_2$ interacts with OLA whereas PtTe, and PtTe:$PtTe_2$ interact with TOP. OLA has two functional moieties, the alkene group, and the amine group, through which an interaction with the nanoparticles can develop. The ^{1}H NMR spectrum of pure OLA shown in Figure 3.9 (purple) reveals the presence of all types of hydrogen except the amino proton, as such, this proton was disregarded in determining the interaction of OLA to the platinum telluride materials. The comparison of the ^{1}H NMR spectra of $PtTe_2$ to that of OLA, and TOP, reveals that the $PtTe_2$ spectrum has peaks at all positions attributed to the protons in pure OLA (Figure 3.9, black). A closer examination of the peak shift and multiplicity change of the ^{1}H NMR OLA peaks in $PtTe_2$ indicated that alkyl protons (0.8 ppm, 1.3 ppm), vinylic protons (5.4 ppm), allylic proton (2.0 ppm) and C$\mathbf{H_2}$-NH_2 (2.7 ppm) are present in $PtTe_2$, most of which have retained their multiplicity. The vinylic proton signal position and multiplicity are not affected in the $PtTe_2$ spectra, suggesting that this functional group can be disregarded as the interaction point with $PtTe_2$ nanoparticles. The multiplicity of the C$\mathbf{H_2}$-NH_2 and alkyl proton (1.3 ppm) peaks have both changed from a triplet and a doublet to a singlet. The peak shift is also observed in the C$\mathbf{H_2}$-NH_2 peak, the proton closest to the amine group, suggesting that OLA interacts with $PtTe_2$ through the amine functionality. These $PtTe_2$ ^{1}H NMR also has three additional peaks at 0.1 and 1.6 ppm, attributed to unidentified impurities.

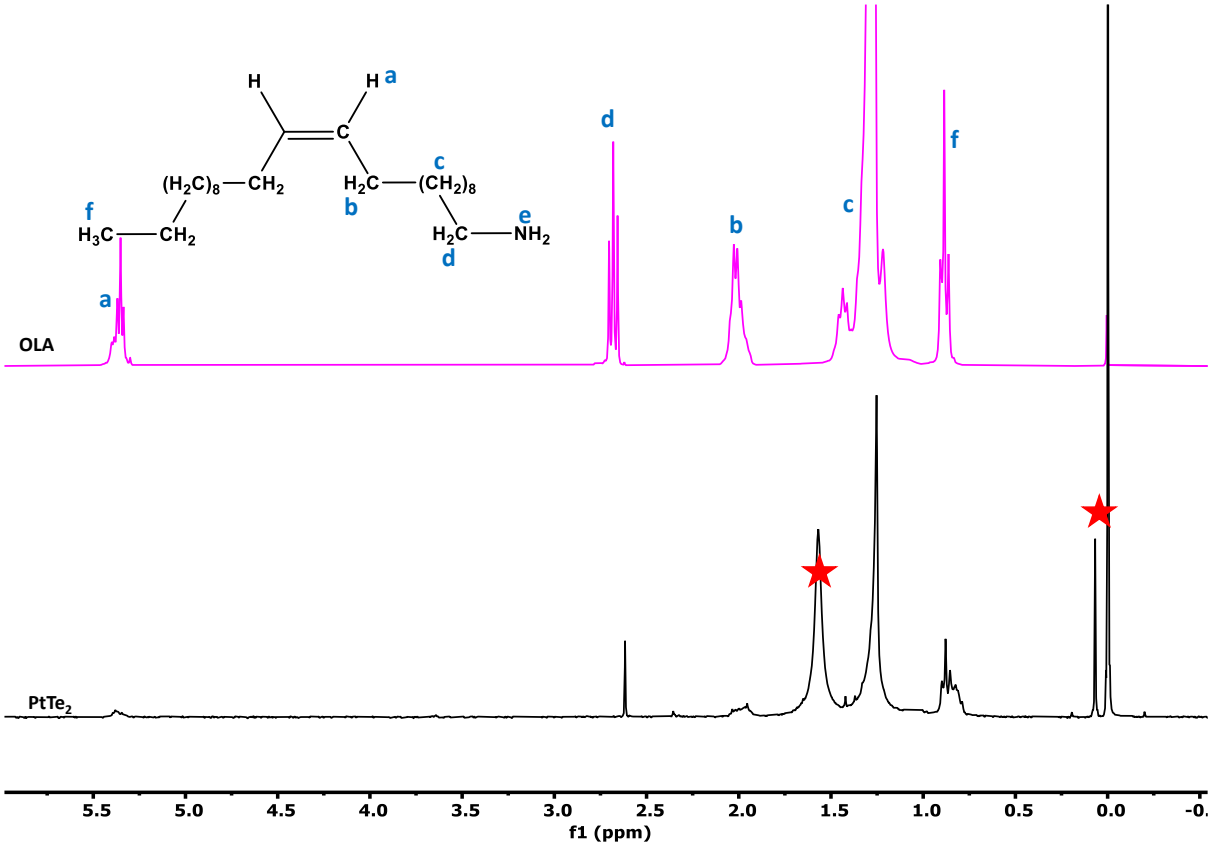

Figure 3.9: ^{1}H NMR spectra of free OLA (top), and OLA-capped $PtTe_2$ nanoparticles (bottom).

Conversely, the general comparison of the ^{1}H NMR spectrum of OLA and TOP to PtTe and PtTe:$PtTe_2$ ^{1}H spectra, reveals that these materials only interact with TOP. The ^{1}H NMR spectrum of free TOP acquired in d-DMSO is shown in Figure 3.10 (brown). Proton signals observed at 1.55 ppm, 1.33 ppm, 1.20 ppm, and 0.85 ppm were assigned to 1-methylene, 2-methylene, 3-methylene, and alkyl groups, respectively.[57] A close-up inspection of the ^{1}H NMR spectra of PtTe and PtTe:$PtTe_2$ shows that only three types of protons exist in these samples and are attributed to the alkyl group, 2-methylene, and 3 methylene groups (Figure 3.10, red and green, respectively). The disappearance of 1-methylene and the multiplicity change of 2-methylene from a multiplet to a singlet suggest that the TOP molecule interacts with the Pt-Te systems through the phosphine group. Phosphine in TOP has 1 lone pair of electrons, creating an electron cloud that can interact with a metal center.[58]

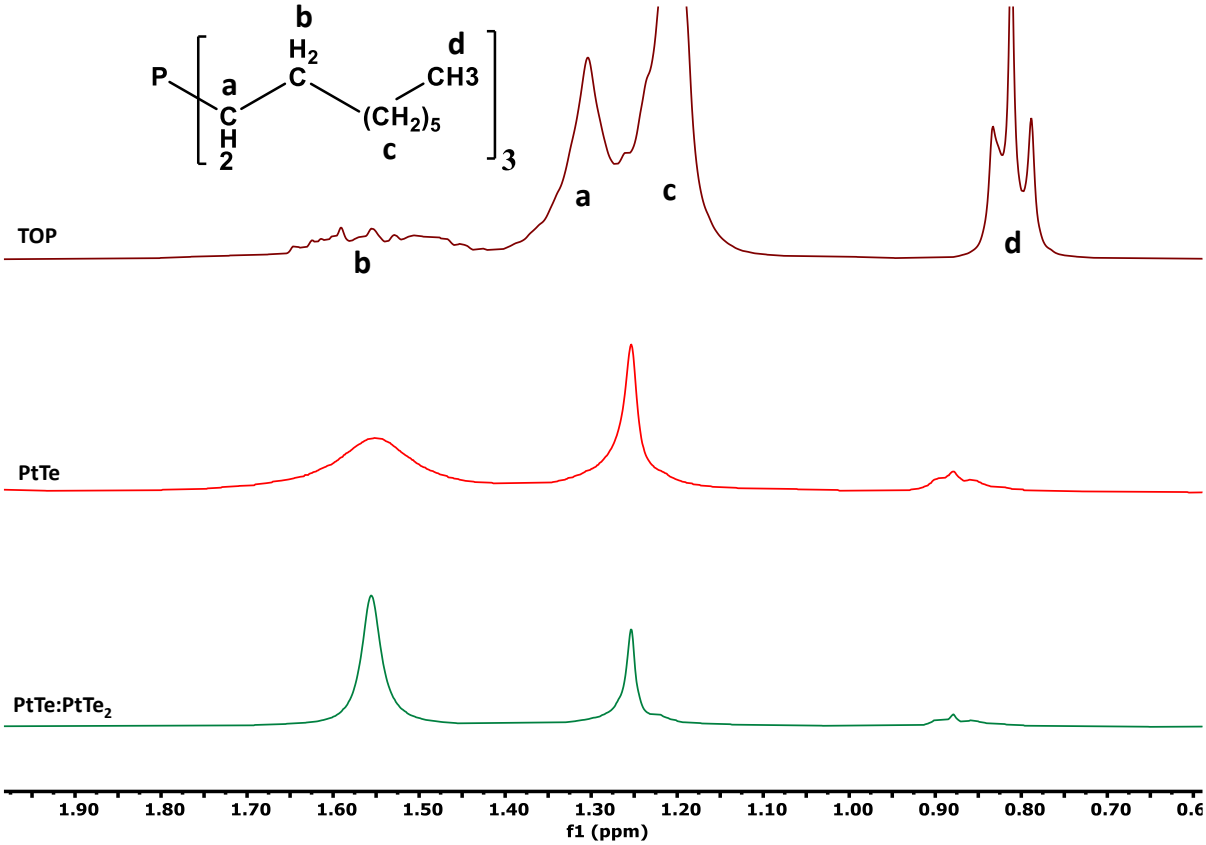

Figure 3.10: ^{1}H NMR spectra of pure TOP (brown) and TOP stabilized PtTe (red), and PtTe:$PtTe_2$ (green).

3.3.2.3 Morphology determination of $PtTe_2$

The morphology of platinum telluride materials prepared in a mixture of OLA and TOP at 320 °C was determined by TEM, shown in Figure 3.11. TEM micrographs of $PtTe_2$ (Figure 3.11 (a)) show irregular-sized, relatively larger, sheet-like materials clustered together. On the other hand, PtTe (Figure 3.11 (b)) shows the existence of rather small plate-like particles agglomerated together. The TEM micrograph of PtTe:$PtTe_2$ clearly shows the presence of two materials with distinct morphologies-first, the crumpled-up sheets and secondly, very dense conjugated polydisperse platelets (Figure 3.11 (c)). Based on the morphology of $PtTe_2$ obtained through synthesis using $PtCl_4$ and Te precursors, we can assume that the sheet-like structures are $PtTe_2$ nanoparticles whereas the agglomerates are PtTe nanostructures. This observation is consistent with the XRD results that clearly showed that using Na_2O_3Te as a Te precursor, results in the simultaneous formation of PtTe and $PtTe_2$.

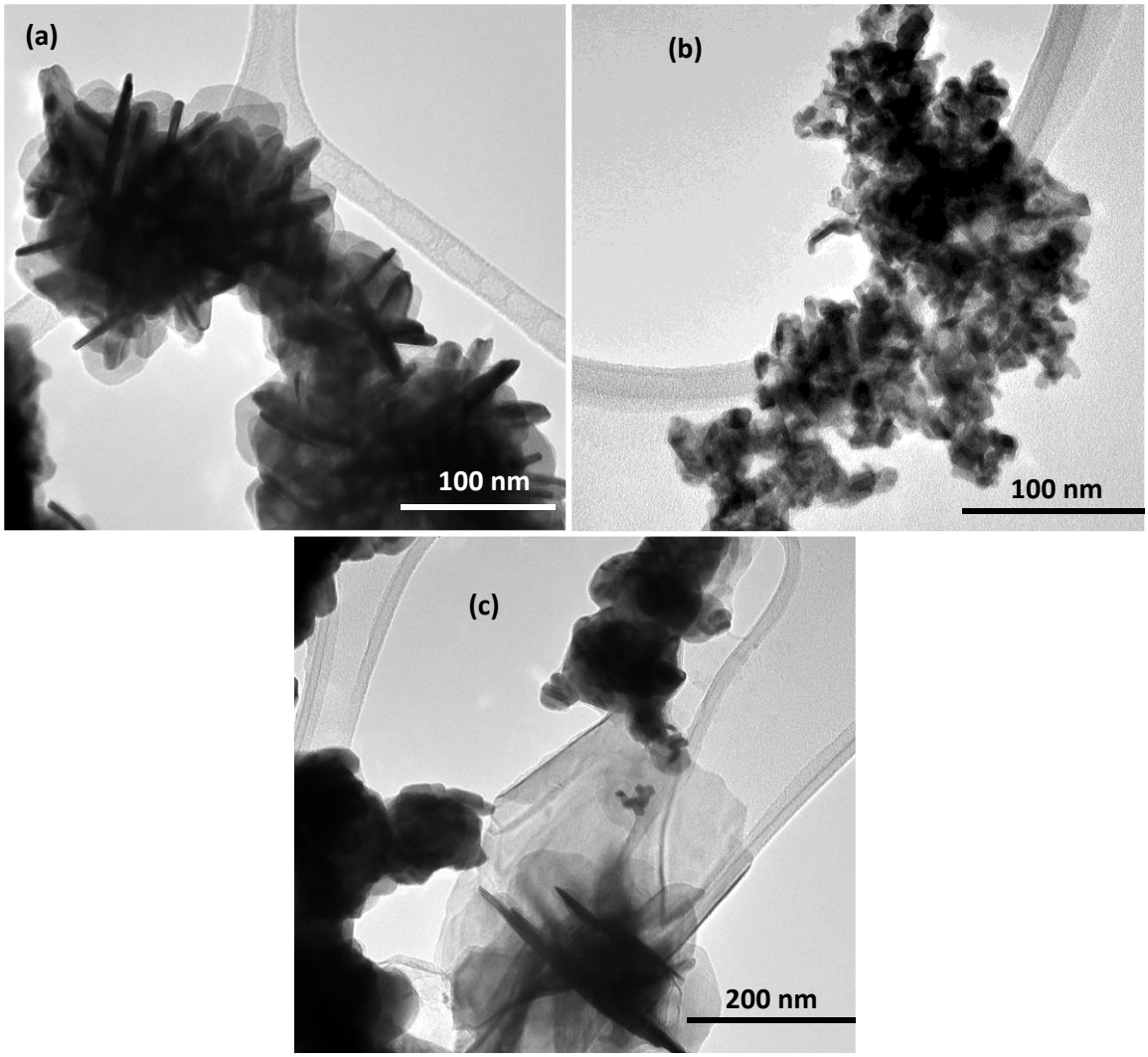

Figure 3.11: TEM images of (a) $PtTe_2$, (b) PtTe, and (c) PtTe:$PtTe_2$.

3.3.2.4 Elemental Composition Analysis of $PtTe_2$

XPS analysis was employed to identify the elements within the Pt-Te samples and the corresponding bonding configuration. The XPS survey spectra of $PtTe_2$, PtTe, and PtTe:$PtTe_2$ shown in Figure 3.12 (a)-(c) indicated the presence of Pt, Te, C, and O. In addition to these elements, Na and Cl were also detected in PtTe:$PtTe_2$ nanostructured material, following the observations in XRD and TGA. The survey spectrum of PtTe shows the presence of chloride ions, and this backs up the claim made in the XRD analysis that this material contains unreacted $TeCl_4$. Pt XPS high-resolution spectra of $PtTe_2$, PtTe, and PtTe are displayed in Figure 3.12 (d)-(f), respectively. For all the materials, Pt $4f_{5/2}$, and $4f_{7/2}$peaks are located at around 75 eV and 72 eV, respectively, with an energy difference of 3 eV, and are assigned to Pt^{2+}.[59] The two peak pairs at 74 eV and 71 eV are indicative of metallic Pt in the platinum telluride materials.[60] Of importance is the absence of Pt 4f peak pair at 77 eV and 72 eV,

which would otherwise indicate the presence of Pt^{4+}.[61,62] The exact peak positions (binding energy, BE), peak intensity (h_{max}), and full-width half maximum (FWHM) of Pt 4f of the $PtTe_2$, PtTe, and PtTe:$PtTe_2$ samples are summarized in Table 3.6. The FWHM of Pt^0 of $PtTe_2$ and PtTe:$PtTe_2$ are comparable while that of PtTe is quite low at 0.8 eV. On the other hand, the FWHM of Pt^{2+} is much higher in PtTe at 1.5 eV, while that of $PtTe_2$ and PtTe:$PtTe_2$ is 1.0 eV.

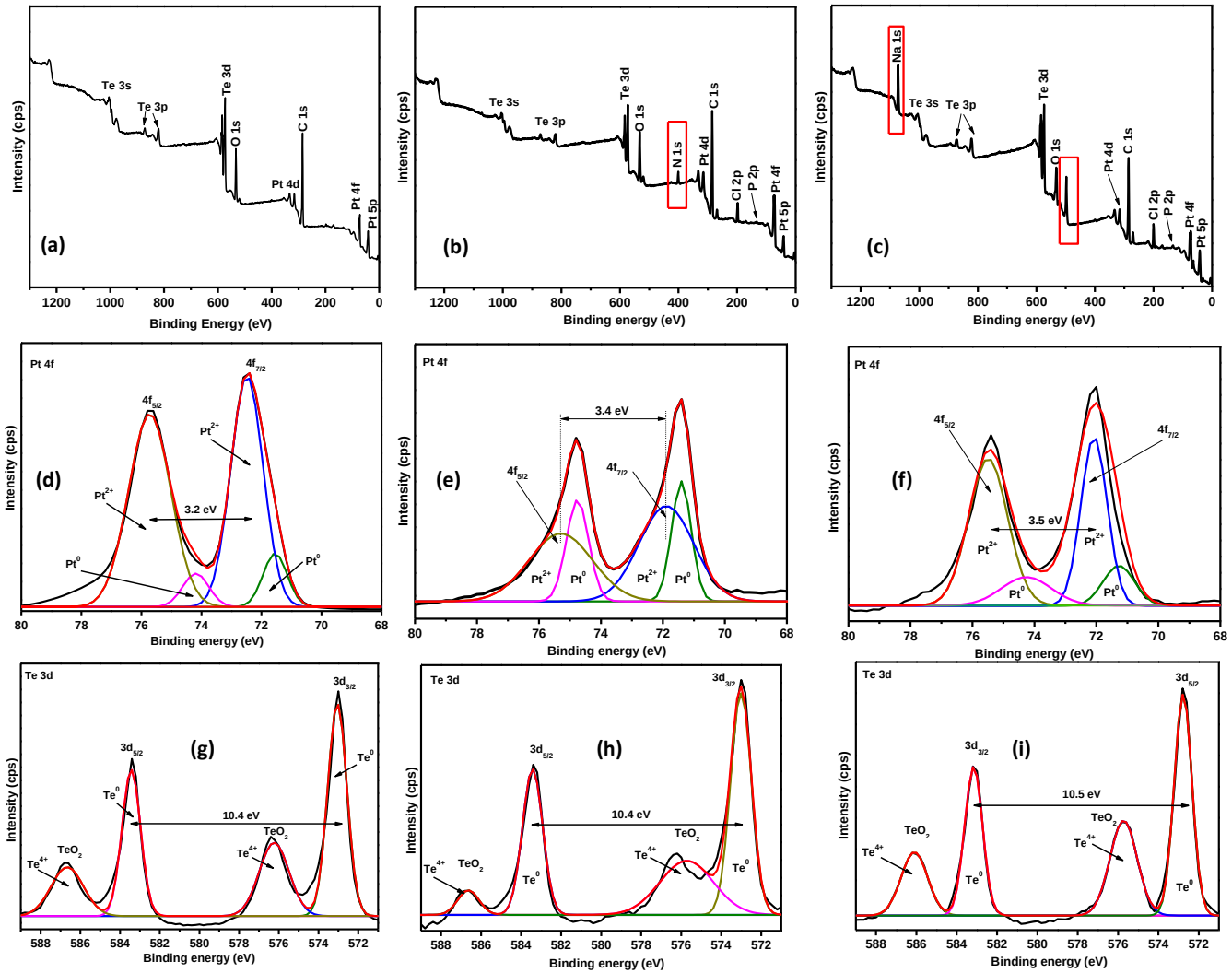

Figure 3.12: XPS survey spectra of (a) $PtTe_2$, (b) PtTe, and (c) PtTe:$PtTe_2$, high-resolution Pt spectra of (d) $PtTe_2$, (e) PtTe, and (f) PtTe:$PtTe_2$ and Te survey spectra of (g) $PtTe_2$, (h) PtTe, and (i) PtTe:$PtTe_2$.

The Te XPS high-resolution spectra of $PtTe_2$, PtTe, and PtTe:$PtTe_2$ are displayed in Figure 3.12 (g)-(i), respectively, and illustrate the presence of the Te^0 and Te^{4+} oxidation states.[63–65] Metallic Te is associated with the doublet peak at 583 eV and 572 eV, whereas the Te^{4+} is associated with the peaks at 586 eV and 576 eV. The peak positions, intensity and FWHM are indicated in Table 3.6. Based on the bonding configurations of previously reported transition metal dichalcogenides (MX_2, where M is the transition metal and X is the chalcogenide), the M usually exists as M^{4+} and the chalcogenide as X^{2-}.[6,66–68] This occurs because a simple ionic bonding of the elements explains bonding in these materials. However, bonding in platinum dichalcogenides, particularly platinum telluride, strays from the expected ionic bonding. In a study conducted by Dai et al. on the bonding patterns of platinum oxide and platinum dichalcogenides using electronic band structure calculations, they found that the Pt-Te bond is covalent.[16] This occurs because of the proximity in the energy of the Pt 5d orbitals to the chalcogen p orbitals.

Table 3.6: Summary of binding energy, peak intensity, and FWHM of the Pt-Te electrocatalysts.

Catalyst	**Peak Label**	**BE (eV)**	**h_{max}**	**FWHM (eV)**
$PtTe_2$	Pt^0 $4f_{7/2}$	71.8	1.3	1.1
	Pt^{2+} $4f_{5/2}$	72.6	2.6	1.0
	Te^0	573.1	16.8	1.2
	Te^{4+}	576.2	6.0	2.2
PtTe	Pt^0	71.4	6.8	0.8
	Pt^{2+}	72.2	3.1	1.5
	Te^0	573.0	12.5	1.2
	Te^{4+}	576.7	3.1	3.1
PtTe:$PtTe_2$	Pt^0	71.3	1.2	1.2
	Pt^{2+}	72.1	5.2	1.0
	Te^0	572.8	7.6	1.6
	Te^{4+}	575.7	17.7	1.0

3.3.2.5 Quantification of Capping Ligands in $PtTe_2$

TGA estimated the relative quantity of the capping ligands (OLA and TOP) and platinum telluride nanoparticles. The TGA/DTG profiles in Figure 3.13 depict the percentage weight change (black) and the derivative weight loss (red) of platinum telluride materials in the temperature range of 100 ℃ - 900 ℃. The derivative weight loss profile of both OLA and TOP are similar, with an initial mass loss of around 150 ℃ and complete sublimation at 300 ℃ (the TGA profile of TOP is shown in Figure S5).[43] As such, this analysis was purely used to estimate the quantity of the ligands rather than to identify the type of ligand present in the platinum telluride samples. $PtTe_2$ and PtTe:$PtTe_2$ profiles have three peaks, implying the degradation and therefore presence of three organic materials in these materials. PtTe derivative weight loss profile has one peak which indicates that only 1 organic compound is present within this sample. Figure 3.13 (a) shows a 20 % mass loss for $PtTe_2$ between 100 ℃ - 460 ℃, attributed to loss of moisture and organic capping ligand. The prepared $PtTe_2$ was assumed to contain 80 % $PtTe_2$. For PtTe, (Figure 3.13 (b), a 50 % mass loss is observed in the same temperature range as $PtTe_2$. TGA/DTG profile of PtTe:$PtTe_2$ in Figure 3.13 (c) shows rather different behaviour. All organic material degraded below 500 ℃ accounts for just 3 weight % of the sample. However, based on the weight % increase above 500 ℃ followed by a drastic decline in mass, it is postulated that this increase in mass is due to NaCl. Therefore, the quantity of PtTe:$PtTe_2$ cannot be estimated conclusively. Nonetheless, the amount of PtTe:$PtTe_2$ can be concluded to be below 60 %, based on the fact that at 900 ℃, the TGA curve is at 65 weight %. NaCl volatilizes above 800 ℃.[69]

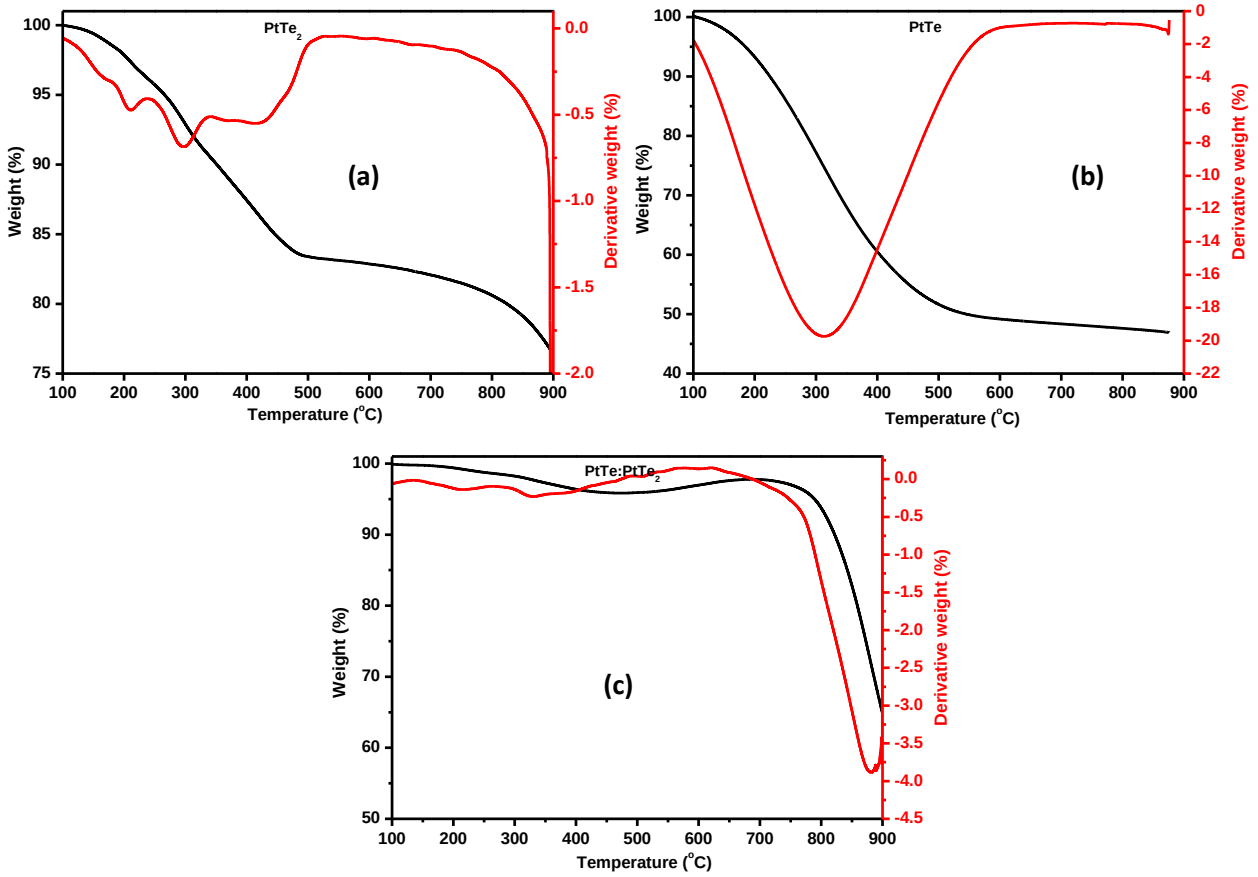

Figure 3.13: The TGA (black) and the corresponding DTG curves of (a) $PtTe_2$, (b) PtTe, and (c) PtTe:$PtTe_2$.

3.3.2.6 Hydrogen evolution reaction of $PtTe_2$

The electrochemical HER activity of $PtTe_2$, PtTe and PtTe:$PtTe_2$ catalysts was evaluated by running electrochemical studies in 1 M KOH using a 3-electrode cell configuration. The parameters are summarised in Table 3.7. The polarization curve depicted in Figure 3.14 (a) shows the change in current density (*j*) with increasing voltage (V). The E_{onset}, the point at which *j* increases from zero, taken at -1 $mAcm^{-2}$, is a parameter that is related to the catalyst activity. The smaller this value is, the more catalytic the catalyst is.[70] $PtTe_2$ has the earliest E_{onset} of 29 mV, followed by PtTe at 71 mV. The PtTe:$PtTe_2$ has the largest E_{onset} of 101 mV. The potential at -10 $mAcm^{-2}$ is another benchmark parameter that can be used universally to compare the performance of different catalyst materials toward HER.[71,72] The least amount of energy (107 mV) is required to produce a current of -10 $mAcm^{-2}$ on $PtTe_2$, followed by PtTe and PtTe:$PtTe_2$ requiring 166 and 187 mV, respectively, to produce the same current. $PtTe_2$ sheets have portrayed the highest catalytic activity. Following this, the polarization curves were then modelled to a Tafel equation to deduce the kinetic parameters of the catalysts (Figure 3.14 (b)). $PtTe_2$ has a Tafel slope of 79 $mVdec^{-1}$, and

the smaller value indicates a fast charge transfer of HER on the catalyst surface. A slower charge transfer HER on PtTe and PtTe:$PtTe_2$ is observed courtesy of high Tafel slopes of 166 $mVdec^{-1}$ and 187 $mVdec^{-1}$, respectively. Therefore, it can be concluded that the catalytic activity of $PtTe_2$ surpasses that of PtTe and PtTe:$PtTe_2$. The HER mechanism on $PtTe_2$ can thus be assumed to follow the Volmer-Heyvosky mechanism.[73,74] The deduced HER mechanism on $PtTe_2$ based on the Tafel slope values is different from the $PtTe_2$ from PtTe and PtTe:$PtTe_2$ HER mechanisms.

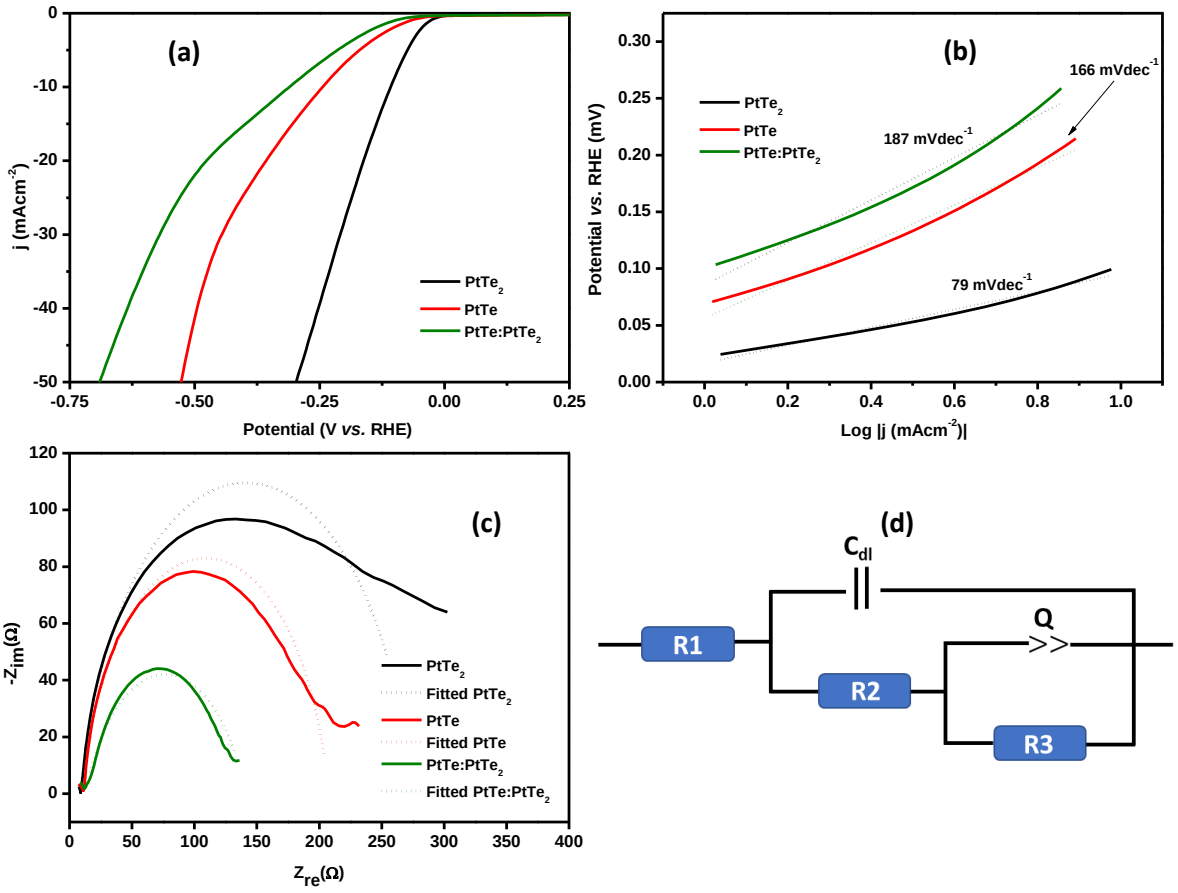

Figure 3.14: Comparison of (a) HER polarization curve, (b) Tafel plots, (c) experimental and fitted Nyquist plot of $PtTe_2$, PtTe, and PtTe:$PtTe_2$, and (d) is the electrochemical cell model that was fitted to the EIS data.

The high Tafel slopes obtained for PtTe and PtTe:$PtTe_2$ have been observed previously for both acid-based and alkaline HER.[50,75,76] It is assumed that for such a reaction, there is a supplementary reaction step that involves the absorption of hydrogen within the catalyst material. The relatively high catalytic activity of $PtTe_2$ compared to PtTe and PtTe:$PtTe_2$ can be explained by the TGA, which indicated that of the three catalysts, $PtTe_2$ has the least amount of additional capping agent and the highest content of $PtTe_2$.

The electrical conductivity of the electrodes prepared from $PtTe_2$, PtTe, and PtTe:$PtTe_2$ catalysts was evaluated by EIS measurements at onset potential. The corresponding EIS plots are shown in Figure 3.14 (c). The EIS plots were then fitted to an electrochemical cell shown in Figure 3.14 (d) and the R_{ct} values were deduced and summarized in Table 3.7 for all catalysts. Although $PtTe_2$ exhibits the highest catalytic activity and fast HER kinetics, it has the largest R_{ct} value while the mixed phase PtTe:$PtTe_2$ has the smallest R_{ct}. This means that there is less resistance to electron transport on PtTe and PtTe:$PtTe_2$ relative to $PtTe_2$.

Table 3.7: HER performance indicators of the prepared platinum telluride catalysts

Catalyst	**η_{onset}/ mV**	**η/mV**	***b*/mVdec^{-1}**	**R_{ct}/Ω**	**ECSA/cm^2**
$PtTe_2$	29	107	79	268	463
PtTe	70	310	166	196	44
PtTe:$PtTe_2$	101	243	187	128	64

Another parameter that can be scrutinized to better understand the electrocatalytic behaviour of the catalyst materials is the electrochemical surface area (ECSA). The current response at different scan rates is determined for the different catalysts, shown in Figure 3.15 (a)-(c), from which Δj is determined and plotted against the scan rate (Figure 3.15 (d)). The ECSA is then estimated from the quotient of C_{dl} and specific capacitance, C_s, assumed to be 40 $\mu F\ cm^{-2} per\ cm$ ECSA.[77,78] The calculated ECSA values are summarized in Table 3.7. $PtTe_2$ has an ECSA of 464 cm^2, almost 8 times that of both PtTe and PtTe:$PtTe_2$. This further corroborates why $PtTe_2$ has a higher overall catalytic activity towards HER in an alkaline medium.

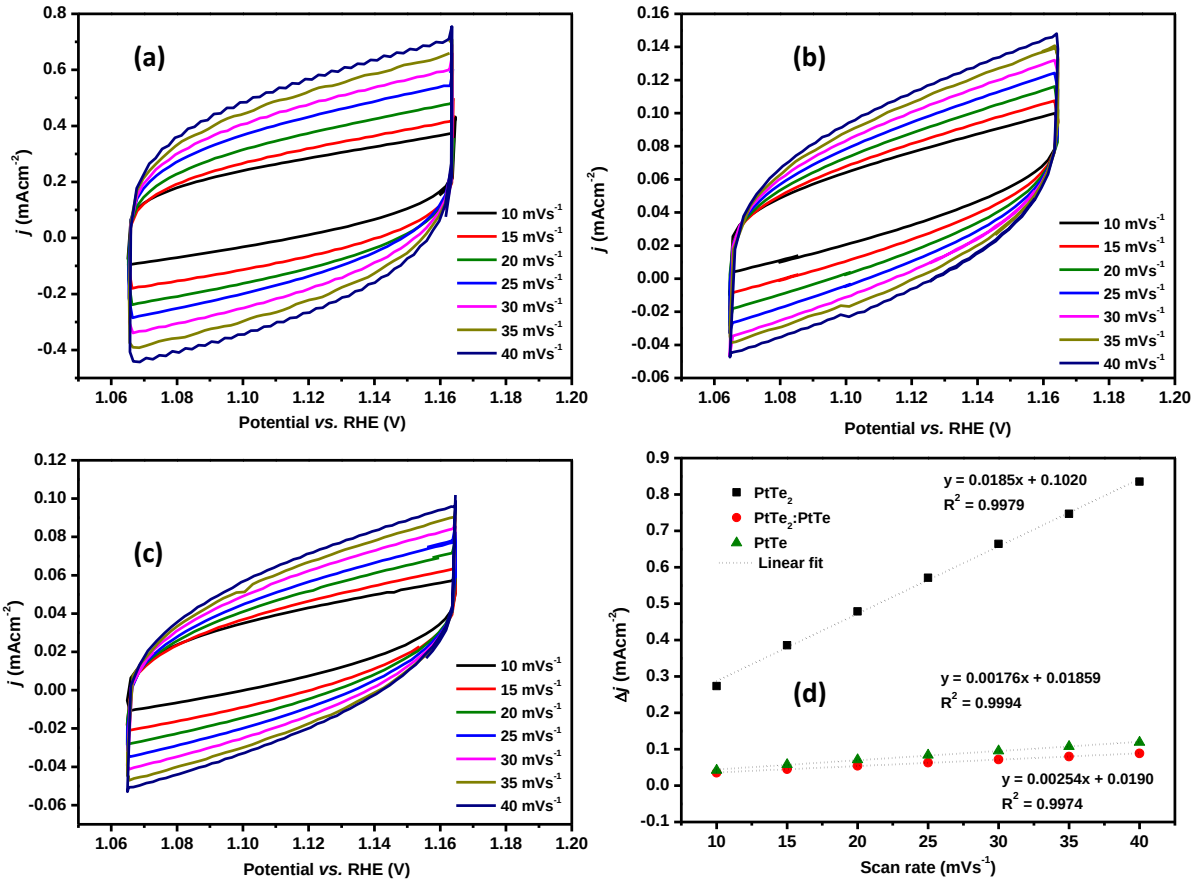

Figure 3.15: Non-Faradeic CV curves of (a) $PtTe_2$, (b) PtTe, and (c) PtTe:$PtTe_2$ at increasing scan rates and (d) the double layer capacitance measurements for ECSA determination.

3.3.3 Comparative performance analysis of optimized $PtSe_2$ and $PtTe_2$ nanomaterials for alkaline hydrogen evolution reaction

$PtSe_2$ prepared from elemental Se demonstrated superior alkaline HER activity. On the other hand, $PtTe_2$, produced from colloidal synthesis of $PtCl_4$ and Te, displayed better HER activity than PtTe and PtTe:$PtTe_2$. The electrochemical HER properties of these catalysts must be compared to a commercial Pt catalyst to determine which PtX_2 is a more suitable HER catalyst. Figure 3.16 (a) depicts the polarization curves $PtSe_2$ and $PtTe_2$. The graph clearly illustrates that $PtTe_2$ has a comparable HER activity to the commercial 40-weight % Pt/C, whereas $PtSe_2$ has a low HER activity in the same electrolyte. These results show a similar trend to previous studies carried out in an acidic medium on the same catalyst materials.[79,80] Chia et al. found out that $PtTe_2$ prepared by chemical vapor deposition of chalcogen on the Pt surface is a better-performing HER catalyst than $PtSe_2$.[80] The observed E_{onset} and potential at -10 mV/s (η_{-10}) of $PtTe_2$ in KOH is extensively lower than that of both $PtSe_2$ and $PtTe_2$ in an acidic medium, suggesting that $PtTe_2$ is a better catalyst for HER in a basic medium. HER in the basic medium is relatively harder to achieve as opposed to

acidic medium HER since for H_2 to be produced in KOH, water needs to be broken down into hydroxyl and hydroxide ions. This process is more energy-intensive than the combination of hydroxyl ions to produce hydrogen gas in an acidic medium.[81]

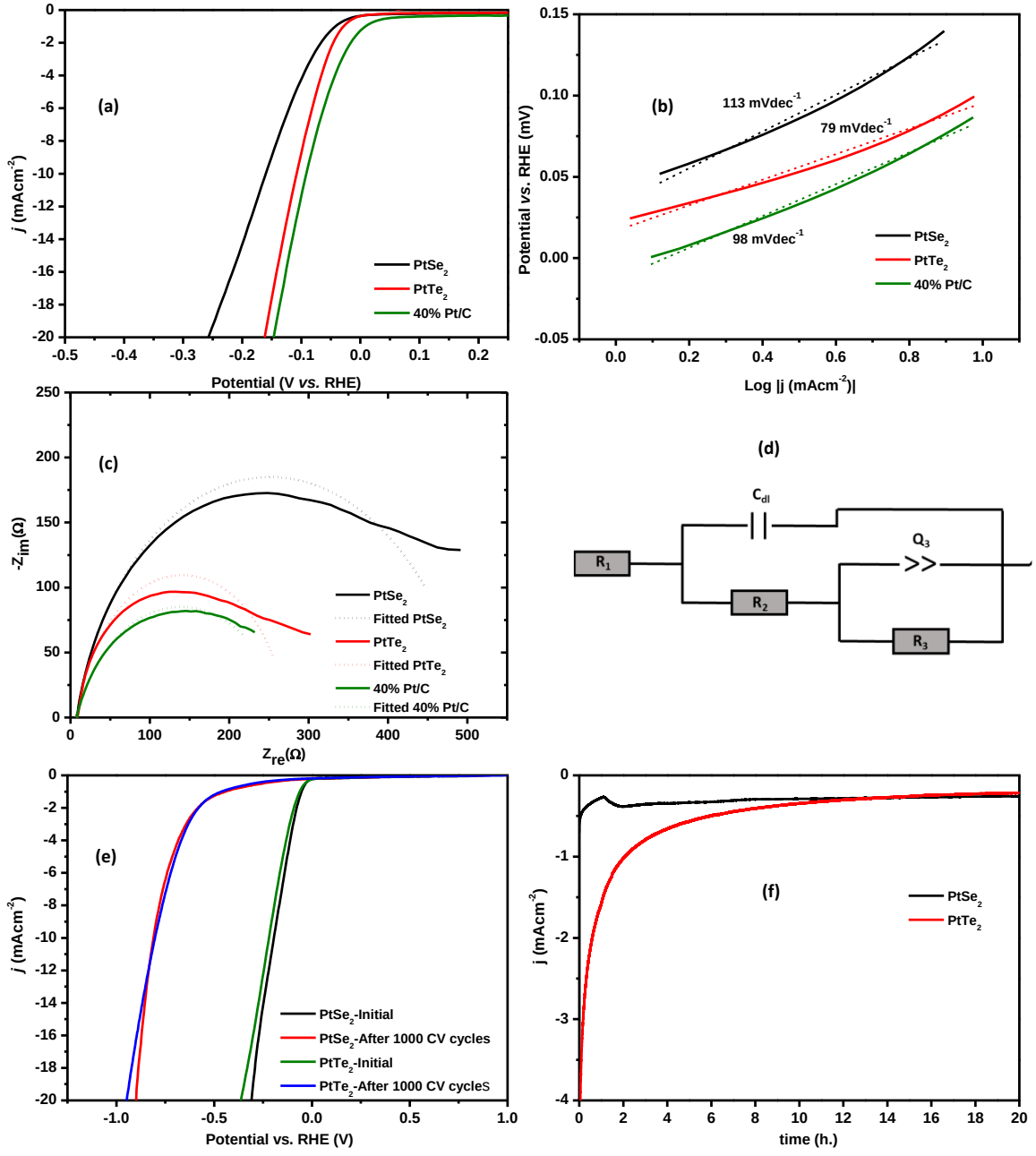

Figure 3.16: Comparison of (a) HER polarization curve, (b) Tafel plots, (c) experimental and fitted Nyquist plots of $PtSe_2$ and $PtTe_2$ to 40 weight % commercial Pt/C catalyst, (d) is the electrochemical cell model that was fitted to the EIS data, and (e) is the LSV curves of $PtSe_2$ and $PtTe_2$ after a stabilized CV cycle and after 1000 CV cycles (CV cycles obtained between -1 V and 0.5 V at 5 mVs^{-1}) and (f) is the CA curves obtained at onset potentials of the respective catalysts.

The production of hydrogen from either acidic or basic electrolytes is a three-step process that involves hydrogen adsorption on the catalyst surface (Volmer step), followed by either electrochemical (Heyrovsky step) or chemical desorption of hydrogen gas (Tafel step). Generally, HER on a catalytic surface occurs through the Volmer-Heyrovsky or Volmer-Tafel mechanisms, with the Heyrovsky obtained if the Tafel slope is substantial.[50] It can then be assumed that HER on $PtSe_2$, $PtTe_2$, and Pt/C follows the Volmer-Heyrovsky mechanism, shown in Figure 3.17. A lower Tafel slope is also indicative of fast reaction kinetics and a low energy barrier. Figure 3.16 (b) shows the comparison of Tafel plots of the catalysts. The relatively low Tafel slope (79 $mVdec^{-1}$) of $PtTe_2$ suggests that $PtTe_2$ displays faster HER kinetics compared to $PtSe_2$ (113 $mVdec^{-1}$). The Tafel plot can then be used to extrapolate the minimum current that can be produced by the catalysts when the potential is zero. This parameter is the j_o and is used to ascertain the catalytic activity of the catalysts. The higher the j_o value is, the more catalytic the electrode material is. $PtSe_2$ shows a higher j_o of 513 μAcm^{-2}, while j_o of $PtTe_2$ is 378 μAcm^{-2}.

The EIS spectra shown in Figure 3.16 (c) were fitted to an electrochemical cell depicted in Figure 3.16 (d). R_{ct} values obtained from this fit indicate the resistance of the electrode surface to electron flow, that is R_{ct} signifies how conductive the electrode is. The R_{ct} values for $PtSe_2$, $PtTe_2$, and Pt/C were found to be 500 Ω, 269 Ω, and 266 Ω, respectively. This suggests that charge transfer occurs faster on both $PtTe_2$ and 40 % Pt/C than on $PtSe_2$. $PtTe_2$ is deemed to exhibit metallic properties while $PtSe_2$ shows semi-metallic properties. The conductivity of $PtTe_2$, by its nature, is expected to surpass that of $PtSe_2$.

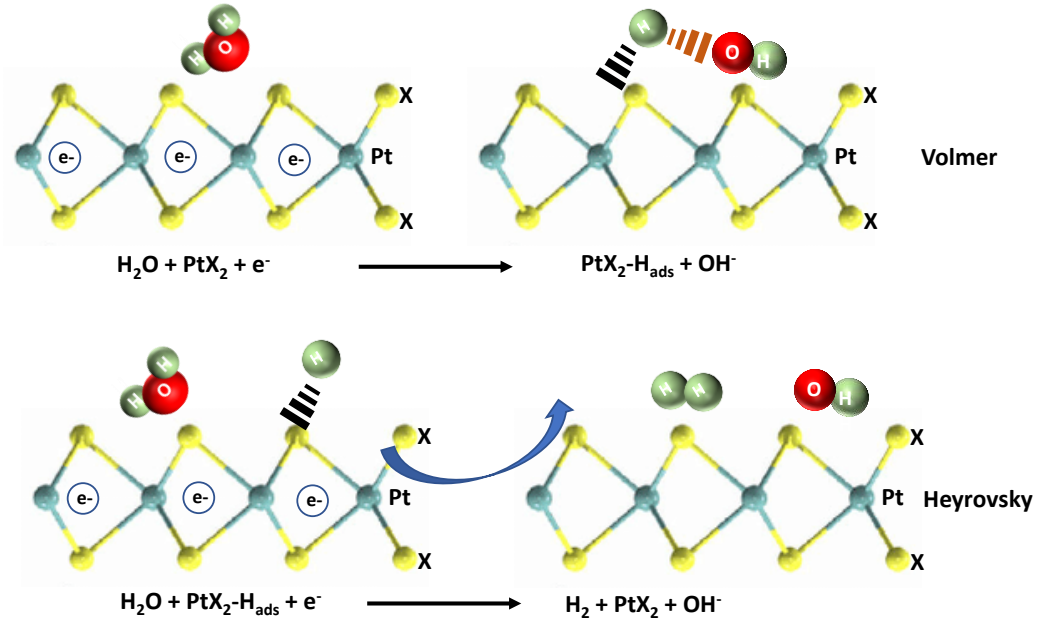

Figure 3.17: The Volmer-Heyrovsky HER on Pt dichalcogenides in KOH

The prolonged stability of the electrode material was determined by running LSV before and after 1000 CV scans (Figure 3.16 (e)). Although the catalysts show a high catalytic activity in the basic medium, their stability is quite poor. This is evidenced by an increased η_{-10} and E_{onset} after 1000 CV scans, indicating that the catalytic activity of the catalysts reduces after prolonged exposure to the electrolyte. CA studies (Figure 3.16 (f)), where the current response was measured over 20 hours show a very low current response, less than 0.5 $mAcm^{-2}$, for both catalysts. The current response for $PtSe_2$ only stabilises after 2 h while the current response for $PtTe_2$ declines gradually over the 20 h period. The HER performance parameters of the catalysts prepared in this study and those of previously evaluated 2D TMDs are summarized in Table 3.8. Generally, $PtSe_2$ and $PtTe_2$ show a small E_{onset} and $\eta_{-10,}$ and comparable Tafel slope to the other catalysts. The R_{ct} values of $PtSe_2$ and $PtTe_2$ are relatively high. This suggests that electron transfer between the external circuit and the KOH electrolyte is harder to achieve when using $PtSe_2$ and $PtTe_2$.

HER	Electrolyte	E_{onset}	$\eta_{-10\ mAcm^{-2}}$	B	J_0	R_{ct}/ Ω	Reference

Catalyst		/ mV	/mV	/mVdec^{-1}	/mAcm^{-2}		
$PtSe_2$	1M KOH	44	161	113 ± 4	0.513	500	This work
$PtTe_2$	1M KOH	28	108	78 ± 3	0.378	269	This work
40 % Pt/C	1M KOH	7	93	98 ± 2	1.364	266	This work
$MoSe_2$	1M KOH	~290	331	137	-	~60	[34]
MoS_2	1M KOH	350	450	105	-	14	[35]
Ni_3S_2	1M KOH	-	171	132	-	10	[36]

Table 3.8: Comparison of performance indicators for HER on various catalysts.

The ECSA of $PtSe_2$ and $PtTe_2$ electrocatalysts was compared as shown in Figure 3.18. The ECSA of $PtTe_2$ was then calculated to be 462.5, three times higher than that of $PtSe_2$ (90.7). This suggests that $PtTe_2$ has a high number of HER active sites where the water molecules are dissociated to produce H_2, rendering this material more catalytically active than $PtSe_2$. The contribution of ECSA of the catalyst on the HER performance was eliminated by normalizing the LSV curves to ECSA using Eqn 3.10, as shown in Figure 3.18 (d).[82] Interestingly, $PtSe_2$ showed a better intrinsic HER performance of 41 mV at 0.01 mAcm^{-2}, almost half that of $PtTe_2$ (78 mV). This could suggest that, although $PtTe_2$ has a higher surface area, the electronic structure and morphology of the catalysts influence the HER performance.[83]

$$J \text{ (ECSA normalized)} = \frac{j}{ECSA} = j \times \frac{C_s}{C_{dl}} \quad \text{.....Eqn 3.10}$$

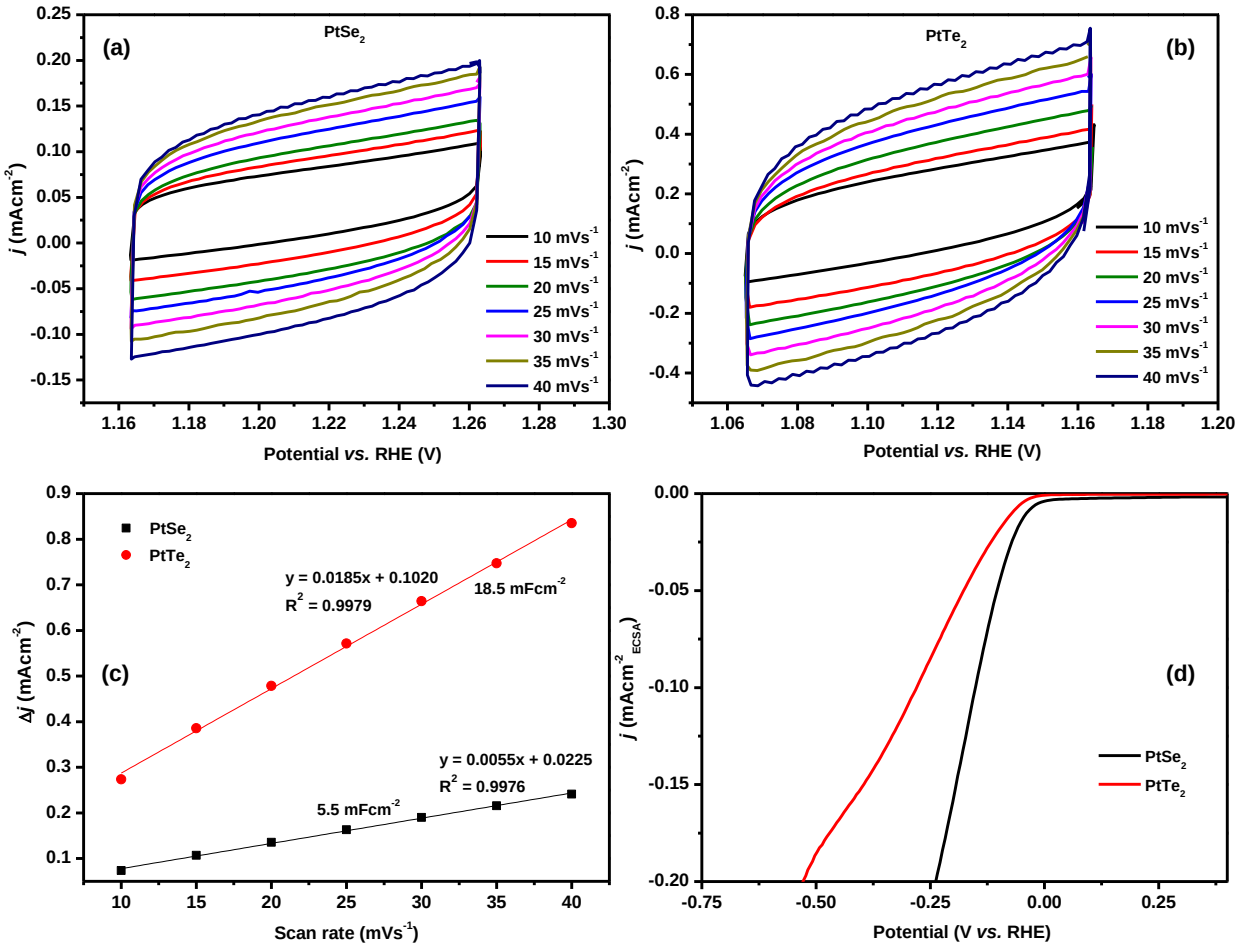

Figure 3.18: Non-Faradaic CV curves of (a) $PtSe_2$, (b) $PtTe_2$ at increasing scan rates, (c) the double layer capacitance measurements, and (d) the LSV curves of $PtSe_2$ and $PtTe_2$ normalized to ECSA.

To better understand the catalyst surfaces and their role in the HER, we studied the morphology of the working electrode. The topology images in Figure 3.19 (a) and (b) indicate the presence of clustered grains with differing heights and lengths. The surface roughness, average roughness divided by root mean square,[84] ($\frac{R_a}{R_q}$) of $PtSe_2$ was calculated as 0.733 while that of $PtTe_2$ was 0.816. This signifies that the surface of $PtTe_2$ electrode was rougher than $PtSe_2$, potentially introducing more grooves that increase the surface area. TEM image analysis of the prepared catalysts suggests that $PtSe_2$ (prepared from Se) is relatively smaller than $PtTe_2$. Generally, larger nanoparticles (or thicker films) show greater R_a as opposed to smaller particles (or thinner films).[85,86]

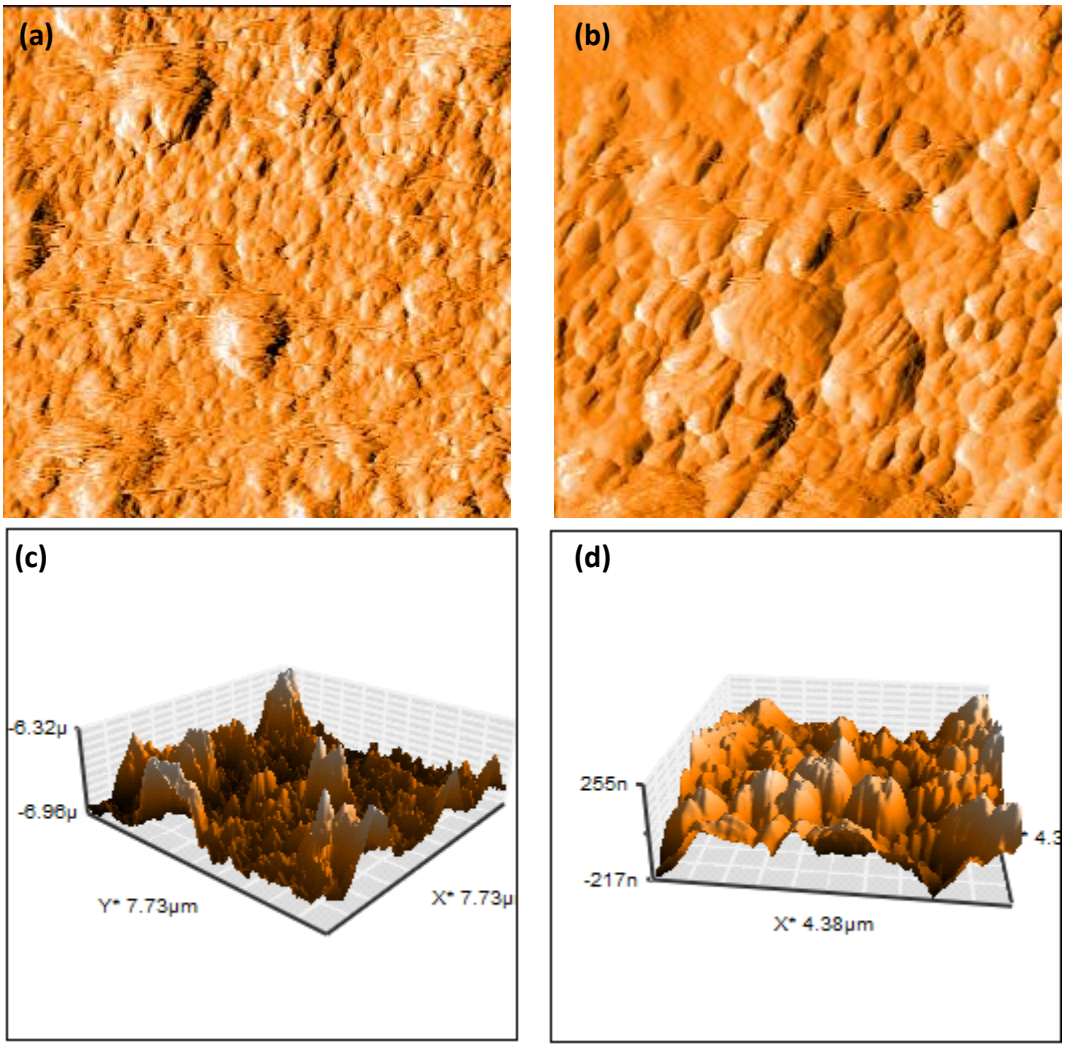

Catalyst/AFM properties	R_a (nm)	R_q (nm)	R_a/R_q
$PtSe_2$	63.308	93.266	0.733
$PtTe_2$	64.252	78.733	0.816

Figure 3.19: AFM surface topology images of (a) $PtSe_2$ and (b) $PtTe_2$ inks and the height profile of (c) $PtSe_2$ and (d) $PtTe_2$.

The HER activity of electrocatalysts is reported to change with the electrolyte temperature. To study this effect, LSV polarization curves of both $PtSe_2$ and $PtTe_2$ were obtained at 298 K, 308 K, 318 K, 328 K, and 338 K. The corresponding Tafel slopes from the LSV curves were also obtained. The onset potential decreases from 45.0 mV at 298 K to 11.5 mV at 338 K, while the η_{-10} changes from 161.2 mV to 70.3 mV at the same temperatures for $PtSe_2$ (Figure 3.20 (a)). Likewise, E_{onset} and the η_{-10} of $PtTe_2$ decreased from 29.9 mV and 107.4 mV, at 298 K to 21.9 mV and 89.8 mV at 338 K, respectively (Figure 3.20 (b)), Figure 3.20 (c) & (d) shows the Tafel slopes at the respective temperatures. The slope for both the catalysts is reduced upon increasing the electrolyte temperature, this suggests faster HER kinetics at elevated temperatures. The Tafel plots were then

linearized to get $J_{o.s}$. This is the current produced when there is no energy input in the system. The minimum energy required to facilitate the HER on the catalysts, referred to as activation energy (E_a) can then be obtained from the plot of the inverse of temperature against ln j_o (Figure 3.20 (e)) deduced from the Arrhenius equation shown in Eqn. 3.11. The slope of this plot is then related to $\frac{E_a}{R}$. From this, the E_a values obtained for $PtSe_2$ was 11.2 $kJmol^{-1}$, with that of $PtTe_2$ slightly lower at 10.3 $kJmol^{-1}$. Both these values are lower than E_a values reported by various authors.[8,87] Lower E_a values signify faster reaction initiation, enhanced reaction efficiency, improved kinetics, and reduced overpotential. This further suggests that the energy required for the HER on PtX_2 catalysts is low, as such, hydrogen is easily produced from these catalysts' surfaces.

$$\boldsymbol{k = Ae^{\frac{-E_a}{RT}}} \quad \textbf{.....Eqn 3.11}$$

where k is the kinetic rate constant, E_a the activation energy, A is the collision frequency factor, R is the gas rate constant and T is the temperature in Kelvin.

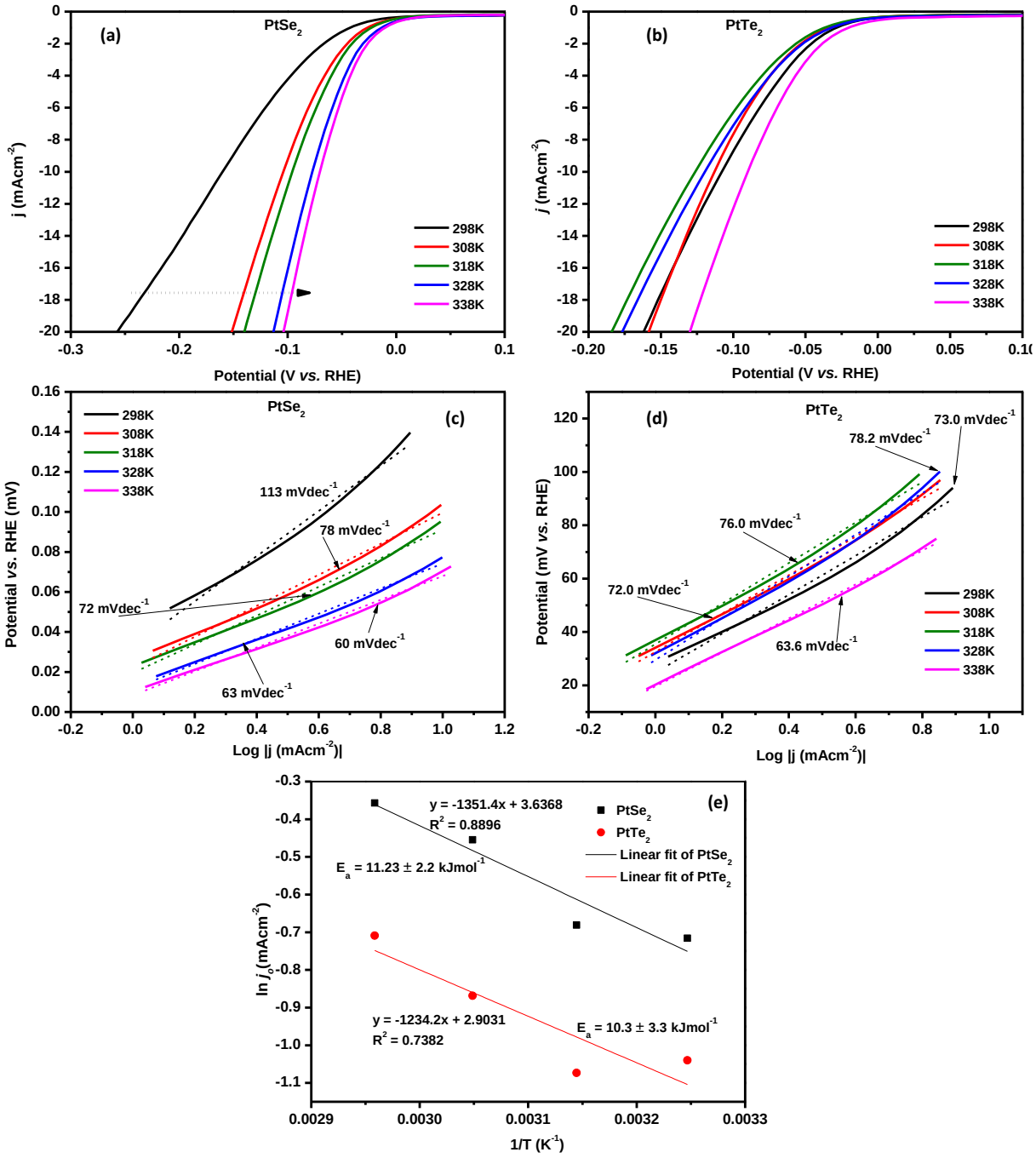

Figure 3.20: LSV curves of (a) $PtSe_2$ and (b) $PtTe_2$ obtained at increasing electrolyte temperature, corresponding Tafel plots of (c) $PtSe_2$ and (d) $PtTe_2$ and, (e) Arrhenius plots for $PtSe_2$ and $PtTe_2$.

The exact amount of Pt in the catalysts and the actual Pt loading was determined by inductively coupled plasma-optical emission spectroscopy (ICP-OES) and the results are summarised in Table 3.9. The mass percent concentration of Pt in $PtSe_2$ was determined to be 2.55 % and slightly lower at 2.23 % in the $PtTe_2$ sample. Therefore, the Pt loading on the $PtSe_2$-coated GC was 33.5 µg/cm^2 and 27.8 µg/cm^2 on $PtTe_2$-coated GC electrodes. Despite having low Pt loading, $PtTe_2$ displays a better alkaline HER activity than $PtSe_2$. The carbon black loading, which was used to improve the conductivity of the catalysts, was calculated, and obtained as 24 µg/cm^2.

Table 3.9: ICP-OES mass percentage concentration of the catalysts and corresponding Pt loading.

Catalyst	Mass percent concentration (% m/m)			Pt loading ($\mu g/cm^2$)
	Pt	Se	Te	
$PtSe_2$	2.55	2.36	-	33.54
$PtTe_2$	2.23	-	2.85	27.84

3.4 Conclusions

$PtSe_2$ was successfully synthesized by hot injection colloidal synthesis using $Pt(AcAc)_2$ as a platinum precursor, and elemental Se, SeU, and Na_2O_3Se as selenium precursors. Based on the XRD pattern and Raman spectroscopy analysis, $PtSe_2$-SeU is more amorphous (has the smallest crystallite diameter) whereas $PtSe_2$-Se and PtSe-Na_2O_3Se are crystalline. Of the three $PtSe_2$ catalysts, $PtSe_2$-Se exhibits a high catalytic activity as evidenced by small E_{onset} and η_{-10}, high exchange current density, and small R_{ct}. This is attributed to the relatively high ECSA of $PtSe_2$-Se. The effect of varying Te precursor in the colloidal synthesis of platinum telluride materials carried out at 320 ℃ in a mixture of OLA and TOP, resulted in the formation of PtTe, $PtTe_2$, and mixed-phase PtTe:$PtTe_2$. TGA results revealed that PtTe:$PtTe_2$ has the least amount of capping ligand per unit mass (5 %) followed by $PtTe_2$ with 20 % and PtTe with 50 %. Although PtTe:$PtTe_2$ has the least amount of capping ligand, it is mostly contaminated by NaCl, a by-product of using Na_2O_3Te and $PtCl_4$ as precursors. It is assumed that this material has below 60 weight % of PtTe:$PtTe_2$. HER studies of these catalysts revealed that $PtTe_2$ is a better alkaline HER catalyst because of its low E_{onset} of 29 mV and least η_{-10} of 107 mV. The Pt loading, as determined by ICP-OES, of $PtSe_2$-Se and $PtTe_2$ catalysts on the glassy carbon electrode was determined to be 33.53 and 27.84 m/m %, respectively. Despite the high Pt loading of $PtSe_2$, $PtTe_2$ showed a better alkaline HER performance with a low HER activation energy of 10.3 $kJmol^{-1}$, attributed to high surface roughness, low R_{ct}, and ECSA 4 times higher than $PtSe_2$.

3.5 References

1. Morales-Guio, C. G., Stern, L. A. & Hu, X. Nanostructured hydrotreating catalysts for electrochemical hydrogen evolution. *Chem Soc Rev* 43, 6555 - 6569 (2014).

2. Tachibana, Y., Vayssieres, L. & Durrant, J. R. Artificial photosynthesis for solar water-splitting. *Nat Photonics* 6, 511 - 518 (2012).

3. Shiva Kumar, S. & Lim, H. An overview of water electrolysis technologies for green hydrogen production. *Energy Reports* 8, 13793 - 13813 (2022).

4. Carmo, M. et al. A comprehensive review on PEM water electrolysis. *Int J Hydrog Energy* 38, 4901 - 4934 (2013).

5. Lu, B. et al. Ruthenium atomically dispersed in carbon outperforms platinum toward hydrogen evolution in alkaline media. *Nat Commun* 10, 631 (2019).

6. Ndala, Z. B. et al. Unravelling the effects of surface functionalization on the catalytic activity of $ReSe_2$ nanostructures towards the hydrogen evolution reaction. *Appl Surf Sci* 612, 155971 (2023).

7. Ndala, Z. et al. Evaluating the effect of varying the metal precursor in the colloidal synthesis of $MoSe_2$ nanomaterials and their application as electrodes in the hydrogen evolution reaction. *Nanomater* 10, 1 - 14 (2020).

8. Nkabinde, S. S. et al. Phase-dependent electrocatalytic activity of colloidally synthesized WP and α-WP_2 electrocatalysts for hydrogen evolution reaction. *New J Chem* 45, 15594 - 15606 (2021).

9. Zeng, K. & Zhang, D. Recent progress in alkaline water electrolysis for hydrogen production and applications. *Prog Energy Combust Sci* 36, 307 - 326 (2010).

10. Tan, H. et al. Engineering a local acid-like environment in alkaline medium for efficient hydrogen evolution reaction. *Nat Commun* 13, 2024 (2022).

11. Chen, L. et al. Separating hydrogen and oxygen evolution in alkaline water electrolysis using nickel hydroxide. *Nat Commun* 7, 11741 (2016).

12. David, M., Ocampo-Martínez, C. & Sánchez-Peña, R. Advances in alkaline water electrolyzers: A review. *J Energy Storage* 23, 392 - 403 (2019).

13. Jiang, N. et al. Nickel sulfides for electrocatalytic hydrogen evolution under alkaline conditions: A case study of crystalline NiS, NiS_2, and Ni_3S_2 nanoparticles. *Catal Sci Technol* 6, 1077 - 1084 (2016).

14. Paseka, I. Hydrogen evolution reaction on amorphous Ni-P and Ni-S electrodes and the internal stress in a layer of these electrodes. *Electrochim Acta* 47, 921 - 931 (2001).

15. McGlynn, J. C. et al. Molybdenum ditelluride rendered into an efficient and stable electrocatalyst for the hydrogen evolution reaction by polymorphic control. *Energy Technol* 6, 345 - 350 (2018).
16. Dai, D. et al. Trends in the structure and bonding in the layered platinum dioxide and dichalcogenides PtQ_2 (Q = O, S, Se, Te). *J Solid State Chem* 173, 114 - 121 (2003).
17. Chia, X. et al. Layered platinum dichalcogenides (PtS_2, $PtSe_2$, and $PtTe_2$) electrocatalysis: Monotonic dependence on the chalcogen size. *Adv Funct Mater* 26, 4306 - 4318 (2016).
18. Setiyawati, I., Chiang, K. R., Ho, H. M. & Tang, Y. H. Distinct electronic and transport properties between 1T-$HfSe_2$ and 1T-$PtSe_2$. *Chinese Journal of Physics* 62, 151–160 (2019).
19. Huang, H., Zhou, S. & Duan, W. Type-II dirac fermions in the $PtSe_2$ class of transition metal dichalcogenides. *Phys Rev B* 94, (2016).
20. Guo, C., Huang, L., Li, C., Shang, S. & Du, Z. Thermodynamic Modeling of the Pt-Te and Pt-Sb-Te Systems. *J Electron Mater* 44, 2638–2650 (2015).
21. Vikraman, D. et al. Engineering the active sites tuned MoS_2 nanoarray structures by transition metal doping for hydrogen evolution and supercapacitor applications. *J Alloys Compd* 893, 162271 (2022).
22. Wang, Y. et al. Monolayer $PtSe_2$, a new semiconducting transition-metal-dichalcogenide, epitaxially grown by direct selenization of Pt. *Nano Lett* 15, 4013 - 4018 (2015).
23. Dionisiev, I. et al. Synthesis and characterizations of 2D platinum diselenide. *Mater Proc* 2, 22 (2022).
24. Umar, A. A., Saad, S. K. & Salleh, M. M. Scalable mesoporous platinum diselenide nanosheet synthesis in water. *ACS Omega* 2, 3325 - 3332 (2017).
25. Yarema, M. et al. Upscaling colloidal nanocrystal hot-injection syntheses via reactor under pressure. *Chem Mater* 29, 796 - 803 (2017).
26. Kim, T., Park, S. & Jeong, S. Diffusion dynamics controlled colloidal synthesis of highly monodisperse InAs nanocrystals. *Nat Commun* 12, 3013 (2021).
27. Rohaizad, N. et al. Layered platinum dichalcogenides (PtS_2, $PtSe_2$, $PtTe_2$) for non-enzymatic electrochemical sensor. *Appl Mater Today* 19, 100606 (2020).
28. Imura, S. et al. Effects of grain refinement on surface enhancement of thin-film chlorine-doped crystalline selenium. *J Mater* 28, 7064 - 7069 (2017).
29. Bureau, B. et al. Forming glasses from Se and Te. *Molecules* 14, 4337 - 4350 (2009).
30. Chivers, T. & Laitinen, R. S. Tellurium: A maverick among the chalcogens. *Chem Soc Rev* 44, 1725 - 1739 (2015).

31. Jena, S. et al. Critical assessment of selenourea as an efficient small molecule fluorescence quenching probe to monitor protein dynamics. *Chem Sci* 14, 14200 - 14210 (2023).

32. Hampson, P. & Mathias, A. Nitrogen-14 chemical shifts in ureas. *J Chems Soc B* 673 - 675 (1968)

33. Rostkowska, H. et al. Proton transfer processes in selenourea: UV-induced selenone → selenol photoreaction and ground state selenol → selenone proton tunneling. *Chem Phys* 298, 223 - 232 (2004).

34. Shlykov, S. A. et al. The structures of tellurium (iv) halides in the gas phase and as solvated molecules. *Dalton Trans* 39, 3245 - 3255 (2010).

35. Buss, B. & Krebs, B. The crystal structure of tellurium tetrachloride. *Inorg Chem* 10, 2796 - 2800 (1971).

36. Zhou, P. *et al.* Synthesis of colloidal WSe_2 nanocrystals: Polymorphism control by precursor ligand chemistry. *Cryst Growth Des* 21, 1451 - 1460 (2021).

37. Hwang, Y. & Shin, N. Colloidal synthesis of $MoSe_2/WSe_2$ heterostructure nanoflowers via two-step growth. *Materials* 14, (2021).

38. Guo, W. *et al.* Colloidal synthesis of $MoSe_2$ nanonetworks and nanoflowers with efficient electrocatalytic hydrogen-evolution activity. *Electrochim Acta* 231, 69 - 76 (2017).

39. Sun, Y. *et al.* Low-temperature solution synthesis of few-layer 1T ′-$MoTe_2$ nanostructures exhibiting lattice compression. *Angew Chem* 128, 2880 - 2884 (2016).

40. Xie, R. *et al.* Low-temperature synthesis of colloidal few-layer WTe_2 nanostructures for electrochemical hydrogen evolution. *Discover Nano* 18, (2023).

41. Klein, J. et al. Pt nanocluster size effects in the hydrogen evolution reaction: Approaching the theoretical maximum activity. *Phys Chem* 22, 19059 - 19068 (2020).

42. O'Brien, M. et al. Raman characterization of platinum diselenide thin films. *2D Mater* 3, 021004 (2016).

43. Yao, L. et al. Reactive mechanism of $Cu_2ZnSnSe_4$ thin films prepared by reactive annealing of the Cu/Zn metal layer in a $SnSe_x$ + Se atmosphere. *Crystals* 9, 10 (2019).

44. Fairbrother, A. et al. Secondary phase formation in Zn-rich $Cu_2ZnSnSe_4$-based solar cells annealed in low pressure and temperature conditions. *Prog Photovolt* 22, 479 - 487 (2014).

45. Khanna, P. K. et al. Synthesis of oleic acid capped copper nanoparticles via reduction of copper salt by SFS. *Mater Chem Phys* 110, 21 - 25 (2008).

46. Chen, S. & Liu, W. Oleic acid capped PbS nanoparticles: Synthesis, characterization and tribological properties. *Mater Chem Phys* 98, 183 - 189 (2006).

47. Zhu, K. et al. Two-dimensional transition-metal dichalcogenides for electrochemical hydrogen evolution reaction. *FlatChem* 18, 100140 (2019).

48. Hussain, S. et al. Experimental and theoretical insights to demonstrate the hydrogen evolution activity of layered platinum dichalcogenides electrocatalysts. *J Mater Res Technol* 12, 385 - 398 (2021).

49. Wiensch, J. D. et al. Comparative study in acidic and alkaline media of the effects of pH and crystallinity on the hydrogen-evolution reaction on MoS_2 and $MoSe_2$. *ACS Energy Lett* 2, 2234 - 2238 (2017).

50. Ipadeola, A. K. & Ozoemena, K. I. Alkaline water-splitting reactions over Pd/Co-MOF-derived carbon obtained via microwave-assisted synthesis. *RSC Adv* 10, 17359 - 17368 (2020).

51. Yang, X. et al. Facet-tunable coral-like Mo_2C catalyst for electrocatalytic hydrogen evolution reaction. *Chem Eng J* 451, 138977 (2023).

52. Lin, S. et al. Tunable active edge sites in $PtSe_2$ films towards hydrogen evolution reaction. *Nano Energy* 42, 26 -33 (2017).

53. To, D. T. et al. Hydrogen evolution reaction activities of electrodeposited nanocrystalline Ni - Mo thin films in alkaline baths. *Int J Hydrog Energy* 48, 8409 - 8417 (2023).

54. Laursen, A. B. et al. Molybdenum sulfides - Efficient and viable materials for electro- and photoelectrocatalytic hydrogen evolution. *Energy Environ Sci* 5, 5577 - 5591 (2012).

55. Santos, D. M. F., Sequeira, C. A. C. & Figueiredo, J. L. Hydrogen production by alkaline water electrolysis. *Quim Nova* 36, 1176 - 1193 (2013).

56. Ahmad, K. et al. Thermoluminescence study of pellets prepared using NaCl from Khewra Salt Mines in Pakistan. *Radiat Environ Biophys* 60, 365 - 375 (2021).

57. Hens, Z., Moreels, I. & Martins, J. C. In situ ^{1}H NMR study on the trioctylphosphine oxide capping of colloidal InP nanocrystals. *ChemPhysChem* 6, 2578 - 2584 (2005).

58. Coles, N. T. et al. Phosphinine-based ligands: Recent developments in coordination chemistry and applications. *Coord Chem Rev* 433, 213729 (2021).

59. Seuser, G. S. et al. Understanding uptake of Pt precursors during strong electrostatic adsorption on single-crystal carbon surfaces. *Top Catal* 61, 379 - 388 (2018).

60. Huang, X. et al. High-performance transition metal-doped Pt_3Ni octahedra for oxygen reduction reaction. *Sci* 348, 1230 -1234 (2015).

61. Yu, F. Y. et al. Pt-O bond as an active site superior to PtO in hydrogen evolution reaction. *Nat Commun* 11, 490 (2020).

62. Nguyen, D. A. et al. Patterning of type-II Dirac semimetal $PtTe_2$ for optimized interface of tellurene optoelectronic device. *Nano Energy* 86, (2021).
63. Dong, M. et al. Synthesis of Cu-decorated PtTe nanotubes with high electrocatalytic activity for oxygen reduction. *J Alloys Compd* 770, 76 - 81 (2019).
64. Liu, J. W. et al. Rapid microwave-assisted synthesis of uniform ultralong the nanowires, optical property, and chemical stability. *Langmuir* 26, 11372 - 11377 (2010).
65. Hayashi, H. et al. X-ray photoelectron spectra for the oxidation state of TeO_2-MoO_3 catalyst in the vapor-phase selective oxidation of ethyl lactate to pyruvate. *Catal Lett* 19, 273 - 277 (1993).
66. Wu, Z. et al. Large-area synthesis and photoelectric properties of few-layer $MoSe_2$ on molybdenum foils. *Nanotechnol* 29, 125605 (2018).
67. Ndala, Z. B. et al. Electrocatalytic activity of pristine and electrochemically activated $SnSe_2$ nanoplates for the hydrogen evolution reaction. *J Electroanal Chem* 918, 116464 (2022).
68. De Silva, U. et al. Nickel telluride as a bifunctional electrocatalyst for efficient water splitting in alkaline medium. *J Mater Chem A Mater* 6, 7608 - 7622 (2018).
69. Wang, X. et al. High-temperature chlorination of PbO and CdO induced by interaction with NaCl and Si/Al matrix. *RSC Adv* 8, 34449 - 34458 (2018).
70. Batchelor-McAuley, C. Defining the onset potential. *Curr Opin Electrochem* 37 (2023).
71. Han, W. et al. Designing champion nanostructures of tungsten dichalcogenides for electrocatalytic hydrogen evolution. *Adv Mater* 32, 2002584 (2020).
72. Chen, Z. et al. Metallic W/WO_2 solid-acid catalyst boosts hydrogen evolution reaction in alkaline electrolyte. *Nat Commun* 14, 5363 (2023).
73. Wang, J. et al. Atomic heterointerface engineering of nickel selenide confined nickel molybdenum nitride for high-performance solar-driven water splitting. *Energy Environ Mater* 6, (2023).
74. Bhat, K. S. & Nagaraja, H. S. Nickel selenide nanostructures as an electrocatalyst for hydrogen evolution reaction. *Int J Hydrog Energy* 43, 19851 - 19863 (2018).
75. Pluntke, Y. & Kibler, L. A. Hydrogen evolution electrocatalysis on AgPd (111) alloys. *Electrocatal* 2, 191 - 199 (2011).
76. Sheng, W. et al. Correlating the hydrogen evolution reaction activity in alkaline electrolytes with the hydrogen binding energy on monometallic surfaces. *Energy Environ Sci* 6, 1509 - 1512 (2013).

77. Connor, P. et al. The determination of electrochemical active surface area and specific capacity revisited for the system MnO_x as an oxygen evolution catalyst. *Zeitschrift fur Physikalische Chemie* 234, 979 - 994 (2020).

78. McCrory, C. C. L., Jung, S., Peters, J. C. & Jaramillo, T. F. Benchmarking heterogeneous electrocatalysts for the oxygen evolution reaction. *J Am Chem Soc* 135, 16977 - 16987 (2013).

79. Supriya, S. et al. Comparison between layered Pt_3Te_4 and $PtTe_2$ for electrocatalytic reduction reactions. *FlatChem* 29, 100280 (2021).

80. Chia, X. et al. Layered platinum dichalcogenides (PtS_2, $PtSe_2$, and $PtTe_2$) electrocatalysis: Monotonic dependence on the chalcogen size. *Adv Funct Mater* 26, 4306 - 4318 (2016).

81. Danilovic, N. et al. Enhancing the alkaline hydrogen evolution reaction activity through the bifunctionality of $Ni(OH)_2$/metal catalysts. *Angew Chem Int Ed* 51, 12495 - 12498 (2012).

82. Niu, S. *et al.* Se-doping activates FeOOH for cost-effective and efficient electrochemical water oxidation. *J Am Chem Soc* 141, 7005 - 7013 (2019).

83. Huang, Y., Jiang, L. W., Shi, B. Y., Ryan, K. M. & Wang, J. J. Highly efficient oxygen evolution reaction enabled by phosphorus doping of the Fe electronic structure in iron-nickel selenide nanosheets. *Adv Sci* 8, (2021).

84. Liu, Q. et al. Isolation of high-purity cellulose nanofibers from wheat straw through the combined environmentally friendly methods of steam explosion, microwave-assisted hydrolysis, and microfluidization. *ACS Sustain Chem Eng* 5, 6183 - 6191 (2017).

85. Hosseingholilou, S., Dorranian, D. & Ghoranneviss, M. Characterization of gold nanoparticle thin film prepared by electrophoretic deposition method. *Gold Bull* 53, 1 - 10 (2020).

86. Zak, S., Trost, C. O. W., Kreiml, P. & Cordill, M. J. Accurate measurement of thin film mechanical properties using nanoindentation. *J Mater Res* 37, 1373 - 1389 (2022).

87. Guo, S. et al. Boosting photocatalytic hydrogen production from water by photothermally induced biphase systems. *Nat Commun* 12, 1343 (2021).

88. Bao, N. et al. Novel synthesis of plasmonic $Ag/AgCl@TiO_2$ continues fibers with enhanced broadband photocatalytic performance. *Catal* 7, 117 (2017).

3.6 Supporting Information

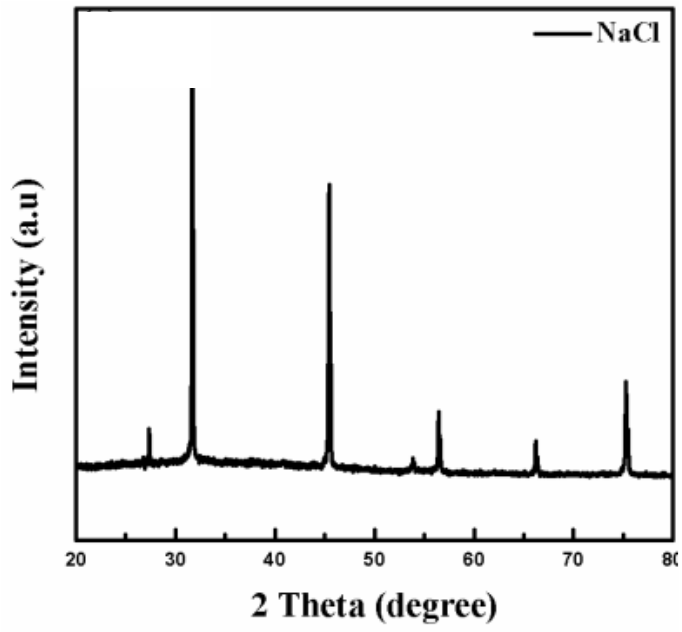

Figure S3.1: XRD pattern of sodium chloride.[88]

Chapter 4

Exploring $PtSe_2$ and $PtSe_2$ anchored on N-MWCNTs as photocathode materials for photo-electrochemical hydrogen evolution reaction

4.1 Introduction

Photo-electrochemical (PEC) ammonia production, carbon dioxide reduction, and hydrogen generation are some reported reactions that use solar energy and show desirable low carbon emissions.[1,2] PEC H_2 can be captured and utilized as a clean energy source or feedstock for other chemical processes. Sustainable PEC H_2 devices rely on efficient and stable photoelectrodes. The photo-conversion efficiencies of these devices are restricted by charge recombination, corrosion, and the development of semiconductors that can efficiently and effectively absorb solar radiation.[3,4] Semiconductor materials that can address these issues while catalyzing the hydrogen and oxygen evolution reactions are sought after to enhance the sustainability of PEC water splitting. In PEC devices, H_2 is generated at the photocathode wherein water is reduced to H_2.[5] Single-phase semiconductors have been utilized as photocathodes whereby suitable band gaps allow for photo-absorption, followed by the generation of electron-hole pairs. The generated electrons facilitate water reduction while holes travel to the anode to facilitate water oxidation.[6,7] A hybrid photoelectrode constructed from a semiconductor and highly conductive material such as silicon and carbon materials has been reported to enhance the charge generation and separation that follows photo-absorption by the composite electrode. The semiconductor photoelectrode material is responsible for photon absorption which is followed by electron excitation from the valence band to the conduction band.[8] The electron then travels through the external circuit to the cathode, where water reduction for H_2 production occurs.[5] The semiconductor material has poor electron transport properties, which increases the chance of electron recombination. A highly conductive material is then included in the composite to facilitate the electron transport to the counter electrode. Usually, carbon materials such as graphene, carbon nanotubes, graphene oxide, and graphene quantum dots are exploited in transition metal semiconductor-based composites to counteract the poor electron transport properties of these compounds.[9–12] Interestingly, these composites are not only deemed suitable for photoelectrodes in PEC devices but also show an overall increased electrocatalytic hydrogen evolution reaction activity. Li Y. et al. evaluated the influence of multiwalled carbon

nanotubes on the HER activity of MoS_2 nanosheets where they observed that MoS_2 required an overpotential of 426 mV versus RHE.[13] Hybridizing MoS_2 with carbon nanotubes, where the weight percent of MoS_2 is 56 %, the overpotential decreased to 284 mV due to improved conductivity. In this study, we explore the growth of $PtSe_2$ nanostructures on the walls of nitrogen-doped multi-walled carbon nanotubes (N-MWCNTs), and the hybrids will be evaluated for light-induced HER in an alkaline medium.

4.2 Experimental Procedure

4.2.1 Chemicals

Oleylamine ($C_{18}H_{37}N$, OLA, 70 %, Sigma-Aldrich), oleic acid ($C_{18}H_{34}O_2$, O.A, 90 %, Sigma-Aldrich), platinum (II) acetylacetonate ($C_{10}H_4O_4Pt$, $Pt(AcAc)_2$, 97 %, Sigma-Aldrich), selenium powder (Se, 99.5 %, Sigma-Aldrich), toluene ($C_6H_5CH_3$, 99 %), Nafion perfluorinated resin solution (5 weight %), isopropanol (C_3H_8O, 99 %, Sigma-Aldrich), ultra-pure water, ethanol (C_3H_5OH, 99.9 %, Sigma-Aldrich), graphite rod (Metrohm), Ag/AgCl auxiliary reference electrode (Metrohm), glassy carbon electrode (GC, Metrohm), potassium hydroxide (KOH, 85 %, Sigma-Aldrich).

4.2.2 In situ synthesis of $PtSe_2$/N-MWCNTs

In situ growth of $PtSe_2$ on the N-MWCNTs was carried out as follows: 8 mL of 1:1 v/v ratio of OLA and O.A was added to a three-neck round flask. This flask was connected to a reflux set-up and the solution was heated to 320 ℃. In a vial, 1 mL of OLA, 1 mL of OA, 10 mg of N-MWCNTs (obtained from our previous work[14]), $Pt(AcAc)_2$ (90 mg, mmol), and Se (42 mg, mmol) were stirred for 72 hours to form a paste-like solution. The paste was then added to the hot OLA: O.A. mixture and the reaction was maintained at 320 ℃ for 1 hour. The hot solution was cooled down to 60 ℃ and the nanoparticles were precipitated by adding toluene. The solution was centrifuged in batches, the liquid discarded, and the nanoparticles dried in an open environment. The same procedure was followed using 20 mg and 30 mg of N-MWCNTs. Thermogravimetric analysis was employed to estimate the relative quantities of $PtSe_2$ and N-MWCNTs in each of the three samples.

4.2.3 Characterization Techniques

The relative quantities of $PtSe_2$ and N-MWCNTs in the composite materials were determined by thermogravimetric analysis (TGA) using a Perkin Elmer Pyris 1 TGA and involved

heating 10 mg of the sample from 35℃ to 900 °C in a nitrogen atmosphere at a heating rate of 10 °C min^{-1} and gas flow rate of 20 mL/min. The crystallinity and phase composition of the composites were examined by X-ray diffraction (XRD) using a Bruker D2 Phaser Powder X-ray diffractometer fitted with a Cu Kα X-ray source (1.54 nm). Measurements were taken over 2θ angle range 10-90° in steps of 0.026° with a step time of 5s at ambient conditions. Raman spectra were recorded on a Horiba Scientific MacroRam Raman Spectrometer equipped with a 785 nm laser, Olympus BX41 microscope. The virtual growth and interaction of $PtSe_2$ and N-MWCNTs in $PtSe_2$/N-MWCNTs hybrid systems was ascertained by microscopy studies using an FEI Tecnai T12 TEM (transmission electron microscopy) microscope operated at 120 KV acceleration voltage. The elemental composition and their corresponding oxidation states were determined by X-ray photoelectron spectroscopy (XPS, Thermo Scientific ESEAlab 250Xi using a 300 W Monochromatic Al kα (1486.7 eV) X-ray beam with a diameter of 900 µm and 20 eV pass energy) characterization techniques were employed to ascertain the morphology and the elemental oxidation states in the nanomaterials. The light absorption properties of $PtSe_2$ and $PtSe_2$/N-MWCNTs were measured using a Varian Cary Eclipse (Cary 50) UV-Vis absorption spectroscopy in a 1 cm path-length quartz cuvette using samples dispersed in EtOH.

4.2.4 Electrochemical Characterization

The electrochemical measurements were carried out using the Biologic SP 300, rotating disk potentiostat in 1 M KOH. A three-electrode cell set-up comprising of graphite rod (counter electrode), Ag wire (reference electrode), and modified glassy carbon working electrode (glassy carbon coated with an ink of the prepared catalysts, 0.196 cm^2) was used for the measurements. The setup is shown in Figure 2. A 2.55 mL dissolving solution containing 1 mL isopropanol, 1.5 mL ultrapure water, and 50 µL of Nafion was used to disperse 5 mg of the $PtSe_2$ and $PtSe_2$/N-MWCNTs powders. The ink mixture was sonicated and then 10 µL of the ink was drop-casted on a pre-cleaned glassy carbon electrode. The glassy carbon was polished by scrubbing on a 1.0 µm followed by 0.5 µm alumina paste and rinsing with ultra-pure water). The ink was dried by rotating the glassy carbon at 250 rpm for approximately 45 min. The calculated catalyst loading was 100 µgcm^{-2}. Linear sweep voltammetry scans of the electrode at 5 mV/s were obtained by applying a potential (-2 V to 0.5 V) to the working electrode while rotating the working electrode at 1600 rpm. The electrochemical impedance spectroscopy (EIS) was carried out by applying potential obtained from the LSV curve at -10 mV/s at a frequency range of 0.1 Hz and 100 kHz while rotating at 1600 rpm. All

electrochemical measurements were performed in a 10 mL electrochemical quartz cell conjugated with argon gas, in the dark and under light. The LED-Based Ossila solar simulator with 1 sun (100 mW/cm^2) irradiance at an 5 cm working distance was used for light-stimulated electrochemical measurements, as shown in Figure 4.1 (b). Before plotting, the potential was corrected against the reference hydrogen electrode, (RHE) using the equations $E_{RHE} = E_{corrected} + (0.059 * pH) + E_{calibrated}$ and $E_{corrected} = E_{measured} - (iR)$, where i is the measured current, R is solution resistance and $E_{calibrated}$ is the Ag/AgCl potential.

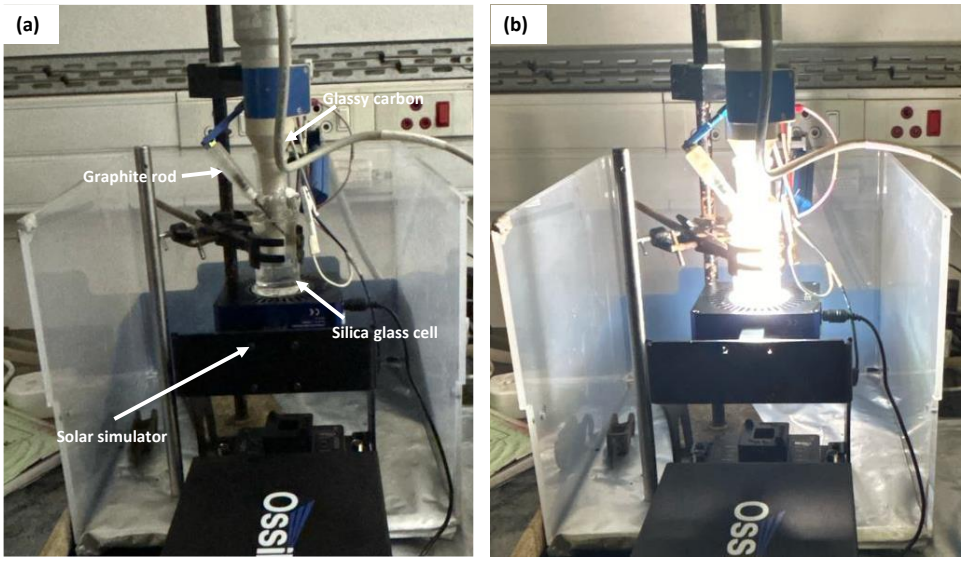

Figure 4.1: Schematic diagram depicting the electrochemical measurement set up with the solar simulator (AM1.5) (a) before switching on the light and (b) when the light is on.

4.3 Results and Discussion

The amount of $PtSe_2$ and N-MWCNTs in the $PtSe_2$/N-MWCNTs composites was estimated by using thermogravimetric analysis carried out under a blanket of nitrogen. The mass loss of $PtSe_2$ on exposure to increasing temperature under an inert atmosphere was tracked by TGA. Although commonly used to assess the thermal stability of compounds, TGA has also been employed to estimate the relative composition of carbon compounds in metal/carbon hybrids.[15,16] The TGA profile of $PtSe_2$ in Figure 4.2 (a)-black shows a minor mass loss commencing at ~120 ℃. This loss is attributed to the dehydration of the sample. As temperature is increased, the weight percentage of the sample continues to decline and at ~420 ℃, 1.8 % of the sample mass is lost. This is attributed to the degradation of the surfactants used in the synthesis procedure. Above 450 ℃, selenium evaporation of $PtSe_2$ begins and continues as the temperature is increased to 900 ℃.[17] The amount of $PtSe_2$ in the

sample can then be assumed to be 98.2 % and 1.8 % is attributed to moisture and organic compounds. This information was used as the basis for the estimation of the amount of $PtSe_2$ and N-MWCNTs in the $PtSe_2$/N-MWCNTs composites. The degradation temperature of N-MWCNTs occurs between 400 and 500 °C, therefore the percentage weight loss at ~500 °C as indicated by the arrows in Figure 4.2 (b)-(d) was used to illustrate the amount of N-MWCNTs, capping ligand, and moisture loss. Where 10 mg of N-MWCNTs were used in the composite preparation, the amount of $PtSe_2$ was estimated as 95 %, where 20 mg of N-MWCNTs was employed, $PtSe_2$ was estimated as 96 % whereas 30 mg of N-MWCNTs, resulted in a composite material with 90 % $PtSe_2$. These composites were labelled as $PtSe_2$/N-MWCNTs (0.05), $PtSe_2$/N-MWCNTs (0.03), and $PtSe_2$/N-MWCNTs (0.1).

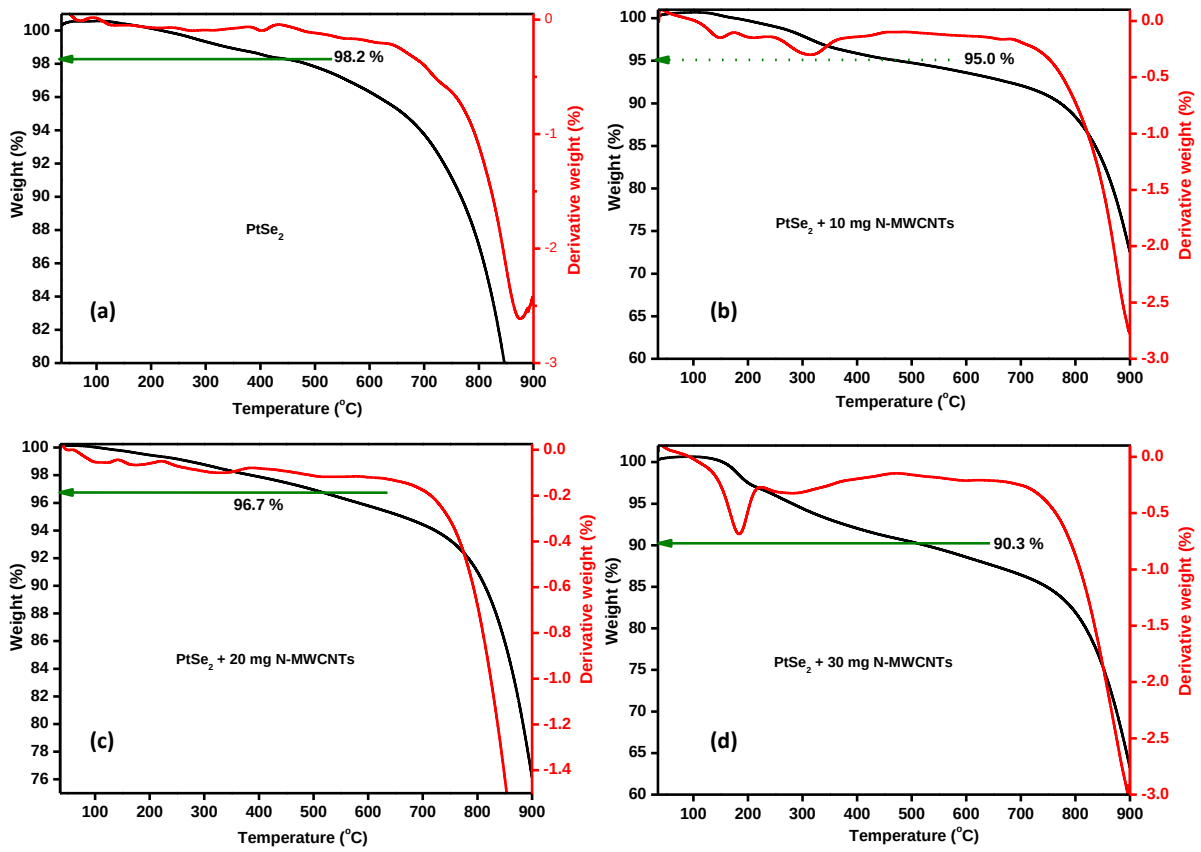

Figure 4.2: TGA/DTG profiles of $PtSe_2$ and in situ prepared $PtSe_2$/N-MWCNTs composites.

The XRD patterns of $PtSe_2$, $PtSe_2$/N-MWCNTs (0.03), $PtSe_2$/N-MWCNTs (0.05), and $PtSe_2$/N-MWCNTs (0.1) are shown in Figure 4.3 (a). The observed diffraction peaks are ascribed to the Sudovikovite, syn (PDF: 03-065-3374) $PtSe_2$. The samples are free of impurities except $PtSe_2$/N-MWCNTs (0.05), which have traces of Pt (marked *). Generally, the carbon nanotubes' XRD peaks are not observed in the XRD patterns of the composites if the quantity of the tubes is very minimal. The amount of N-MWCNTs in the three composites

is very small, less than 10 weight %. In carbon nanotube-based composites, the nanotubes are usually not detectable by XRD.[14] It is, however, clear that the in situ growth of $PtSe_2$ on the nanotubes does not affect the crystallographic parameters of $PtSe_2$. TEM analysis of the samples was carried out to determine the presence of the two microstructures in the composites (Figure 4.3 (b) – (d)). No significant change is observed when the N-MWCNTs weight percent is increased from 3 to 10 %. It is noticeable that, although most of the nanotubes are covered with $PtSe_2$, N-MWCNTs that have smooth surfaces and no particles on them are available. This could be due to incomplete functionalization of the nanotube surfaces during acid treatment. The $PtSe_2$ forms clusters of petal-like structures unevenly covering the nanotubes.

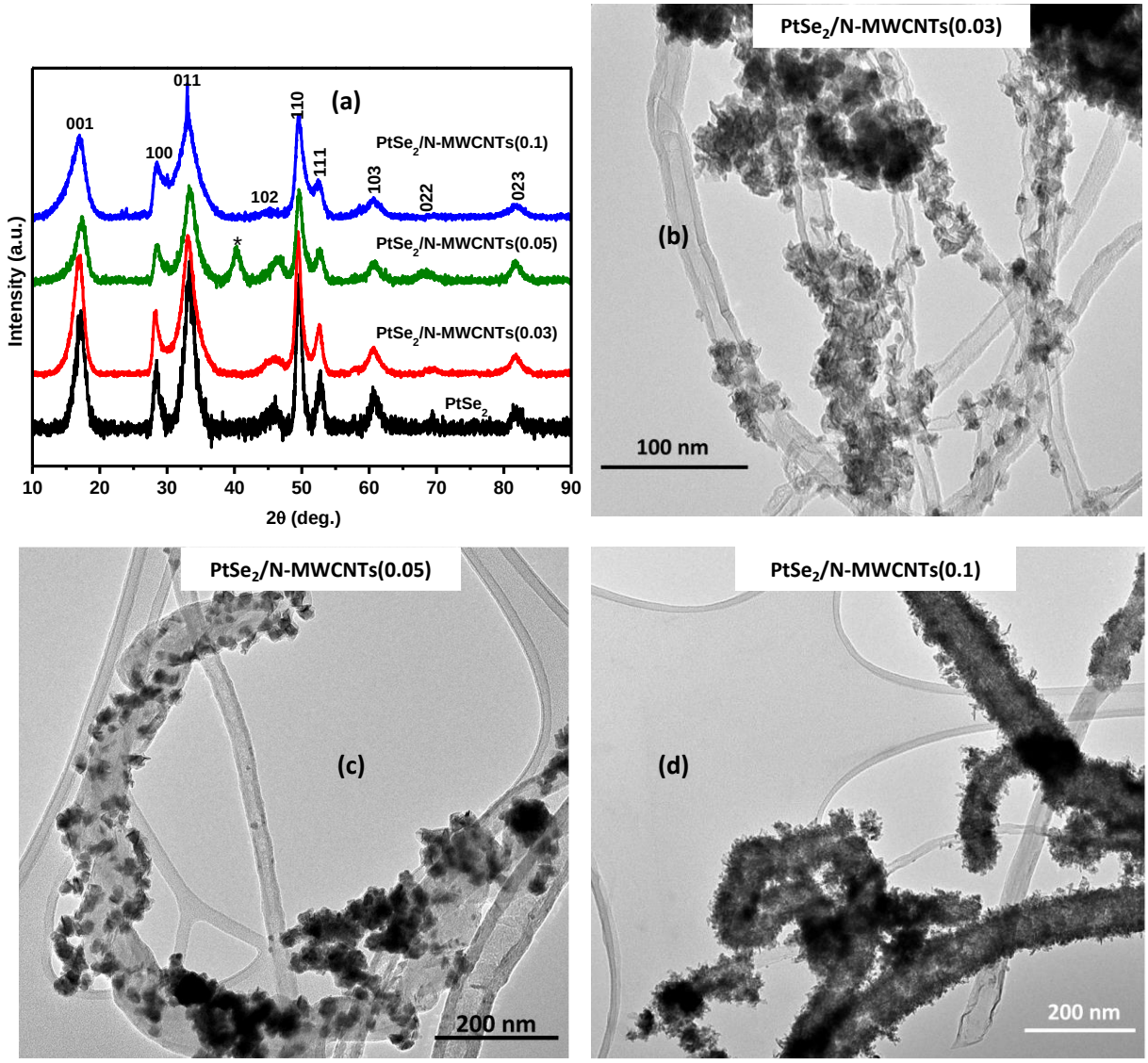

Figure 4.3: (a) Raman spectra of $PtSe_2$ and $PtSe_2$/N-MWCNTs (0.1) and (b)-(d) are TEM images of $PtSe_2$/N-MWCNTs (0.03), $PtSe_2$/N-MWCNTs (0.05) and $PtSe_2$/N-MWCNTs (0.1), respectively.

The degree of graphitization, defects in the N-MWCNTs, and the incorporation of the N-MWCNTs in $PtSe_2$ were assessed by Raman spectroscopy. Raman spectra of $PtSe_2$, N-MWCNTs, and $PtSe_2$/N-MWCNTs (0.1) are shown in Figure 4.4 (a). $PtSe_2$ is characterized by two main Raman peaks, the in-plane (E_g) and out-of-plane (A_{1g}) selenium vibrations on the Pt atoms, respectively. The E_g peak is reported to occur at 180 cm^{-1}, while the A_{1g} occurs at slightly higher energy at 210 cm^{-1}.[18,19] These peaks are observed at 177 cm^{-1} and 209 cm^{-1} in the $PtSe_2$ prepared by colloidal synthesis. The additional peaks observed in the Raman spectrum of $PtSe_2$ between 1000 and 2000 cm^{-1}, demonstrate the presence of the organic capping ligands. OLA and O.A, are used in the synthesis of this compound. The N-MWCNTs

have two distinct Raman peaks at 1335 and 1578 cm^{-1} ascribed to the D and G bands, respectively. The low energy peak is a defect peak while the higher energy peak is attributed to the graphitic nature of the carbon material. The synthesis procedure or post-synthesis treatment of the nanotubes is the primary course of defects in carbon nanotubes. The area ratio of the D and G bands (A_D/A_G) indicates the quality of the nanotubes relative to defects quantity, whereby a low ratio speaks to fewer defects in the carbon structure.[20,21] Defects in carbon nanotubes are attributed to the presence of hetero atom dopants, vacancies, or impurities.[21] The Raman spectrum of the $PtSe_2$/N-MWCNTs (0.1) display peaks due to $PtSe_2$ and the D and G peaks at 1330 and 1578 cm^{-1}, respectively, and A_D/A_G ratio of 2.0, slightly lower than in the N-MWCNTs. As a result, the presence of N-MWCNTs in the $PtSe_2$/N-MWCNTs composites is accounted for. Heteroatom doping of carbon nanotubes, particularly nitrogen doping influences the properties of the nanotubes. N-MWCNTs with high quantities of the dopant are less stable than pristine MWCNTs. However, the electron conductivity of the N-MWCNTs is improved compared to MWCNTs, a parameter important in electron transfer HER. It is thus assumed that the nitrogen-doped carbon nanotubes will improve the conductivity of $PtSe_2$.

The XPS analysis $PtSe_2$/N-MWCNTs (0.1) was employed to determine the elemental composition and oxidation states of the elements in the composite. The XPS survey spectrum is shown in Figure 4.4 (b). Pt, Se, C, O, and N are the major elements present in the $PtSe_2$/N-MWCNTs (0.1). Table 4.1 summarizes the weight and atomic compositions of these elements in $PtSe_2$/N-MWCNTs (0.1). Generally, the sample consists of a high C atomic percentage, which implies presence of the carbon nanotubes in the composite. The Pt high-resolution XPS spectrum (Figure 4.4 (c)) shows a doublet peak at 76.2 and 72.9 eV with energy splitting of 3.0 eV, attributed to Pt^{2+}. The peaks at 74.8 and 71.9 eV show the presence of elemental Pt traces in the composites. Elemental Pt was, however, not picked up by XRD and traces of this metal enhance the HER of various catalysts. As such, the presence of this element does not negatively impact the performance of the prepared catalysts.

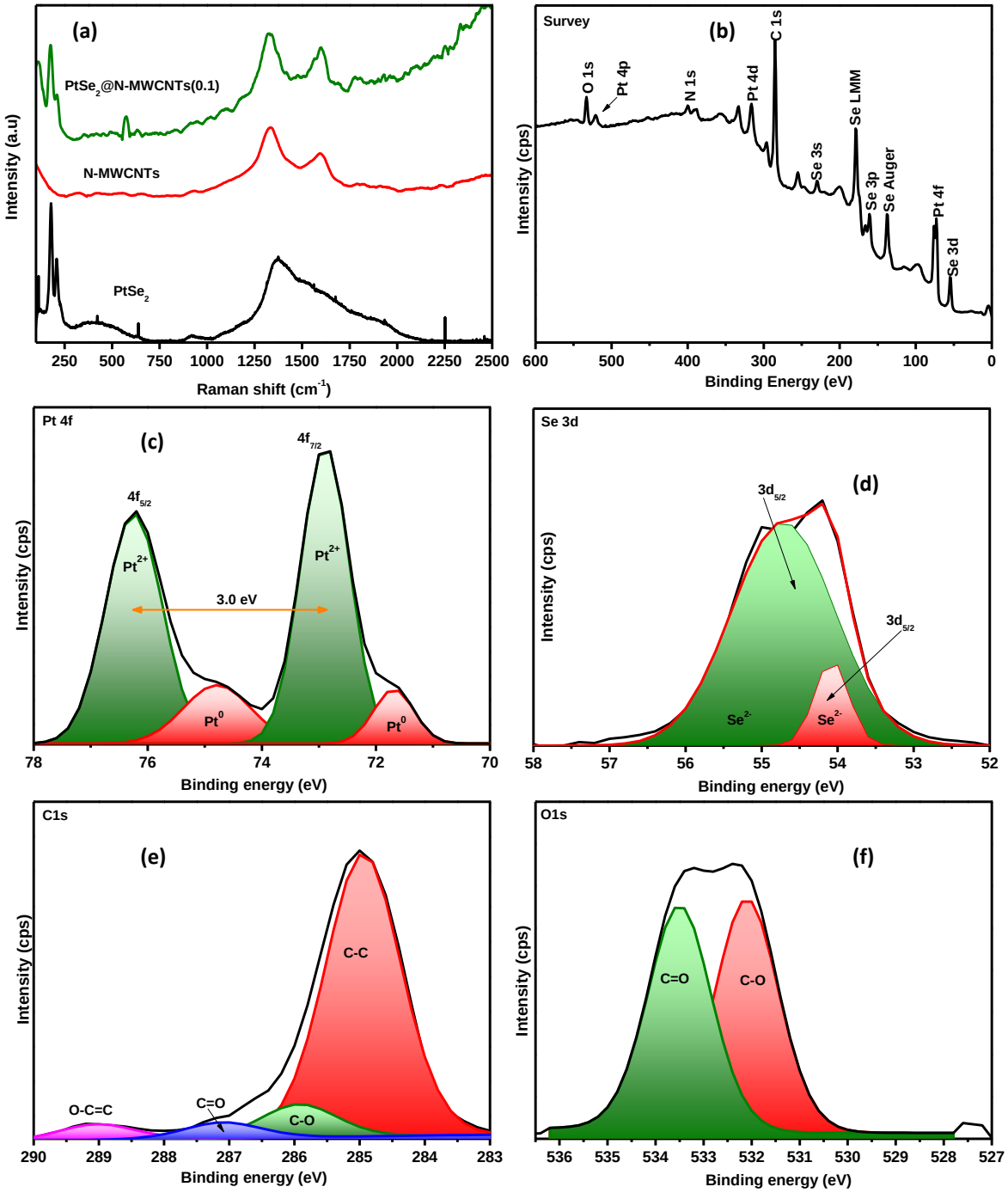

Figure 4.4: (a) Raman spectra of $PtSe_2$/N-MWCNTs (0.1) constituents, (b) XPS survey spectrum of $PtSe_2$/N-MWCNTs (0.1) and the XPS high-resolution spectra of (c) platinum, (d) selenium, (e) carbon, and (f) oxygen.

The selenium 3d core level XPS spectrum in Figure 4.4 (d) reveals a peak at 54 eV, which was deconvoluted to two peaks at 54.8 and 54.0 eV corresponding to the $3d_{3/2}$ and $3d_{5/2}$, respectively. The binding energies of Pt and Se are consistent with Pt and Se energies of $PtSe_2$ by other authors.[22–24] The atomic percentage ratio of Pt^{2+} and Se^{2-} is 1:3.3, which is

larger than the expected 1:2 ratio. The XPS core level spectrum of C in Figure 4.4 (e) shows the presence of four types of carbon, graphitic carbon, (C-C, 284.9 eV), organic carbon (C-O, 286 and C=O, 287.1 eV), and O-C=C carbon (289 eV). The corresponding oxygen peaks in Figure 4.4 (f) are observed at 533 eV. The presence of oxidized carbon indicates that the carbon nanotubes have oxygen functional groups, including OH^- and carboxylic moieties. These functionalities are crucial in the composite preparation because they act as nucleation sites for the growth of $PtSe_2$ on the N-MWCNTs.

Table 4.1: XPS elemental composition and bonding configurations in $PtSe_2$/N-MWCNTs (0.1)

Element	Assignment	Binding energy (eV)	Atomic (%)
Pt	Pt^{2+} $4f_{5/2}$	72.9	3
	Pt^0 $4f_{7/2}$	71.6	0.7
Se	Se^{2-} $3d_{3/2}$	54.8	9.6
	Se^{2-} $3d_{5/2}$	54.0	
O	Organic C-O	532.1	3.7
	Organic C=O	533.5	3.6
C	C-C	284.9	64.6
	C-O	286.0	7.5
	C=O	287.1	3.7
	O-C=C	289.0	3.6

The optical properties of the $PtSe_2$/N-MWCNTs and the respective constituent materials were determined by UV-Vis absorption spectroscopy in EtOH and are depicted in Figure 4.6 (a). The normalized light absorption of $PtSe_2$ and N-MWCNTs is high at high energy (ultraviolet region) and declines as the light energy goes to the visible region. However, the composite materials reveal a slightly improved absorption in the visible region. The absorption of the composites remains almost unchanged when the N-MWCNTs weight is below 10 %. The band gap of $PtSe_2$ and carbon nanotubes was determined by a Tauc plot and the effect of adding the nanotubes with increasing weight % to the $PtSe_2$ matrix was evaluated. Band gap manipulation is crucial in semiconductor materials as it improves the solar absorption spectrum of the semiconductor. The band gap computational calculations estimate the band gap of $PtSe_2$ at 1.18 eV for monolayer $PtSe_2$, while bilayer $PtSe_2$ exhibits a low band gap

energy of 0.24 eV and 0 for more than 5 layers of $PtSe_2$.[25,26] There is limited experimental band gap reporting of multi-layered $PtSe_2$. Ciarrocchi et al. exfoliated bulk $PtSe_2$ onto a silicon substrate and produced a thick $PtSe_2$.[27] They determined the band gap of 2.5 mm thick $PtSe_2$ as 2.2 eV and attributed the difference between theoretical calculations and their study on underestimation of the band gap by DFT calculations. This study obtained a band gap of around 2.1 eV for multi-layered $PtSe_2$. The $PtSe_2$ band gap increased approximately to 2. 75 eV, 2.85 eV, and 3 eV when $PtSe_2$ was hybridized with 10, 3, and 5 weight % N-MWCNTs. 5 weight % of N-MWCNTs improves the band gap of $PtSe_2$ by the largest amount of around 0.9 eV. This means that incorporation of the carbon me$_2$.

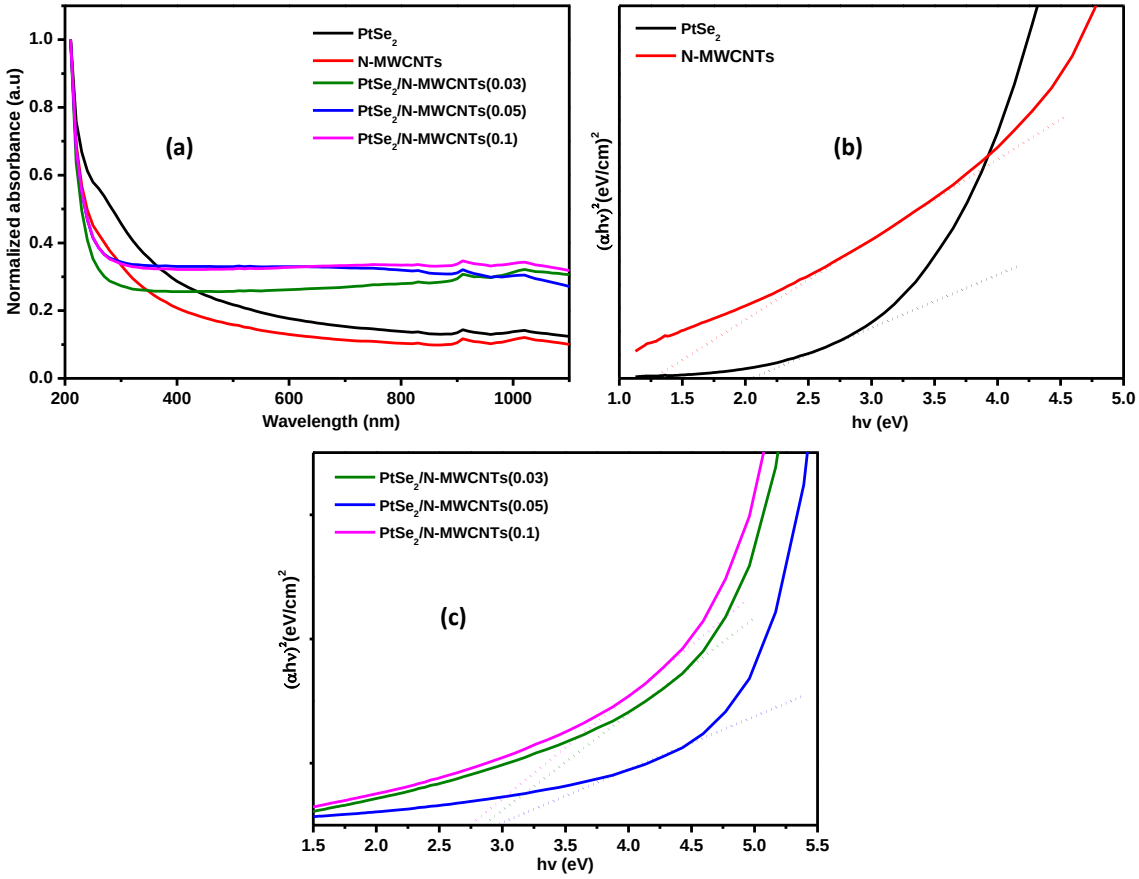

Figure 4.5: The UV-Vis absorption spectra of $PtSe_2$, N-MWCNTs, $PtSe_2$/N-MWCNTs (0.03), $PtSe_2$/N-MWCNTs (0.05) and $PtSe_2$/N-MWCNTs (0.1).

The light-activated HER performance of $PtSe_2$, $PtSe_2$/N-MWCNTs (0.03), $PtSe_2$/N-MWCNTs (0.05), and $PtSe_2$/N-MWCNTs (0.1) catalysts was determined by LSV measurements by illuminating light onto the catalyst-modified glassy carbon (GC) electrode.

The distance between the light source and the GC was maintained at 5 cm. All the electrochemical measurements were repeated in the dark. The polarization curve shown in Figure 4.6 (a) compares the HER catalytic performance of the catalysts by critically analyzing the overpotential (η_{-10}) required to produce a current density of -10 $mAcm^{-2}$. In the dark, $PtSe_2$ displays an η_{-10} of 400 mV. As the concentration of N-MWCNTs is increased from 3 weight % ($PtSe_2$/N-MWCNTs (0.03)) to 5 weight % ($PtSe_2$/N-MWCNTs (0.05)), the η_{-10} decreases from 274 mV to 159 mV, respectively. On drastically increasing the quantity of the nanotubes to 10 weight % ($PtSe_2$/N-MWCNTs (0.1), the HER activity of the composite decreases, and an η_{-10} of 1038 mV is observed.

For the light-induced HER, the same trend is observed where $PtSe_2$ has an η_{-10} of 87 mV and the η_{-10} improves on incorporating the carbon nanotubes where $PtSe_2$/N-MWCNTs (0.05) shows the most improved HER performance with η_{-10} of 78 mV $PtSe_2$/N-MWCNTs (0.1) displays the poorest η_{-10} of 626 mV under the light. Generally, the HER activity of the catalysts improves when light is illuminated on the catalysts, and using small quantities of N-MWCNTs improves the overall catalytic activity of $PtSe_2$. This could be attributed to the slight increase in the band gap of the $PtSe_2$ and carbon nanotube composites, the improved conductivity of the composites, and the possible modified electronic structure that results from hybridization as opposed to the pristine $PtSe_2$.

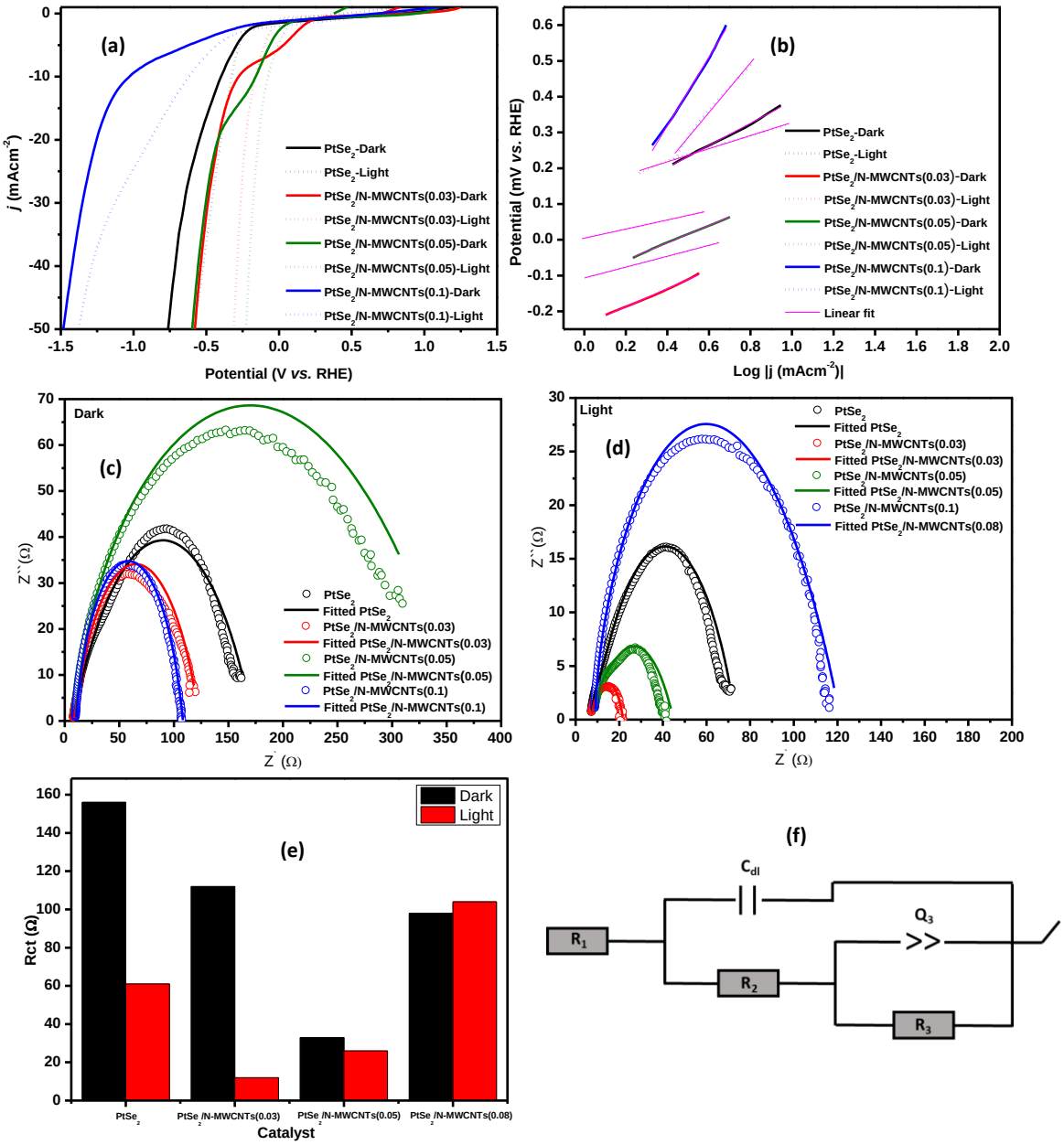

Figure 4.6: (a) Polarization curves, (b) Tafel plots derived from LSV data, (c) Nyquist plot in the dark, (d) Nyquist plot under illumination, (e) bar graph comparing Rct values of $PtSe_2$, and $PtSe_2$/N-MWCNTs composites, and (f) the electrochemical equivalent circuit modelled from the EIS data.

The polarization current can be linearized and plotted against the potential to obtain a slight line plot that is used to estimate the Tafel slope, shown in Figure 4.6 (b). Tafel slope is a HER kinetic indicator that gives information about the performance of the catalyst.[4] For all the catalysts, the Tafel slopes decline under illumination. This suggests that light increases the overall HER kinetics. $PtSe_2$/N-MWCNTs (0.1) and $PtSe_2$ exhibit the highest Tafel slopes of 959 and 309 $mVdec^{-1}$ in the dark and, 656 and 183 $mVdec^{-1}$ under illumination, respectively.

The Tafel slope declines from 250 mVdec^{-1} in $PtSe_2$/N-MWCNTs (0.03) to 240 mVdec^{-1} in $PtSe_2$/N-MWCNTs (0.05) in the dark. Light stimulation of the catalysts results in the Tafel slope of $PtSe_2$/N-MWCNTs (0.3) and $PtSe_2$/N-MWCNTs (0.05) decreasing to 127 and 152mVdec^{-1}, respectively. $PtSe_2$/N-MWCNTs (0.03) show the greatest decrease in the Tafel slope where the slope is reduced to half the value of the slope in the dark. Thus far, the $PtSe_2$/N-MWCNTs (0.05) exhibit the smallest η_{-10} and a relatively low Tafel slope, rendering this composite an efficient HER catalyst under light (AM1.5).

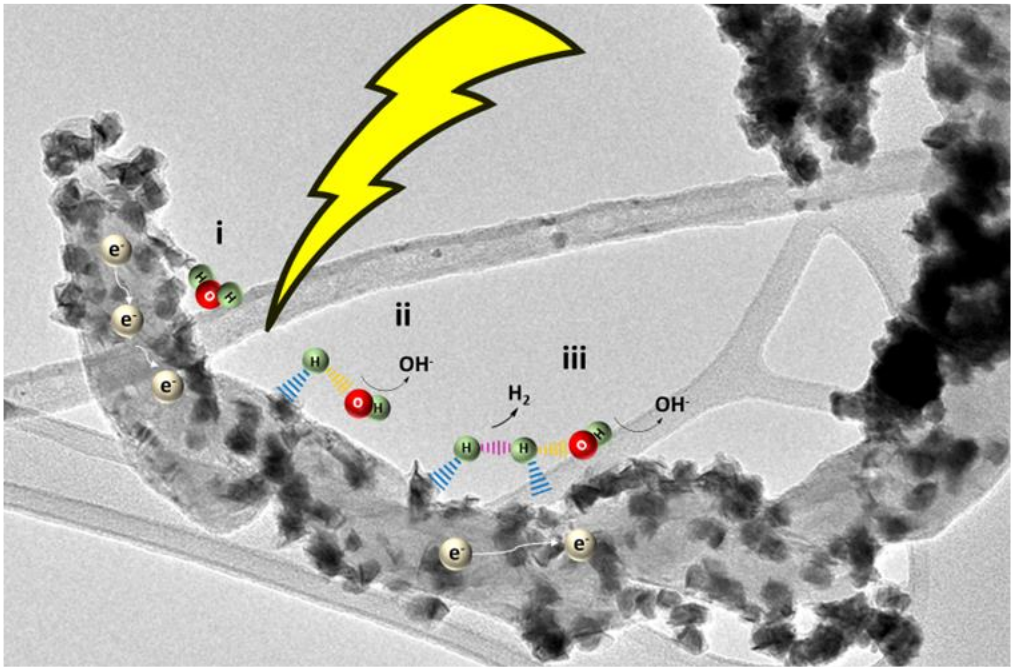

Figure 4.7: The postulated HER mechanism on the $PtSe_2$/NMWCNTs

Following the water dissociation to generate hydroxide ions and H atoms on the surface of the catalyst, the H_2 generation proceeds via the Tafel or Heyrovsky step. The value of the Tafel slope indicates whether the Volmer-Tafel or Volmer-Heyrovsky takes place. For Tafel slope values below 116 mVdec^{-1}, the Volmer-Heyrovsky mechanism dominates. The Volmer-Heyrovsky mechanism is reported to be the most popular for alkaline HER. Very high Tafel slopes, as in this study, have been reported before by various authors and are attributed to an addition reaction step, the intense H_2 adsorption on the catalyst active sites.[28] This means that, as the adsorbed hydrogen atoms interact to produce H_2, the H_2 molecule does not readily go into solution but rather interacts with the catalyst surface. The exchange current density, j_o, obtained by extrapolating the Tafel lot where the potential is zero indicates the rate of the HER at equilibrium. The larger the j_o is, the more catalytic the catalyst is. The j_o of $PtSe_2$ improves by coalescing with 3 and 5 weight % N-MWCNTs but declines on

increasing the N-MWCNTs to 10 %. This observation holds in dark and light conditions. The HER performance parameters of the prepared catalysts are summarised in Table 4.2 and indicate that $PtSe_2$/N-MWCNTs (0.05) is a better alkaline HER catalyst under light.

Table 4.2: Summary of the electrochemical performance indicators for HER (D= dark, L=light).

Catalyst		η_{-10}(mV)	b (mVdec^{-1})	j_o (mAcm^{-2})	R_{ct} (Ω)	ECSA (cm^2)
$PtSe_2$	D	400	309	0.559	156	-
	L	339	183	0.162	62	30
$PtSe_2$/N-MWCNTs (0.03)	D	274	250	8.825	112	2.4
	L	162	127	0.923	12	94
$PtSe_2$/N-MWCNTs (0.05)	D	159	241	2.276	351	38
	L	78	152	5.047	32	38
$PtSe_2$/N-MWCNTs (0.1)	D	1038	959	1.170	97	-
	L	626	696	1.227	104	75

The EIS measurements further evaluated the alkaline HER kinetics of the catalysts. The corresponding Nyquist plots of the various catalysts in the dark are shown in Figure 4.6 (c), while Figure 4.6 (d) shows the Nyquist plot under the light. All the plots were then modelled to an electrochemical equivalent circuit shown in Figure 6 (e). The constituents of the circuit are R_s, which is the resistance of the 1 M KOH electrolyte, the C_{dl}, which represents the double-layer capacitance at the electrode surface, and Q3, which is the constant phase element. R2 and R3 correspond to surface film resistance and charge transfer resistance, R_{ct}, respectively.[29] R_{ct} is the electrochemical parameter of the electron transfer or more simply, indicates the conductivity of different catalysts. A low R_{ct} value illustrates that the specific catalyst has a low resistance or hindrance to electron motion, thus considered to have better electron transfer properties. The charge transfer resistance improved drastically as the weight percent of the nanotubes was increased to 3 %, and 5 %, which suggests that the electron flow of the $PtSe_2$ is improved upon hybridization with the nanotubes.

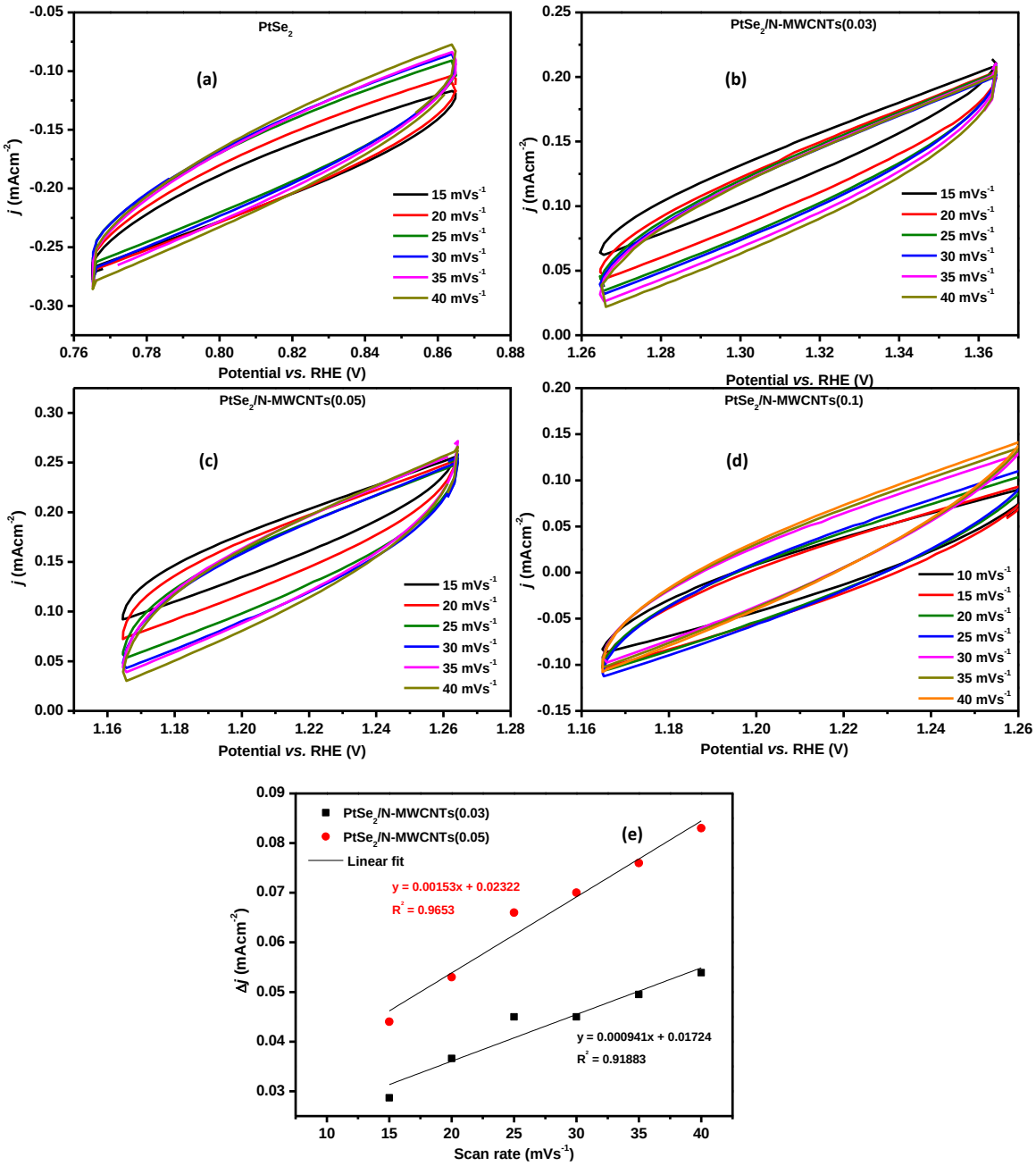

Figure 4.8: The plot of change in current density with scan rate for (a) $PtSe_2$, (b) $PtSe_2$/N-MWCNTs (0.03) (c) $PtSe_2$/N-MWCNTs (0.05), and (d) $PtSe_2$/N-MWCNTs (0.1) at scan rate from 10 mVs^{-1} to 40 mVs^{-1} and (e) C_{dl} plot for $PtSe_2$/N-MWCNTs (0.03) and $PtSe_2$/N-MWCNTs (0.05) in the dark.

Figure 4.6 (e) shows the bar graph comparing the Rct values in the dark and under illumination and the trend in the R_{ct} change with increasing N-MWCNT concentration. The R_{ct} of $PtSe_2$/N-MWCNTs (0.05) is largest in the dark at 351 Ω, followed by $PtSe_2$ at 156 Ω, and $PtSe_2$/N-MWCNTs (0.03) with an R_{ct} value of 112 Ω. The $PtSe_2$/N-MWCNTs (0.1) demonstrate the smallest R_{ct} value of 97 Ω in the dark. Interestingly, this composite shows

the largest R_{ct} of 104 Ω under illumination. The 3 and 5 weight % incorporation of N-MWCNTs in $PtSe_2$ produces composites with 5 times and 3 times smaller R_{ct} values, respectively, compared to $PtSe_2$. $PtSe_2$/N-MWCNTs (0.03) and $PtSe_2$/N-MWCNTs (0.05) depict that the electron transfer rate is sped up while the electron transport obstruction is lowered by using light and incorporating N-MWCNTs in $PtSe_2$.[30]

The electrochemical surface area (ECSA) of the prepared catalysts was determined in both light-induced and dark conditions. Figure 4.8 (a) – (d) shows the current density response at increasing scan rates, from 10 to 40 mVs^{-1} of $PtSe_2$, $PtSe_2$/N-MWCNTs (0.03), $PtSe_2$/N-MWCNTs (0.05), and $PtSe_2$/N-MWCNTs (0.1), respectively, under dark conditions. The current versus scan rate for $PtSe_2$ and $PtSe_2$/N-MWCNTs (0.1) does not have a linear relationship. A linear relationship between current density and scan rate is observed for $PtSe_2$/N-MWCNTs (0.03), and $PtSe_2$/N-MWCNTs (0.05), especially in the cathodic region which allows for the ECSA determination of the two catalysts under dark (Figure 4.8 (e)). The ECSA of 38.3 and 2.4 cm^2 was obtained for $PtSe_2$/N-MWCNTs (0.05), and $PtSe_2$/N-MWCNTs (0.03). Under illumination, the relationship between scan rate and current density is linear for the catalysts, and the C_{dl} plots are shown in Figure 4.9 (a)-(d) for $PtSe_2$, $PtSe_2$/N-MWCNTs (0.03), $PtSe_2$/N-MWCNTs (0.05), and $PtSe_2$/N-MWCNTs (0.1), respectively. Figure 4.9 (e) compares the double-layer capacitance of the catalysts and the corresponding ECSA is summarised in Table 4.2. Generally, we observed that the ECSA of $PtSe_2$, under illumination, improved when the nanotubes were incorporated. However, the ECSA obtained for the catalysts does not follow the trend observed in the catalytic performance of the composites under illumination.

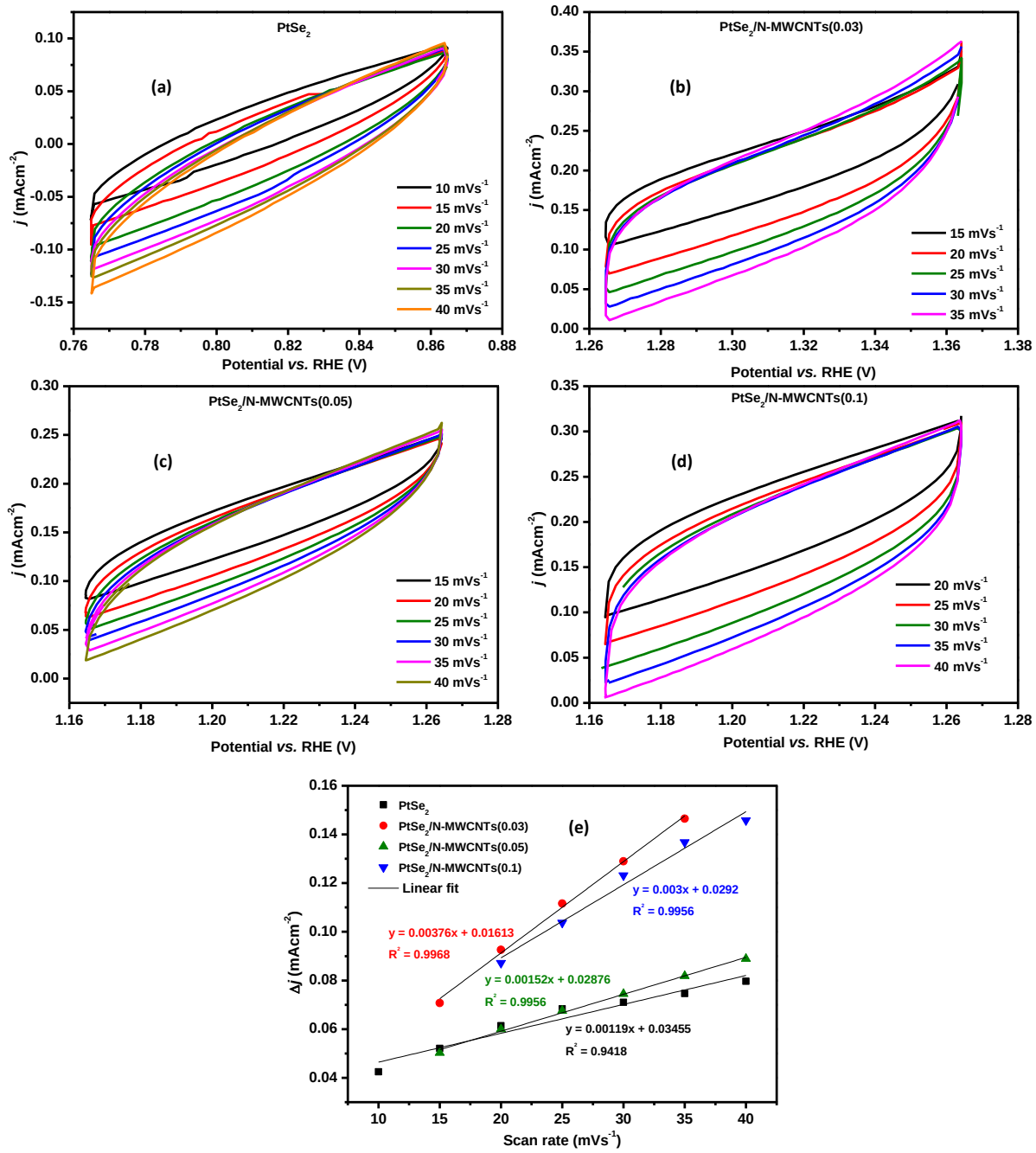

Figure 4.9: The plot of change in current density with scan rate of (a) $PtSe_2$, (b) $PtSe_2$/N-MWCNTs (0.03) (c) $PtSe_2$/N-MWCNTs (0.05), and (d) $PtSe_2$/N-MWCNTs (0.1) and the corresponding C_{dl} plots obtained under light illumination of the catalysts.

4.4 Conclusions

In summary, the $PtSe_2$ nanostructures were grown on the nitrogen-doped multiwalled carbon nanotubes by modification of the $PtSe_2$ colloidal synthesis method developed in Chapter 3. The amount of the nanotubes in the composites was increased and based on the TGA of the samples, the composites were assumed to contain 3, 5, and 10 weight percent of the

nanotubes. Because the amount of the nanotubes was below 10 weight %, the nanotubes could not be detected by XRD. However, TEM and Raman analysis of the samples confirmed the existence of $PtSe_2$ and nanotube structures in the hybrid systems. The oxidation states of Pt and Se were determined to be +2, and -2, respectively. The band gap of $PtSe_2$ was obtained as 2.1 eV using Tauc plot and the incorporation of the carbon nanotubes increased the value of the band gap. The light-stimulated HER of $PtSe_2$ revealed that the prepared $PtSe_2$ performance is influenced by light leading to the confirmation that that it is a semi-conductor, although it is multi-layered. The HER activity of $PtSe_2$ improved when the nanotube weight % was increased from 3 % to 5% in both light and dark conditions. The HER activity declined when the nanotubes were increased to 10 weight %. Generally, this chapter demonstrates that exposing light (AM 1.5) to the $PtSe_2$ and $PtSe_2$/N-MWCNTs electrodes improves the alkaline HER activity. This opens an opportunity to further explore these catalysts as either photoanodes or photocathodes in PEC HER.

4.5 References

1. Kistler, T. A. et al. photoelectrochemical CO_2 reduction producing syngas at 10% efficiency. *Adv Energy Mater* 11, 2100070 (2021).

2. Deng, X. *et al.* Metal-organic framework coating enhances the performance of Cu_2O in photoelectrochemical CO_2 reduction. *J Am Chem Soc* 141, 10924 - 10929 (2019).

3. Kamat, P. V. & Sivula, K. Photoelectrochemical and photocatalytic hydrogen generation: A virtual issue. *ACS Energy Lett* 7, 4379 - 4380 (2022).

4. Poonia, K. et al. Photo-electrocatalytic systems for simultaneous energy recovery and wastewater treatment: A review. *Environ Chem Lett* 21, 265 - 283 (2023).

5. Lam, N. H. et al. Improving the photoelectrochemical water splitting performance of CuO photocathodes using a protective $CuBi_2O_4$ layer. *Sci Rep* 13, 5776 (2023).

6. Paracchino, A. et al. Highly active oxide photocathode for photoelectrochemical water reduction. *Nat Mater* 10, 456 - 461 (2011).

7. Thakur, A. et al. Current progress and challenges in photoelectrode materials for the production of hydrogen. *Chem Eng J* 397, 125415 (2020).

8. Krishnan, A. et al. Ni-based electro/photo-catalysts in HER - A review. *Surf Interfaces* 36, 102619 (2023).

9. Wu, Y. L. et al. Auxiliary ball milling to prepare WS_2/graphene nanosheets composite for lithium-ion battery anode materials. *Tungsten* 6, 124 - 133 (2023).

10. Le, P. A. et al. One-step surface-plasma-induced exfoliation of the graphite/WS_2 bilayer into homogeneous two-dimensional graphene/WS_2 nanosheet composites as catalysts for the hydrogen evolution reaction. *ACS Appl Energy Mater* 4, 5143 - 5154 (2021).

11. Moradpur-Tari, E., Sarraf-Mamoory, R. & Yourdkhani, A. 1T-WS_2/Graphene on activated carbon cloth as a flexible electrode for wearable supercapacitors. *Ceram Int* 48, 8563 - 8571 (2022).

12. Zhu, K. et al. Few-layer MoS_2 nanosheet/carbon nanotube composite films for long-lifetime lithium storage and hydrogen generation. *ACS Appl Nano Mater* 4, 4754 - 4762 (2021).

13. Li, Y. et al. Efficient and scalable preparation of MoS_2 nanosheet/carbon nanotube composites for hydrogen evolution reaction. *Int J Hydrog Energy* 45, 16489 - 16499 (2020).

14. Mxakaza, L. et al. Cu_2ZnSnS_4/N-MWCNTs hybrid systems as counter electrode substitutes for platinum in dye-sensitized solar cells. *J Mater Res* 39, 1 - 13 (2024)

15. Ou, X. et al. In situ X-ray diffraction characterization of $NiSe_2$ as a promising anode material for sodium ion batteries. *J Power Sources* 343, 483 - 491 (2017).

16. Lone, M. A. et al. Rapid hydrothermal synthesis of mesoporous NiS_2 and $NiSe_2$ nanostructures for wastewater treatment. *Heliyon* 9, e22308 (2023).

17. Jha, N. et al. Synthesis, optimization, and physicochemical characterization of selenium nanoparticles from polysaccharide of mangrove Rhizophora mucronata with potential bioactivities. *JMEMIN* 2, 100019 (2022).

18. Umar, A. A., Saad, S. K. & Salleh, M. M. Scalable mesoporous platinum diselenide nanosheet synthesis in water. *ACS Omega* 2, 3325 - 3332 (2017).

19. Yim, C. et al. High-performance hybrid electronic devices from layered $PtSe_2$ films grown at low temperature. *ACS Nano* 10, 9550 - 9558 (2016).

20. Tetana, Z. N. et al. The synthesis of nitrogen-doped multiwalled carbon nanotubes using an Fe-Co/$CaCO_3$ catalyst. *S Afr J Chem* 65, 39 - 49 (2012).

21. Dinda, S. et al. Quantifying defects in carbon nanotubes undergoing prolonged electrochemical cycling with Raman phase map. *Carbon* 218, 118753 (2024).

22. Wang, Y. et al. Monolayer $PtSe_2$, a new semiconducting transition-metal-dichalcogenide, epitaxially grown by direct selenization of Pt. *Nano Lett* 15, 4013 - 4018 (2015).

23. Lin, S. et al. Tunable active edge sites in $PtSe_2$ films towards hydrogen evolution reaction. Nano *Energy* 42, 26 - 33 (2017).

24. Yuan, J. et al. Few-layer platinum diselenide as a new saturable absorber for ultrafast fiber lasers. *ACS Appl Mater Interfaces* 10, 21534 - 21540 (2018).

25. Villaos, R. A. B. et al. Thickness dependent electronic properties of Pt dichalcogenides. *Mater Appl* 3, 1-8 (2019).
26. Li, J. et al. Layer-dependent band gaps of platinum dichalcogenides. *ACS Nano* 15, 13249 -13259 (2021).
27. Ciarrocchi, A. et al. Thickness-modulated metal-to-semiconductor transformation in a transition metal dichalcogenide. *Nat Commun* 9, 919 (2018).
28. Ipadeola, A. K. & Ozoemena, K. I. Alkaline water-splitting reactions over Pd/Co-MOF-derived carbon obtained via microwave - assisted synthesis. *RSC Adv* 10, 17359 - 17368 (2020).
29. Jin An, S. et al. Electrolyte volume effects on electrochemical performance and solid electrolyte interphase in Si-Graphite/NMC lithium-ion pouch cells. *ACS Appl Mater Interfaces* 9, 1 - 44 (2017).
30. Wang, H. et al. Photo enhanced electrocatalytic hydrogen evolution based on multiwalled carbon nanotubes modified MoS_2-MoO_3 heterostructure. *J Alloys Compd* 891, 118753 (2022).

Chapter 5
General conclusions and future work

5.1 Conclusions

In this work, we report on the employment of colloidal synthesis to prepare Pt dichalcogenides and their electrocatalytic HER activity in alkaline electrolytes. The effect of the chalcogen precursor on the colloidal synthesis of the Pt dichalcogenides is evaluated and coalescing of the Pt dichalcogenides with N-MWCNTs is carried out and the light-induced HER activity of the nanotube-based composites determined. To the best of our knowledge, Pt dichalcogenides have not been prepared via this method and their composites with N-MWCNTs have not been explored, especially in light-stimulated HER. As such, this work presents the first insight in the reaction conditions that results in the formation of PtX_2 during colloidal synthesis as well as the in-situ preparation of $PtSe_2$/N-MWCNTs and the light-stimulated HER thereof. The Pt loading on the GC for $PtSe_2$ and $PtTe_2$ is 34 and 28 µg/cm^2, respectively. This is way lower than the Pt loading of 50 µg/cm^2 in a commercial Pt/C catalyst although the HER activity of $PtSe_2$ and $PtTe_2$ are comparable to elemental Pt.

In Chapter 3, elemental selenium, sodium selenide, and selenourea were evaluated as selenium precursors on the colloidal hot injection synthesis of $PtSe_2$ using platinum acetyl acetonoate. The choice of the precursor influences the crystallite size of the resulting $PtSe_2$, with selenourea from $PtSe_2$ with the smallest size. The catalytic properties of the $PtSe_2$ prepared from the different selenium precursors are also different. Generally, $PtSe_2$ prepared from elemental selenium displayed a higher HER catalytic activity than PtSe-SeU and $PtSe_2$-Na_2O_3Se exhibited the smallest onset potential of 46 mV, overpotential of 162 mV and 112 mVdec^{-1} Tafel slope. The pronounced HER activity displayed by $PtSe_2$-Se is attributed to its high electrochemical surface area of 90.7 cm^2 relative to $PtSe_2$-SeU and $PtSe_2$, Na_2O_3Se with surface area of 14.6 and 9.1 cm^2, respectively. Interestingly, altering the Se precursor in the colloidal synthesis of $PtSe_2$ using Pt $(AcAc)_2$ as the Pt precursor does not influence the stoichiometries of Pt and Se in the material. In the same chapter, we studied the effect of changing the Te precursor on the formation of platinum telluride in OLA and TOP at 320℃ using $PtCl_4$. The $PtCl_4$ and tellurium precursor ratio was 1:2. Using tellurium powder resulted in the formation of moncheite $PtTe_2$, while Na_2O_3Te produced a mixed-phase platinum telluride system containing PtTe and $PtTe_2$. $PtCl_4$ resulted in the formation of PtTe, with high quantities of unreacted $TeCl_4$. We reduced the molar ratio of $PtCl_4$ and $TeCl_4$ from 1:2 to 1:1

to reduce the amount of unreacted $TeCl_4$, and the resulting product was PtTe, with traces of $TeCl_4$. We can therefore conclude that the tellurium type and concentration influence the resulting phase of platinum telluride formed. $PtTe_2$, PtTe, and mixed-phase PtTe:$PtTe_2$ materials were then evaluated as alkaline HER electrocatalysts in 1 M KOH. Of the three catalysts, $PtTe_2$ demonstrated the highest HER catalytic activity with an onset potential of 29 mV and overpotential of 107 mV and a Tafel slope of 79 $mVdec^{-1}$. $PtTe_2$ portrays the highest ECSA of 464 cm^2, almost 8 times more than PtTe and PtTe:$PtTe_2$. We then compared the catalytic activity of $PtSe_2$-Se and $PtTe_2$ in 1M KOH. These are the best-performing catalysts based on the optimization of $PtSe_2$ using different Se precursors and the optimization of $PtTe_2$ using different Te precursors. Overall, the catalytic activity of $PtTe_2$ surpasses that of $PtSe_2$, due to the relatively high ECSA and roughness as determined by AFM studies. Lastly, in Chapter 4, we demonstrated how the light absorption properties of $PtSe_2$ can be improved by coalescing $PtSe_2$ with N-MWCNTs. Successful growth of $PtSe_2$ on the walls of the nanotubes was achieved by heating a mixture of OLA, O.A, and N-MWCNTs to 320 ℃ under excessive stirring. The Pt and Se precursors were then injected, and the reaction ran for 1 hour. TEM analysis showed the sheet-like structures covering the nanotubes. Solar light equivalent to 1 Sun, was shone on the working electrode at 13 cm light to GC electrode distance and the HER activities determined. An improvement in the HER activity of $PtSe_2$ was observed by the incorporation of small amounts of N-MWCNTs, 3 and 5 weight %. The HER activity of $PtSe_2$ in the dark is poor but improves when light the $PtSe_2$ is exposed to light. This implies that the $PtSe_2$ prepared in this work is s semi-conductor rather than a metalloid.

Through this work, we demonstrated that colloidal synthesis of Pt dichalcogenides can be achieved, and altering some of the parameters can influence the resulting phase, size, and morphology of the materials. Colloidal synthesis of Pt dichalcogenides is vital because of the relatively high product yield of the materials. The alkaline HER activity of Pt dichalcogenides is better than that of the other common TMDs and $PtTe_2$ exhibits the highest activity, comparable to Pt/C. The semi-conductor $PtSe_2$ anchored on N-MWCNTs shows light-dependent HER and therefore offers the opportunity to employ this material in photoelectrodes in PEC HER. Despite this, the following recommendations can be executed to advance the colloidal synthesis and possibly the physical and electrochemical properties of Pt dichalcogenides and their electrocatalytic stability improvement techniques.

5.2 Future work

- DFT studies can be carried out to determine the Gibbs free energy of hydrogen adsorption to provide further details on how the H_2 adsorption changes in $PtSe_2$ and $PtSe_2$ grown on N-MWCNTs
- The Mott-Schottky measurements of the PtX_2 and $PtSe_2$/N-MWCNTs can be carried out to determine the band edge diagram of the catalysts.
- Employ all the catalysts in HER-coupled gas chromatography to quantify the amount of hydrogen produced over time.
- Conduct the electrocatalytic activity and electrode stability of $PtSe_2$/N-MWCNTs, as an extension of the study presented in Chapter 3.
- Prepare and conduct the electrocatalytic activity and electrode stability of $PtTe_2$/N-MWCNTs, as an extension of the study presented in Chapter 3.
- Explore $PtSe_2$ and $PtSe_2$/N-MWCNTs as photocathodes in 2-electrode PEC HER.